UNIVERSITY OF SOUTHERN QUEENSLAND

Analysis of Shielded Rectangular Dielectric Rod Waveguide Using Mode Matching

A Dissertation submitted by

Colin Gordon Wells, B.Eng (Hons)

for the award of

Doctor of Philosophy

September 2005

Abstract

The limit of current technology for mobile base station filters is the multimode filter, in which each cavity supports two (or possibly three) independent degenerate resonances. Shielded dielectric resonators with a rectangular cross-section are useful in this application.

In the design of these filters, manufacturers are using software packages employing finite element or finite difference time domain techniques. However, for sufficient accuracy these procedures require large numbers of points or elements and can be very time consuming. Over the last decade research using the mode matching technique has been used to solve this kind of difficulty for various types of filter design and waveguide problems.

In this thesis a mode matching method and computer program is developed to calculate the propagation coefficients and field patterns of the modes in a shielded rectangular dielectric rod waveguide. Propagating, complex, evanescent and backward wave modes are included and the work shows the presence of a dominant mode, and other fundamental modes, not previously identified. The effect of the shield proximity on the propagation characteristics and mode spectrum is investigated, together with the limitations on the accuracy of the mode matching method.

In addition, the fields within the shielded rectangular dielectric rod waveguide, are used

to calculate the attenuation coefficient of the dominant and fundamental modes. The influence on the attenuation coefficient of the proximity of the shield to the rod is also evaluated for these modes and limitations on accuracy are discussed.

The calculated numerical results for the propagation and attenuation coefficient values are verified by measurement. The propagation coefficients results are typically within 2% of those measured. Verification of the attenuation coefficient results is achieved by comparing calculated and measured Q at the resonant frequencies of a number of shielded rectangular dielectric rod resonators. The difference between calculated and measured Q values is on average less than 4%.

In the absence of a full solution of the shielded rectangular dielectric rod resonator, these results provide useful design information for this structure.

In addition, the work reported in this thesis provides a basis for a full electromagnetic solution of this type of resonator. This would encompass the cubic dielectric resonator in a cubical cavity.

Certification of Thesis

I certify that the ideas, experimental work, results, analyses, software and conclusions reported in this dissertation are entirely my own effort, except where otherwise acknowledged. I also certify that the work is original and has not been previously submitted for any other award, except where otherwise acknowledged.

Signature of Candidate	Date
ENDORSEMENT	
Signature of Supervisors	Date

Acknowledgments

This project has benefited from the assistance of a number of people and I would like to express my gratitude to them for their contributions.

Firstly I would like to thank Dr. Jim Ball for his technical guidance and support in this project and for his reminder that sometimes unexpected results are possibly correct. Also Dr. Nigel Hancock for his encouragement and assistance with the draft of the thesis and initial proposal of the project.

I would also like to thank Dr. Mostafa Abu Shaaban of Filtronics Brisbane for suggesting that mode matching methods are computationally more efficient than purely numerical methods, when applied to filter problems. Also for explaining the advantages of multimode filters.

I would also like to acknowledge the technical support of the Faculty of Engineering and Surveying, in particular Chris Galligan and the workshop staff for the manufacture of the test cavities.

I gratefully acknowledge the support of a USQ scholarship.

I wish to express my gratitude to Andrew Hewitt and my other colleagues at the university for their friendship and exchange of ideas.

Finally I would like to thank my family for their patience in allowing me to complete this endeavor and to share my problems with them.

Contents

List of Tables

List of Figures

Chapter 1

Introduction

1.1 Project Background

An increasing requirement of mobile phone technology is to fit as many radio frequency channels as possible into the available frequency spectrum. This is not only to make efficient use of the bandwidth, it also reduces congestion for users and increases the revenue available to mobile phone companies. Another aspect of the mobile system is that, during a call, the transmitter and receiver at each end must both be on so that the users of a phone connection can converse at the same time. To achieve sufficient signal selectivity and rejection, stringent specifications are required for the dielectric loaded cavity filters employed in the mobile phone base stations. In the context of base station filters, the limit of present technology is multimode filter design.

Multimode filters are made up of coupled resonant cavities each containing a cylindrical or rectangular block of ceramic material having a high dielectric constant. These dielectric resonators store most of the electromagnetic energy and the cavity walls surrounding them are principally there to provide shielding. The dielectric resonators also allow smaller cavity size and lower energy loss compared to non-dielectric filters. This allows a sharper filter response and greater unwanted signal rejection. The term

multimode can be explained with reference to a dual-mode waveguide filter where n series cavities each support two orthogonally polarised degenerate mode resonances. Applying this technique a $2n$th degree filter can be constructed with n cavities giving a significant reduction in size compared to a conventional filter, in which each cavity supports only one resonant mode (Hunter, 2001, p. 255).

Due to difficulties caused by the interaction between components, a lot of design work on filters is still performed empirically, as in the case of the coupled dielectric resonator filter described by Walker & Hunter (2002). This is because a complete knowledge of the electromagnetic fields in the coupled cavity sections has not been achieved (Rong & Zaki, 1999). Because of their increased complexity this is especially true for the multimode dielectric loaded cavity filters.

At present commercial software packages using Finite Element (FEM) or Finite Difference Time Domain (FDTD) methods are used to overcome this. These methods work well but processing a solution of sufficient accuracy requires a large number of points or elements (large memory requirement) and can be very time consuming. If a structure is doubled in size in all coordinate directions (ie grid cell numbers increased by 2^3), or equivalently if the frequency is doubled, a 3-D FEM solution could take up to 64-times as long (depending on the sparsity of the matrix and how well the FEM software can use this to advantage) , or 16 times for a FDTD solution (Veidt, 1998, p. 134). Rong & Zaki (1999) have stated that the standard of efficiency of general purpose numerical methods using FEM (example given: Hewlett Packard HFSS) makes their use for filter design impractical.

In comparison the matching (MM) method generally gives solutions in a shorter time and requires less memory (Itoh, 1989, p. 30), as it uses well known field equations tailored to the boundary conditions of basic structure shapes common in present filter design. These equations already contain most of the information required, and only have to be matched at the junctions of the regions to obtain a solution. Moreover if the overall size of a structure or the frequency used is increased the solution time remains the same. Mode matching also gives a better understanding of the fields in the structure

in that it allows an analytical analysis of the solution once the unknown coefficients are found. This provides an insight into the mode structure which would be difficult to achieve using purely numerical methods. For example, the results for shielded dielectric rod waveguide show that this structure is capable of supporting complex modes and backward waves, in addition to the expected propagating and evanescent modes.

During discussions with Brisbane based filter manufacturer Filtronic[1], the use of the mode matching method was proposed to remedy some of the commercial solver problems as well as to predict interactions between coupled multimode resonant cavities. Although a lot of work has been done in this area over the past 10 years, no commercial software package is available that can solve the present problems in multimode dielectric loaded filter design.

This being the case, and as investigations into the use of cubic dielectric loaded resonators were being carried out by Filtronic and others, an improved theoretical understanding of these structures was desirable; and the MM technique provided a means to achieve this. Specifically, the study of the shielded rectangular dielectric rod waveguide could be seen as a basic precursor to the analysis of the cubic dielectric loaded cavity resonator. The latter procedure would take a similar path to that of Zaki & Atia (1983) where a cylindrical dielectric rod enclosed in a cylindrical waveguide was modeled and the propagation coefficients of the fundamental modes were found. Metallic plates were then placed on the ends of a section of this waveguide forming a cylindrical dielectric loaded cavity resonator. Mode matching was then used to solve the resonant frequency eigenvalue problem. Later Liang & Zaki (1993) extended this to cylindrical dielectric resonators in rectangular waveguide and cavities.

[1]Filtronic Pty Ltd, Metroplex Avenue, Murarrie, Qld., Australia / http://www.filtronic.co.uk

1.2 The Proposition of the Thesis

The proposition of this thesis is that the mode matching method has significant advantages for the analysis of the electromagnetic fields of structures used in current dielectric loaded multimode cavity filters. In general the method requires less CPU time than a strictly numerical procedure, such as the finite element method, due to its inherent analytic pre-processing; and it also provides a better physical understanding of the field structure.

1.3 Aim and Objectives

The broad aim of the project is to perform electromagnetic field analysis on the shielded rectangular dielectric rod waveguide using the mode matching method.

The specific objectives of the project are as follows:

1. (a) To perform a literature survey on the use of mode matching in general and to replicate the results of some of the early work associated with rectangular waveguide discontinuities. A number of computer programs would have to written to achieve this and would provide confidence in the validity of later original work.

   (b) Apply mode matching to the analysis of cylindrical structures such as a coaxial resonator. This work was seen as an exercise in the use of mode matching to solve eigenvalue problems. For the case of the coaxial resonator these values are the resonant frequencies of the structure. In the event this work produced some original results suitable for publication it would be included in the thesis.

2. Perform a thorough investigation of the shielded rectangular dielectric rod waveguide. This work would include an investigation of the proximity effect of the shield

and of the losses associated with this structure. This would provide a foundation for a complete analysis of shielded rectangular cross-section dielectric resonators (as has been achieved for cylindrical resonators (Zaki & Atia, 1983)).

1.4 Overview of the Thesis

Chapter 1
Introduction

Chapter 1 introduces the proposition driving this research, namely that the mode matching method has some advantages for the electromagnetic analysis on a structure associated with the latest dielectric loaded multimode cavity filters. Chapter 1 also outlines the aim and objectives of the research and highlights those areas where original work has been performed.

Chapter 2
Overview of the Mode Matching Method

The first part of Chapter 2 presents two literature surveys, firstly to give some background to the project in the area of microwave cavity filters and secondly the theory and application of mode matching techniques. The second part of Chapter 2 details mode matching theory related to rectangular waveguide discontinuity problems. The last part of the chapter gives an insight into some of the early work accomplished in applying the mode matching procedure. This is shown by comparing some of the results from literature for waveguide discontinuity problems with those from computer programs written to replicate them.

Chapter 3
The Coaxial Resonator

In this chapter a coaxial line in the form of a cylindrical cavity with a centre conductive

rod (single coaxial resonator) is studied. A simplified mode matching procedure is used to find the TEM mode resonant frequencies and gap capacitance. This chapter is an expansion of a paper published in *IEE Proceedings on Microwave Antennas and Propagation* (Wells & Ball, 2004).

Chapter 4
The Shielded Rectangular Dielectric Rod Waveguide

In Chapter 4 the mode matching method is developed to allow the computation of the propagation coefficients and field patterns of the fundamental modes in a shielded rectangular dielectric rod waveguide. The full solution described in this chapter shows the results of all the dominant modes and field patterns. It also shows that in addition to conventional waveguide modes the structure can support complex waves and backward waves. This original work is an expansion of a paper published in *IEEE Transactions on Microwave Theory and Techniques* (Wells & Ball, 2005*b*).

Chapter 5
Attenuation of a Shielded Rectangular Dielectric Rod Waveguide

In this chapter the calculated fields, found using the mode matching method of Chapter 4, are employed to find the wall and dielectric losses of the waveguide and hence its attenuation. For the E_{11}^{y} mode and the dominant E_{21}^{x}/E_{12}^{y} coupled mode the effect of the proximity of the shield on the attenuation is also be evaluated. This work is original, and is an expansion of a paper submitted for publication (Wells & Ball, 2005*a*).

Chapter 6
Conclusion

This chapter summarises the major findings of the thesis and their significance to the wider body of knowledge in the field. The chapter concludes with a summary of suggested areas for future work.

Appendix A

Coaxial Resonator Mode Matching Equations

This appendix provides a summary of the basis functions and integrals used in the mode matching method developed for the coaxial resonator in Chapter 3.

Appendix B
Shielded Rectangular Dielectric Rod Mode Matching Equations

This appendix provides a summary of the basis functions, continuity equations at boundaries and integrals used in the mode matching method developed for the shielded rectangular waveguide in Chapter 4.

Appendix C
Calculation of Unloaded Q Factor from the Measured Reflection Coefficient of a Resonator

In this appendix the method used for determining unloaded Q factor from the measured reflection coefficient S_{11} of the resonant structures of section 5.6 is described.

Appendix D
Guide to the Thesis Companion Disk

This appendix provides a guide to the thesis companion disk. The disk contains a copy of the dissertation and a basic cross-section of the main computer programs for the coaxial resonator of Chapter 3, the rectangular shielded dielectric rod of Chapter 4 and for the rectangular shielded dielectric rod attenuation in Chapter 5.

1.5 Summary of Original Work

The areas of this project where original work has been performed are summarised below.

1. A simplified mode matching method of finding the resonant frequency of a coaxial

resonator, and calculation of the gap capacitance.

2. Calculation of the propagation coefficients of the modes in a shielded rectangular dielectric rod waveguide. Propagating, complex, evanescent and backward wave modes were included and the work showed the presence of a dominant mode, and other fundamental modes, not previously identified. The effect of the proximity of the shield to the dielectric rod on the propagation coefficient and mode structure was also investigated.

3. Calculation of the attenuation coefficient of the commonly used E_{11}^{y} mode, and other fundamental modes, in a shielded rectangular dielectric rod waveguide. The influence on the attenuation coefficient of the proximity of the shield to the rod was also evaluated.

1.6 Publications

Wells, C. G. & Ball, J. A. R. (2004), 'Gap capacitance of a coaxial resonator using simplified mode matching', *IEE Proceedings on Microwave Antennas and Propagation*, **151**(5), 399 -403.

Wells, C. G. & Ball, J. A. R. (2005), 'Mode matching analysis of a shielded rectangular dielectric rod waveguide ', *IEEE Transactions on Microwave Theory and Techniques*, **53**(10), 3169-3177, October.

Wells, C. G. & Ball, J. A. R. (2005), 'Attenuation of a shielded rectangular dielectric rod waveguide ', *submitted for publication in IEEE Transactions on Microwave Theory and Techniques.*

Chapter 2

Overview of the Mode Matching Method

2.1 Introduction

This chapter begins with a description of two literature surveys. The first is on the topic of microwave cavity filters. This describes how these filters have evolved from simple cavity and combline filters of forty years ago to the small multimode dielectrically loaded high selectivity types of today. The second describes how the mode matching method has been used over this same period to solve at first, waveguide discontinuity problems, and then later, aid in the design of combline, finlines, microstrip lines and many other structures including dielectric loaded cavity filters.

Section 2.4 details the basic theory behind the mode matching method. The problem of the junction of two rectangular waveguides in a boundary reduction configuration is used as an example.

Finally section 2.5 describes the results obtained from a mode matching program written for the rectangular waveguide discontinuity problem of the previous section. This

program was written to gain experience in writing mode matching code, by using past papers as a procedural guide (no code is ever given), and comparing the results with those published.

2.2 Microwave Cavity Filters

A generation ago virtually all design information available on microwave filters was summarised in the classic text titled "Microwave Filters, Impedance Matching Networks and Coupling Structures" (Matthaei et al., 1984). Amongst other types, this dealt with design of combline filters, from which present day base station filters could be said to have evolved.

In the early 1970s dual mode filters, which effectively double the use of a cavity and make the overall filter smaller, were introduced by Atia & Williams (1972). An other step forward occurred when Fiedziuszko (1982) described dual mode dielectric loaded filters. These allowed further size reduction, improved in-band performance and provided greater thermal stability. Wang et al. (1998) described a dielectric loaded version of the combline filter which combined the merits of the metallic combline and dielectric loaded filters. A mode matching method was used to model the electromagnetic fields in the filter from which filter parameters were calculated. Sabbagh et al. (2001) and Wu et al. (2002) then described methods for solving problems in this type of filter when a number of interacting combinations of resonant cavities in the same type of filter were coupled together.

2.3 Brief History of Mode Matching Method in Filter Design

Up until about 1960 electromagnetic field modeling was only possible for simple structures which could be analysed theoretically. Since then the mode matching method,

and other numerical methods, have been devised and then gradually improved to cope with the invention of many new and complex microwave structures. Initially, these were applied to the analysis of the discontinuities in rectangular waveguides.

The use of computer-aided mode matching to calculate the fields of simple structures began in the 1960s with papers by Wexler (1967) and Clarricotes & Slinn (1967). The use of computers has been an essential part of the method's development because of the amount of repetitive calculations required to reach a solution.

Luebbers & Munk (1973) used the method to calculate the reflection and transmission properties of a thick rectangular window in centrally located in a rectangular waveguide. The waveguides on either side of the window had to be identical.

Patzelt & Arndt (1982) and Safavi-Naini & Macphie (1982) adapted the method to solve problems involving the junction of rectangular to rectangular waveguide steps as used in waveguide transformers, irises (small windows across the waveguide) and reactance coupled filters. By addition of the use of a technique involving the conservation of complex power, rapid convergence of numerical results was achieved (Safavi-Naini & Macphie, 1981). Also the results of a junction were presented in the form of a scattering (S) parameter matrix. This enabled a number of cascaded junctions in a system to be analysed in a unified manner.

Omar & Schunemann (1985) showed that the orthogonality relations associated with the cross-product of field vectors, as used sometimes in mode matching, were again related to the conservation of complex power [1] and hence good convergence properties could be obtained. Also transmission matrix results were used in the formulation of a multi-section finline bandpass filter. Calculations with this type of matrix have lower computation time than with the S parameter matrix, but problems can sometimes occur with the convergence of a solution (Alessandri et al., 1988).

[1] Complex power is the combination of the real and reactive power of the electric and magnetic fields in a region in space. The concept is used in many texts associated with time harmonic electromagnetic fields where it appears in derivations of Poynting's theorem (Pozar, 1998, pp. 26-29)(Harrington, 2001, pp. 19-23)

About the same time Chu & Itoh (1986) modeled cascaded microstrip step discontinuities using mode matching. An equivalent waveguide model was introduced for the microstrip line. Also Wade & Macphie (1986) used the method to determine exact solutions at the junction of circular and rectangular waveguide. James (1987) provided solutions to irises in coaxial and circular waveguides.

Analyses of dielectric inserts in waveguide first appeared in 1988 (Gesche & Lochel, 1988), (Zaki et al., 1988). Also a more formalised approach to the cascading of junction discontinuities in general were formulated in a paper by Alessandri et al. (1988). Particular types of junction problems were recognised and placed into so called mode matching building blocks allowing the Computer Assisted Design (CAD) of a large class of waveguide components (Arndt et al., 1997). It may be possible to use a variation of this approach to analyse microwave filters.

A number of papers, spanning the early 1990's and extending this formalised approach, then appeared for rectangular waveguide: Sieverding & Arndt (1992) for the T-junction building block and Reiter & Arndt (1992) for cascaded H-plane discontinuities.

Through the 1990s a succession of papers appeared that involved the method in the solution of problems related to dielectric loaded waveguide cavities and filters. Most of these were written in association with K. A. Zaki from the University of Maryland (Chen & Zaki, 1991), (Liang & Zaki, 1993), (Yao et al., 1995), (Wang et al., 1997).
In 1998 Wang et al. (1998) described the calculation of the parameters of a dielectric loaded combline filter. Sabbagh et al. (2001) and Wu et al. (2002) described methods for solving problems in this type of filter when a number of interacting combinations of resonant cavities in the same type of filter were coupled together. These final references were mentioned in section 2.2 and represent the current level of filter technology and the most ambitious application of mode matching method to filter design to date.

2.4 Mode Matching

The mode matching procedure is useful for solving scattering parameter problems at a discontinuity in a structure. It can be applied to junctions of different types of waveguide or posts or obstructions in a waveguide. Additionally it can be used in eigenvalue problems such as finding the resonant frequency of a cavity, the cutoff frequency of a waveguide or the propagation coefficient of a transmission line.

2.4.1 Basic Procedure

To model a discontinuity a structure is divided into separate regions either side of the discontinuity. The fields in each region are expressed as a sum of modes. In the case of common rectangular waveguide these modes would be the electric and magnetic TE and TM modes of homogeneously filled rectangular waveguide. By matching the tangential components of the modes at the boundary between regions and using their orthogonality properties an infinite set of linear equations can be obtained.

A number of formulations are available in the literature to achieve this, and the principal difference between these lies in the method they use to expand the mode functions to form an infinite set of equations. The method of Shih, described in Itoh (1989), uses the dot product of testing functions with the mode functions whereas the method described by Eleftheriades et al. (1994) uses a cross product. Ultimately there does not appear to be a significant difference in the results using either of these methods and the final decision of which to use comes down to the ease by which they can be applied to the type of structure involved.

The set of equations can then be solved for the unknown coefficients of the mode functions and the superposition of these functions will give the actual resultant fields caused by the discontinuity. This will allow field plotting, the calculation of loss and the study of field intensity in the structure. Alternatively the equations can be arranged so that the forward and reflected component coefficient elements will form a Generalised

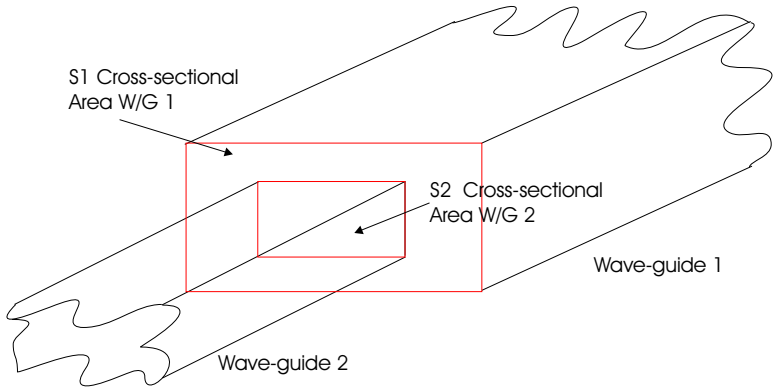

Figure 2.1: Boundary Reduction Wave-guide Configuration

Scattering Matrix (GSM) from which the the scattering parameters of the discontinuity can be obtained.

2.4.2 A Boundary Reduction Discontinuity Problem

The mode matching technique is usefully illustrated by means of a simple example, that of the determination of the scattering parameters of a waveguide discontinuity.

The junction of a large to small waveguide is shown in Figure 2.1. This is called a Boundary Reduction (BR) configuration when the input wave travels from the larger into the smaller guide. In an early paper on mode matching by Wexler (1967), systems of equations were derived, which were solved for all forward and reflected scattering coefficients of the modes either side of the junction of waveguides of different cross-section. It has been shown in many later papers and texts, such as Omar & Schunemann (1985) and Itoh (1989), that these equations can be used in the much more convenient form of the Generalised Scattering Matrix (GSM). The conventional form of the Scattering Matrix(S), as used in single moded transmission line systems, describes the ratio of the amplitudes of forward and reflected waves at ports, or between ports of a network. The GSM extends this to include the dominant and all scattered modes at a junction, whether propagating or evanescent. The use of the GSM not only enables all modes to contribute to the result, it also allows a number of discontinuities to be cascaded

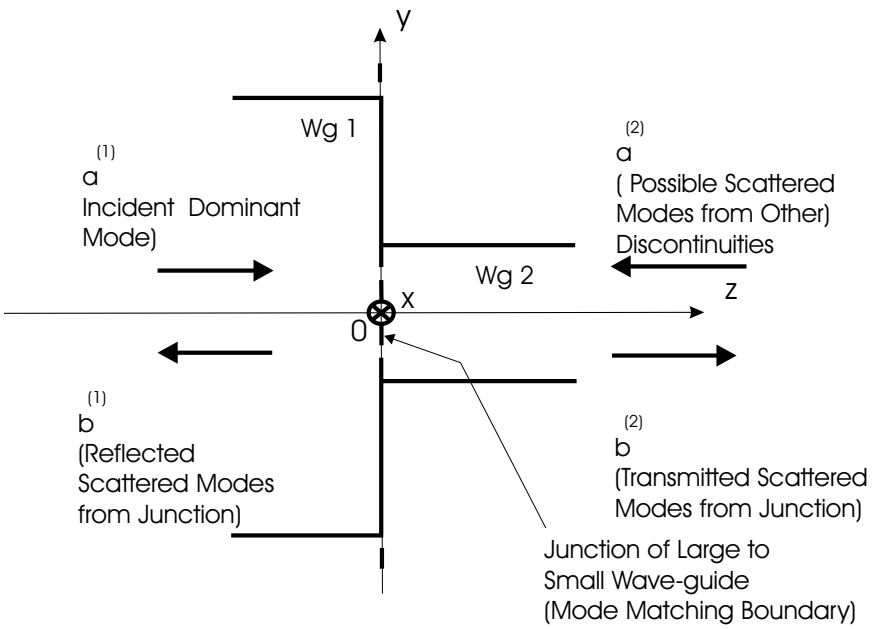

Figure 2.2: Forward and Reflected Components at a BR Wave-guide Junction

together by the algebraic combination of their S matrices. Figure 2.2 shows how the forward $(\mathbf{a}^{(1)}, \mathbf{a}^{(2)})$ and the reflected $(\mathbf{b}^{(1)}, \mathbf{b}^{(2)})$ modal amplitude vectors are arranged at the junction.

To implement the mode matching procedure the tangential components of the modes are forced to be continuous at the mode matching boundary. The boundary conditions to be satisfied are:

$$\mathbf{E}_t^{(1)} = \begin{cases} \mathbf{E}_t^{(2)} & \text{on } S_2 \\ 0 & \text{on } S_1 - S_2 \end{cases} \tag{2.1}$$

$$\mathbf{H}_t^{(1)} = \mathbf{H}_t^{(2)} \qquad \text{on } S_2 \tag{2.2}$$

where

$\mathbf{E}_t^{(i)}$ and $\mathbf{H}_t^{(i)}$ are the transverse electric and magnetic fields tangential at the boundary,

S_1 and S_2 are the cross-sectional areas of waveguides 1 and 2 respectively; and

$$\mathbf{E}_t^{(1)} = \sum_{m=1}^{\infty}(a_m^{(1)}e^{-\gamma_1 z} + b_m^{(1)}e^{\gamma_1 z})\mathbf{e}_{tm}^{(1)} \tag{2.3}$$

$$\mathbf{E}_t^{(2)} = \sum_{n=1}^{\infty}(b_n^{(2)}e^{-\gamma_2 z} + a_n^{(2)}e^{\gamma_2 z})\mathbf{e}_{tn}^{(2)} \tag{2.4}$$

$$\mathbf{H}_t^{(1)} = \sum_{m=1}^{\infty}(a_m^{(1)}e^{-\gamma_1 z} - b_m^{(1)}e^{\gamma_1 z})\mathbf{h}_{tm}^{(1)} \tag{2.5}$$

$$\mathbf{H}_t^{(2)} = \sum_{n=1}^{\infty}(b_n^{(2)}e^{-\gamma_2 z} - a_n^{(2)}e^{\gamma_2 z})\mathbf{h}_{tn}^{(2)} \tag{2.6}$$

where m and n are all the TE and TM modes of rectangular waveguide in waveguides 1 and 2 respectively and a and b are the amplitude coefficients of those modes.

The transverse components (at the z = 0 boundary) can be written from those in Pozar (1998) as:

$$e_{x_{p\,q}}^{(i)} = \left\{ \begin{array}{c} -q\frac{A^{(i)}}{B^{(i)}} \\ p\frac{B^{(i)}}{A^{(i)}} \end{array} \right\} \cos\beta_{x_p} x \sin\beta_{y_q} y \left\{ \begin{array}{c} TE \\ TM \end{array} \right\} \tag{2.7}$$

$$e_{y_{p\,q}}^{(i)} = \left\{ \begin{array}{c} p \\ q \end{array} \right\} \sin\beta_{x_p} x \cos\beta_{y_q} y \left\{ \begin{array}{c} TE \\ TM \end{array} \right\} \tag{2.8}$$

$$h_{x_{p\,q}}^{(i)} = \left\{ \begin{array}{c} -pY_\omega^h \\ -qY_\omega^e \end{array} \right\} \sin\beta_{x_p} x \cos\beta_{y_q} y \left\{ \begin{array}{c} TE \\ TM \end{array} \right\} \tag{2.9}$$

$$h_{y_{p\,q}}^{(i)} = \left\{ \begin{array}{c} -p\frac{A^{(i)}}{B^{(i)}}Y_\omega^h \\ q\frac{B^{(i)}}{A^{(i)}}Y_\omega^e \end{array} \right\} \cos\beta_{x_p} x \sin\beta_{y_q} y \left\{ \begin{array}{c} TE \\ TM \end{array} \right\} \tag{2.10}$$

where

$$\beta_{x_p}^2 + \beta_{y_q}^2 = \gamma_{p\,q}^2 + \beta_0^2\varepsilon_r \tag{2.11}$$

$$Y_\omega^h = \frac{\gamma_{p\,q}}{\omega\mu_0};\ Y_\omega^e = \frac{\omega\varepsilon_0\varepsilon_r}{\gamma_{p\,q}} \tag{2.12}$$

$$\beta_{x_p} = \frac{p\pi}{A^{(i)}};\ \beta_{y_q} = \frac{q\pi}{B^{(i)}};\ \beta_0^2 = \omega^2\mu_0\varepsilon_0 \tag{2.13}$$

and $A^{(i)}$and $B^{(i)}$ are the width and height of the waveguides respectively and p and q are the TE and TM mode indicies for rectangular waveguide.

To implement the mode matching procedure on a computer it is necessary to truncate the infinite number of modes involved to a value that will give the required accuracy in the solution. Increasing numbers of modes are tried in the initial computation until the result converges to a sufficiently constant value. The maximum number of modes allocated for computation in waveguides 1 and 2 will now be designated M and N respectively.

For proper convergence of the solution the number of modes in the larger waveguide should always be greater than that in the smaller, ie $M > N$ for Figure 2.2. If this is not done there could be a violation of the field distributions at the edge of a conductive boundary and ill-conditioning of the linear system of equations themselves can also occur (Mittra & Lee, 1971). This is a consequence of truncating the number of modes in each region from their true infinite value and in calculation is equivalent to truncating two infinite series (Itoh, 1989, pp. 603-4). It will be shown later in section 2.5 that the numerical solution will converge to different values depending on the ratio of the number of modes chosen in each region. This phenomenon is called relative convergence and is a limitation to the accuracy of the mode matching procedure. Fortunately some simple rules can be employed to minimise its effect on accuracy. For example, for a boundary reduction in height only, researchers have found that keeping the ratio of modes in each waveguide region equal to that of the ratio of corresponding regional cross-section side lengths gives optimum results (Itoh, 1989, p. 613).

A procedure to create a set of linear equations from the truncated form of equations (2.3), (2.4), (2.5) and (2.6) and using the boundary conditions of (2.1) and (2.2), is implemented by Omar & Schunemann (1985) and discussed by Eleftheriades et al. (1994). This cross product formulation, used with rectangular waveguide discontinuities, is used more often and given greater detail in the literature than the dot product method. In the cross product formulation the dot product of the z unit vector is applied to the result to give a scalar answer and in so doing uses only the tangential components and testing functions at the mode-matching boundary as required. The formulation is also related to the conservation of complex power across the discontinuity boundary (Omar

& Schunemann, 1985) and also allows a better understanding of the mode matching method and makes it easier to write a workable program. This procedure is as follows:

1. Find the cross product of the electric field equations on both sides of the junction with a testing function from the magnetic field equation of the waveguide 1 and integrate.

   In wave-guide (1)

   $$\int_{s_1} \left(\mathbf{e}_m^{(1)} \times \mathbf{h}_n^{(1)}\right) \cdot \hat{z}\, ds = P_m^{(1)} \delta_{mn} \tag{2.14}$$

   In wave-guide (2)

   $$A_{nm} = \int_{s_2} \left(\mathbf{e}_m^{(2)} \times \mathbf{h}_n^{(1)}\right) \cdot \hat{z}\, ds \tag{2.15}$$

2. Find the cross product of the magnetic field of waveguide 2 with a testing function from the electric field equation of the same waveguide and integrate, ie

   $$\int_{s_2} \left(\mathbf{e}_n^{(2)} \times \mathbf{h}_m^{(2)}\right) \cdot \hat{z}\, ds = Q_n^{(2)} \delta_{nm} \tag{2.16}$$

   Note that the integral of the cross product of the magnetic field of waveguide 1 with a testing function from the electric field equation of waveguide 2 could be calculated as:

   $$B_{mn} = \int_{s_2} \left(\mathbf{e}_m^{(2)} \times \mathbf{h}_n^{(1)}\right) \cdot \hat{z}\, ds \tag{2.17}$$

   However, in view of the equality:

   $$B_{mn} = A_{nm}^t \tag{2.18}$$

   where superscript t means transpose, only A_{nm} need be calculated.

   In equations (2.14), (2.15), (2.16) and (2.17) m and n are the TE plus TM modes used where:

   $$\begin{aligned} m &= 1, 2, ..., M \\ n &= 1, 2, ..., N \end{aligned} \tag{2.19}$$

   and δ_{mn} and δ_{nm} are Kronecker deltas

3. The amplitude vectors can then be related by two sets of linear equations in matrix form:

$$[\lambda_P]\,(\,[\mathbf{a}^{(1)}] + [\mathbf{b}^{(1)}]\,) = [A_{nm}]\,(\,[\mathbf{a}^{(2)}] + [\mathbf{b}^{(2)}]\,) \qquad \text{electric field} \tag{2.20}$$

$$[A_{nm}]^t\,(\,[\mathbf{a}^{(1)}] - [\mathbf{b}^{(1)}]\,) = [\lambda_Q]\,(\,[\mathbf{b}^{(2)}] - [\mathbf{a}^{(2)}]\,) \qquad \text{magnetic field} \tag{2.21}$$

where:
$\lambda_P = (P_m^{(1)}\delta_{mn})$ and $\lambda_Q = (Q_n^{(2)}\delta_{nm})$ are diagonal matrices of M x M and N x N respectively. They contain the normalisation constants for each individual mode in each wave-guide and:
A_{nm} and A_{nm}^t are N x M and M x N matrices respectively which show the reaction or coupling between modes across the wave-guide junction.

From these sets of linear equations the unknown coefficients ($\mathbf{a}^{(1)}, \mathbf{a}^{(2)}, \mathbf{b}^{(1)}$ and $\mathbf{b}^{(2)}$) of the BR junction can be found or the Generalised Scattering Matrix (GSM) can be derived:

1. In the method described by Wexler (1967) the electric field equation was re-arranged for the $\mathbf{b}^{(1)}$ coefficients and the resultant equation was substituted into the magnetic field equation to eliminate them. This, and the fact that the $\mathbf{a}^{(1)}$ modal input and the scattered modes from a later junction $\mathbf{a}^{(2)}$ would be known, gave sufficient equations to solve for the $\mathbf{b}^{(2)}$ coefficients. These could then be substituted into the original equations to find the remaining $\mathbf{b}^{(1)}$ coefficients.

2. In the method described by Omar & Schunemann (1985) the GSM for the junction is derived. Firstly the equations are arranged into the following form:

$$\mathbf{a}^{(1)} + \mathbf{b}^{(1)} = [R] \cdot (\mathbf{a}^{(2)} + \mathbf{b}^{(2)}) \tag{2.22}$$

$$[T] \cdot (\mathbf{a}^{(1)} - \mathbf{b}^{(1)}) = \mathbf{b}^{(2)} - \mathbf{a}^{(2)} \tag{2.23}$$

where:
$[R] = [\lambda_P]^{-1} \cdot [A_{nm}]$

and

$[T] = [\lambda_Q]^{-1} \cdot [A_{nm}]^t$

By dividing these equations through by the appropriate $\mathbf{a}^{(j)}$ coefficient calculation of the S matrix elements can be performed by use of the standard formula:

$$S_{ij} = \left. \frac{b^{(i)}}{a^{(j)}} \right|_{a_k=0 \; for \; k \neq j} \tag{2.24}$$

Using this procedure Omar & Schunemann (1985) give the S parameters, which are actually GSM parameters, as:

$$[S_{11}] = ([R][T] + [I])^{-1} \cdot ([R][T] - [I]) \tag{2.25}$$

$$[S_{12}] = 2([R][T] + [I])^{-1} \cdot [R] \tag{2.26}$$

$$[S_{21}] = [T]([I] - [S_{11}]) \tag{2.27}$$

$$[S_{22}] = [I] - [T][S_{12}] \tag{2.28}$$

where:

I is the identity matrix.

The scattering matrix representation can then be written as:

$$\begin{bmatrix} \mathbf{b}^{(1)} \\ \mathbf{b}^{(2)} \end{bmatrix} = \begin{bmatrix} [S_{11}] & [S_{12}] \\ [S_{21}] & [S_{22}] \end{bmatrix} \cdot \begin{bmatrix} \mathbf{a}^{(1)} \\ \mathbf{a}^{(2)} \end{bmatrix} \tag{2.29}$$

2.5 Numerical Results for the Boundary Reduction Discontinuity

A computer program was written to duplicate a number of the results found in literature for this type of discontinuity. This was done so as to gain experience in producing mode matching code and also to be able to experiment with some of the problems associated with the method such as relative convergence (see section 2.4.2).

The first case considered was when the waveguides are of equal height and are axially symmetrical at the junction. The smaller waveguide width was then varied over the

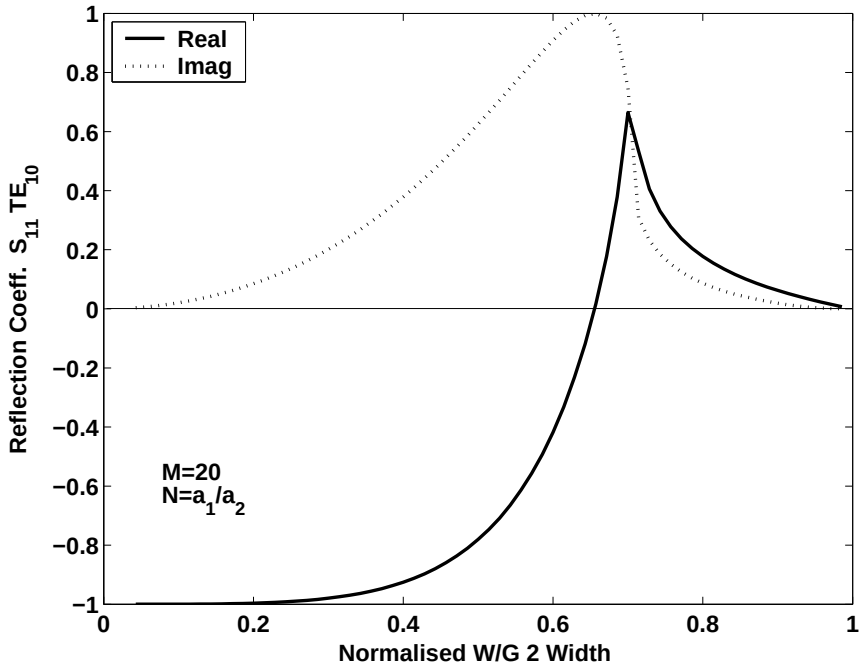

Figure 2.3: Reflection coefficient S_{11} of the incident TE_{10} mode to the BR discontinuity

range of the larger and the reflection coefficient S_{11} of an incidentTE_{10} mode was found to be as in Figure 2.3. For calculation the larger waveguide (1) dimensions were made the same as WR284 (72.14 x 34.04mm) and the frequency was determined from the free space wavelength λ, calculated as:

$$\lambda = \frac{a_1}{0.71} \tag{2.30}$$

where a_1 is the width of the large waveguide. This is the same as that used in a paper by Shih & Gray (1983) referred to later. Twenty TE_{p0} modes (M) were used in waveguide (2) and N modes in waveguide 1 calculated from the expression:

$$N = M\frac{a_1}{a_2} \tag{2.31}$$

Where a_1 and a_2 are the widths of waveguides 1 and 2 respectively.
This is to satisfy the relative convergence criteria.

When a TE_{10} mode is incident on this type of structure only the TE_{p0} modes are excited (Shih & Gray, 1983) which reduces the number of modes required in the program appreciably. The logical result can be seen in Figure 2.3 where full reflection is

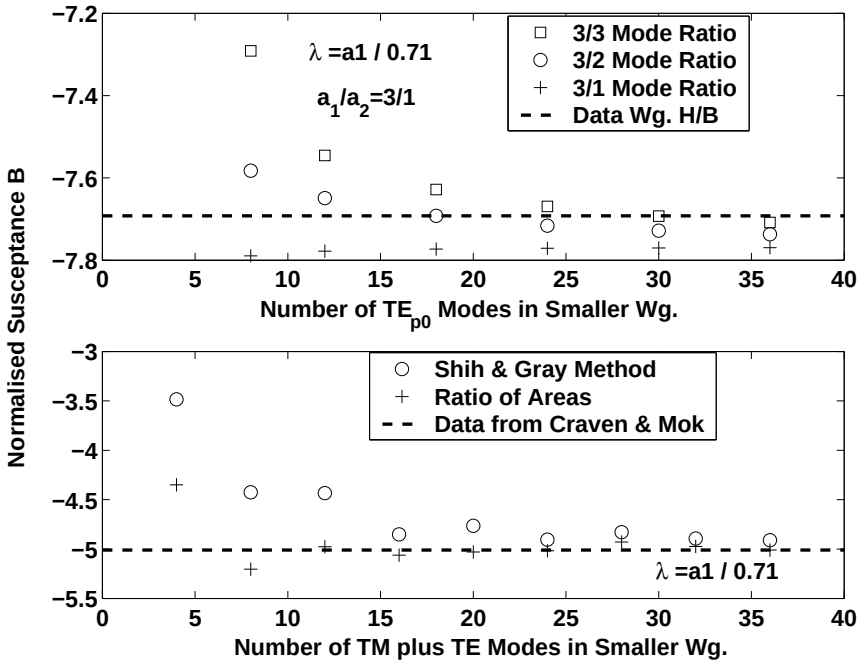

Figure 2.4: Mode matching susceptance results for the change in cross-section of a rectangular waveguide. Upper graph: symmetrical change in width only (single step) with a waveguide region width ratio of 3/1. Lower graph: symmetrical change in height and width (double step) with a waveguide region height and width ratios of 2/1.

approached as the width of waveguide 2 draws near to zero and the reflection becomes minimal as the width of the waveguides become the same.

An investigation into the input susceptance results using mode matching for a BR junction was described in a paper by Shih & Gray (1983). In this paper both the single step (width only case of the previous example in this section) and also a double step, where both the height and width are varied symmetrically, are described. This procedure was duplicated using the program written and the results are shown in Figure 2.4. The the upper graph shows the convergence characteristics for the single step with a waveguide region height ratio $a_1/a_2 = 3/1$ compared to a number of mode ratios. Convergence can be seen to be faster, for the same number of modes in the smaller waveguide, when the region height ratio is equal to the mode ratio. This verifies the results of Shih & Gray (1983). Similarly the lower graph shows the convergence characteristics for the double step with ratio of heights and widths equal to 2.

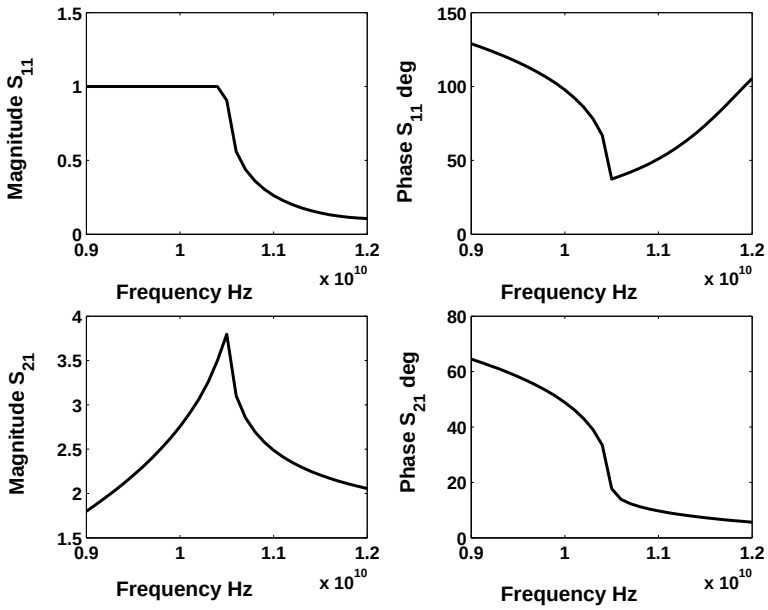

Figure 2.5: Duplication of the results of Figure 3 Safavi-Naini & McPhie (1982). Magnitude and phase of S_{11} and S_{21} for the BR junction double step.

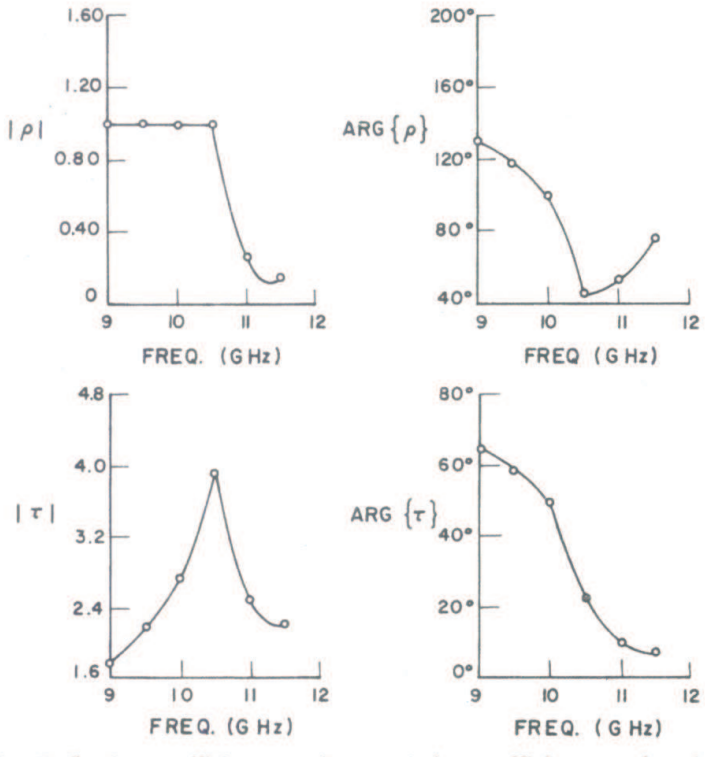

Figure 2.6: Scan of the actual results for the BR junction double step, Figure 3 Safavi-Naini & McPhie (1982).

The ratio of areas and the Shin and Gray method (Shih & Gray, 1983) give similar convergence.

For a higher number of modes, where convergence is best, the calculated results compare well with those from the Waveguide Handbook (Marcuvitz, 1951) for the single step (within 1% for 36 modes in the input waveguide). Similarly for the double step the calculated results are within 2% or less of the approximation of Craven & Mok (1971) for 36 input waveguide modes.

Finally the results for the double step BR junction from a paper by Safavi-Naini & Macphie (1982) were duplicated. The magnitude and phase of the reflection coefficient and the transmission coefficient from the calculated results are plotted in Figure 2.5 and are almost identical with the actual Safavi-Naini & Macphie (1982) results shown in Figure 2.6.

2.6 Conclusion

This chapter began with two literature surveys that gave a brief history of microwave cavity filters and the use of the mode matching method over the last forty years.

The basic theory behind the mode matching method was then described. To illustrate this a boundary reduction discontinuity problem in rectangular waveguide was used as an example.

Results from experiments using a mode matching program, written as an exercise to solve problems for this type discontinuity, gave information on the nature of the rate of convergence and the relative convergence problem. These problems were found to be associated with the number of modes and the ratio of the number of modes in each region.

Results from literature were also compared to those obtained from the mode matching

program. The closeness of the results indicated that the code written was performing correctly and that future mode matching programs, created for the main objectives of the thesis, would have a sound basis.

Chapter 3

The Coaxial Resonator

3.1 Introduction

After the initial introduction to mode matching through the analysis of rectangular waveguide discontinuities, the coaxial resonator was selected as it was considered that this would be a good learning exercise in using the method with regard to resonators and the inherent eigenvalue problem of finding the resonant frequency.

Coaxial filters are used in wireless and mobile communication applications due to their small size, low cost and relatively high Q factor. Traditionally these filters have been designed using filter theory based on TEM mode transmission line structures (Matthaei et al., 1984).

In this chapter a coaxial line in the form of a cylindrical cavity with a centre conductive rod (single coaxial resonator) as shown in Figure 3.1 will be studied. A simplified mode matching procedure is used to find the TEM mode resonant frequencies. This chapter is an expansion of a paper published in *IEE Proceedings on Microwave Antennas and Propagation* (Wells & Ball, 2004).

The coaxial line studied is less than $\frac{\lambda}{4}$ in length, with open and short circuit ends.

The inductance provided by the line at the open circuit, and capacitance due to the gap Cg, provide conditions for a resonant circuit. The resonant frequency can be adjusted by altering the gap capacitance with the aid of a tuning screw. Size constraints may require the coaxial line length to be reduced to $\frac{\lambda}{8}$ or less, which means that a substantial capacitance is required to bring the structure to resonance. This in turn means the gap must be quite small. However calculation using a parallel plate capacitance model will only give an approximate resonant frequency for the structure, as the total capacitance will be larger due to fringing effects around the open circuit end of the centre conductor. If a tuning screw is added, as shown in the figure, it will further complicate the capacitance evaluation.

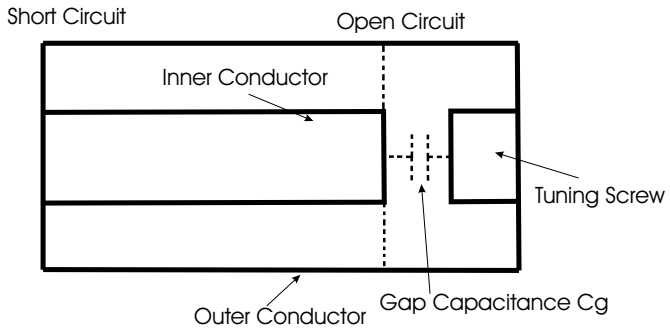

Figure 3.1: Single Coaxial Transmission Line Resonator

This problem can be overcome by the use of a rigorous mode matching method (Wexler, 1967) (Omar & Schunemann, 1985) to compute the resonant frequency of the cavity, and hence the gap capacitance. The cavity is partitioned into two cylindrical regions, as in Figure 3.2, and the fields in each region are represented as linear combinations of radial basis functions [1]. Since only the lowest order quasi-TEM resonant frequency is required, only radial basis functions having no circumferential variation need be included. The transverse fields are matched at the boundaries between regions to ensure that they are continuous, and a set of simultaneous equations is produced. The resonant frequency is found by equating the determinant of this system to zero. Resonant frequencies computed in this way show excellent agreement with measured results.

[1] To reduce confusion with the term 'modes', the modes of radial waveguide, used to 'build up' the actual modes of the structure, will be called radial basis functions in this chapter.

Once the resonant frequency has been found, the gap capacitance can be calculated. For filter applications, a requirement is to maximise the resonator Q-factor. This is accomplished by choosing the coaxial line radius ratio a/r_o to be 3.591 (Sander, 1987, p. 24), which minimises the conductor losses in the coaxial surfaces. This corresponds to an air-spaced characteristic impedance of 76.7Ω. Values of gap capacitance are provided for this optimum situation.

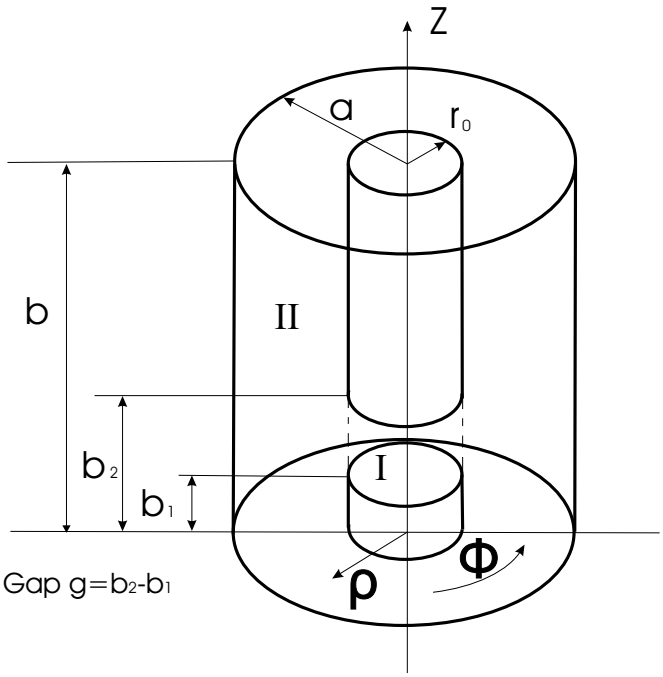

Figure 3.2: Single Coaxial Resonator Coordinate System

3.2 Analysis using the Radial Mode Matching Method

The mode matching method used in this chapter represents the fields within the cavity in terms of radial waves, and is similar to that used by Kobayashi and others (Kobayashi et al., 1981) (Yao et al., 1995) (Kajfez & Guillon, 1986) to solve the general problem of cylindrical posts in waveguides . Another method, called the longitudinal mode matching method, has been used by Risley (1969) and Zaki & Atia (1983). It entails the matching to be performed at a plane at right angles to the cylindrical axis, and

so uses cylindrical waveguide basis functions. This method was not used as it requires the integral of the product of Bessel functions, which makes the problem more complex and increases the computation time (Chen, 1990).

The structure to be analysed is shown in Figure 3.2, and is composed of two air filled regions. Region I is the cylindrical gap between the inner rod and the tuning screw, assumed to be of the same diameter ($b_1 < z < b_2,\ 0 < \rho < r_o,\ 0 < \phi < 2\pi$). The remainder of the cavity is region II ($0 < z < b,\ r_o < \rho < a,\ 0 < \phi < 2\pi$). The mode matching boundary is then defined as the surface: $0 < z < b,\ \rho = r_o,\ 0 < \phi < 2\pi$. All metal surfaces will be considered to be perfect electric conductors (PEC). The fields within the structure are represented by superpositions of radial waves (basis functions), which propagate in the radial direction forming standing waves. Their form can be derived using the boundary conditions and the radial waveguide field equations as described by Balanis (1988). In this structure these equations can be greatly simplified by removing the circumferential variations. This can be justified by realising that for the radial basis functions to describe the field patterns of the TEM transmission line, only those parts describing the radial and longitudinal variations are necessary. This means that the TE basis functions can be neglected as there is no E_z component, and consulting the differential equations for the TE radial fields (Balanis, 1988, p. 501), E_ρ and H_ϕ, which would be used to 'build up' a TEM mode, are zero as they are dependent on ϕ. The general form of the magnetic vector potential in the structure would then be:

$$A_z(\rho,\phi,z) = (C_1 J_i(\beta_\rho \rho) + D_1 Y_i(\beta_\rho \rho))(C_2 \sin(\beta_z z) + D_2 \cos(\beta_z z)) \cdot (C_3 \sin(i\phi) + D_3 \cos(i\phi)) \quad (3.1)$$

and, using the simplification just described, the transverse magnetic (TM) radial basis function fields can then be derived from:

$$A_z(\rho,\phi,z) = (C_1 J_0(\beta_\rho \rho) + D_1 Y_0(\beta_\rho \rho))(C_2 \sin(\beta_z z) + D_2 \cos(\beta_z z)) \quad (3.2)$$

where $i = 0$ due to no circumferential variation.

3.2.1 Radial TM Basis Functions

Region I

Using equation (3.2) and the appropriate boundaries, the magnetic vector potential field equation for the gap between the conductive rod and the tuning screw can be shown to be:

$$A_{z_I}(\rho, z) = A_k^{TM} J_0(\beta_{\rho_I}\rho)\cos(\beta_{z_I}(z - b_1)) \tag{3.3}$$

where:

$\beta_z = \left(\frac{k\pi}{b_2 - b_1}\right)$ due to the top and bottom PEC boundaries at the rod and tuning screw ends.

The wave number in the radial direction β_ρ is related to β_z, and to the wave number of the medium β_0, by the equations:

$$\beta_\rho^2 = \beta_0^2 - \beta_z^2; \qquad \beta_0^2 = \omega^2\mu_0\varepsilon_0\varepsilon_r \tag{3.4}$$

and the Bessel functions of the second kind (Y_0) are infinite at $\rho = 0$ and are therefore not part of the solution.

The TM basis function component equations for region I are then found from the differential equations provided by Balanis (1988, p. 503). A summary of these are presented in Appendix A.

Region II

E_z will be zero at the tangential outer cylindrical boundary $\rho = a$. This field component is related to the potential function by:

$$E_z = -j\frac{1}{\omega\mu\varepsilon}\left(\frac{\partial^2}{z^2} + \beta^2\right)A_z \tag{3.5}$$

Using equations (3.2) and (3.5) and working backwards from the outer wall PEC boundary the potential function for region II must have the form:

$$A_{z_{II}}(\rho, z) = B_n^{TM}(Y_0(\beta_{\rho_{II}}a)J_0(\beta_{\rho_{II}}\rho) - J_0(\beta_{\rho_{II}}a)Y_0(\beta_{\rho_{II}}\rho))\cos(\beta_{z_{II}}z) \tag{3.6}$$

where:

$\beta_{z_{II}} = \left(\frac{n\pi}{b}\right)$ due to the top and bottom PEC boundaries at the outer cylinder end

plates. The wave number in the radial direction $\beta_{\rho_{II}}$ is related to $\beta_{z_{II}}$, and to the wave number of the medium β_0, by the equations:

$$\beta_{\rho_{II}}^2 = \beta_0^2 - \beta_{z_{II}}^2; \qquad \beta_0^2 = \omega^2 \mu_0 \varepsilon_0 \varepsilon_r \tag{3.7}$$

The TM basis function component equations for region II are then found from the differential equations provided by Balanis (1988, p. 503). A summary of these are presented in Appendix A.

If the radial wave number β_ρ is imaginary, then the basis function is non propagating, and the fields will decay exponentially in the radial direction. This can occur in both regions, and with either basis function type. In this case the Bessel functions J_0 and Y_0 for that particular basis function will have to be changed to modified Bessel functions I_0 and K_0 respectively.

3.2.2 Mode Matching at the Boundary Between Regions

To find a field solution to the current problem the transverse (tangential) E and H fields in both regions must be matched at the cylindrical boundary $\rho = r_o$. Each field component is represented by a summation of radial basis functions. Matching the transverse electric fields across the boundary between regions I and II leads to:

$$\mathbf{E} = A_p^{TM} \sum_{p=1}^{\infty} \mathbf{E}_I^{TM} = B_q^{TM} \sum_{q=1}^{\infty} \mathbf{E}_{II}^{TM} \tag{3.8}$$

where the TM basis function in region I is identified by p and the TM basis function in region II is identified by q.

Similarly, the transverse magnetic fields will be matched if the following condition holds:

$$\mathbf{H} = A_p^{TM} \sum_{p=1}^{\infty} \mathbf{H}_I^{TM} = B_q^{TM} \sum_{q=1}^{\infty} \mathbf{H}_{II}^{TM} \tag{3.9}$$

The above pair constitutes a doubly infinite set of linear equations for the modal coefficients A_p and B_q. To simplify these, and provide good convergence, the following

orthogonality relation (inner product), as applied by Yao (1995), was used.

$$< \mathbf{E}_m, \mathbf{H}_n > = \int_S (\mathbf{E}_m \times \mathbf{H}_n) \cdot d_s = 0 \quad if\ m \neq n \tag{3.10}$$

This is applied to both equations (3.8) and (3.9). Firstly, form the cross-product of equation (3.8) and a testing function from the magnetic field of region II and integrate over the inner cylindrical surface of region II:

$$< \mathbf{E}, \mathbf{h}_{q_{II}} >= \int_0^b \int_0^{2\pi} (\mathbf{E} \times \mathbf{h}_{q_{II}}) \cdot \hat{\rho}\, r_o d\phi dz \tag{3.11}$$

For no circumferential variations this then becomes:

$$< \mathbf{E}, \mathbf{h}_{q_{II}} >= \int_0^b (\mathbf{E} \times \mathbf{h}_{q_{II}}) \cdot \hat{\rho}\, dz \tag{3.12}$$

Secondly, form the cross-product of equation (3.9) and a TM testing function from the electric field of region I and integrate over the outer cylindrical surface of region I:

$$< \mathbf{e}_{p_I}, \mathbf{H} >= \int_{b_1}^{b_2} \int_0^{2\pi} (\mathbf{e}_{p_I} \times \mathbf{H}) \cdot \hat{\rho}\, r_o d\phi dz \tag{3.13}$$

For no circumferential variations this then becomes:

$$< \mathbf{e}_{p_I}, \mathbf{H} >= \int_{b_1}^{b_2} (\mathbf{e}_{p_I} \times \mathbf{H}) \cdot \hat{\rho}\, dz \tag{3.14}$$

Therefore the testing functions required are only the z dependent factors of the basis functions.

The infinite set of linear equations so formed is then reduced, by truncating the number of basis functions used, to a value that will give a desired solution accuracy. This is possible because the basis functions tend to taper in dominance from lower to higher order, providing convergence to near the exact value for relatively few basis functions used. However numerical problems, such as relative convergence, associated with the truncation of the set equations do occur. See section 3.6. A summary of the integrals in these equations is shown in Appendix A.4.

The resultant equations in matrix form for the electric field are:

$$\begin{bmatrix} a_{11} & \cdots & a_{1p} \\ \vdots & \ddots\, TM_{E_z}^{(I)} TM_{h_\phi}^{(II)} & \vdots \\ a_{q1} & \cdots & a_{qp} \end{bmatrix} \begin{bmatrix} A_1^{TM} \\ \vdots \\ A_p^{TM} \end{bmatrix} = \begin{bmatrix} b_{11} & \cdots & 0 \\ \vdots & \ddots\, TM_{E_z}^{(II)} TM_{h_\phi}^{(II)} & \vdots \\ 0 & \cdots & b_{qq} \end{bmatrix} \begin{bmatrix} B_1^{TM} \\ \vdots \\ B_q^{TM} \end{bmatrix} \tag{3.15}$$

or in an abbreviated form

$$[\mathbf{W}][\mathbf{A}] = [\mathbf{X}][\mathbf{B}] \tag{3.16}$$

The magnetic field equations are:

$$\begin{bmatrix} a_{11} & \cdots & 0 \\ \vdots & \ddots\, TM_{H_\phi}^{(I)} TM_{e_z}^{(I)} & \vdots \\ 0 & \cdots & a_{pp} \end{bmatrix} \begin{bmatrix} A_1^{TM} \\ \vdots \\ A_p^{TM} \end{bmatrix} = \begin{bmatrix} b_{11} & \cdots & b_{1q} \\ \vdots & \ddots\, TM_{H_\phi}^{(II)} TM_{e_z}^{(I)} & \vdots \\ b_{p1} & \cdots & b_{pq} \end{bmatrix} \begin{bmatrix} B_1^{TM} \\ \vdots \\ B_q^{TM} \end{bmatrix} \tag{3.17}$$

and in abbreviated form

$$[\mathbf{Y}][\mathbf{A}] = [\mathbf{Z}][\mathbf{B}] \tag{3.18}$$

The elements of [**W**] and [**Y**] are the result of the inner products on the LHS of equations (3.8) and (3.9) respectively, and those of [**X**] and [**Z**] are the results of the inner product on the RHS of the same equations. [**X**] and [**Y**] are diagonal matrices. [**A**] and [**B**] are the unknown coefficients. These equations can then be used to solve for the resonant frequencies of the structure or to find the unknown coefficients of the field equations.

3.2.3 Resonant Frequencies of the Structure

An efficient system of homogeneous equations may be formed from equations (3.16) and (3.18) by eliminating either the [**A**] or the [**B**] coefficients. It is preferable to eliminate [**B**], because this leads to a smaller matrix.

$$\left[[\mathbf{Y}]^{-1}[\mathbf{Z}][\mathbf{X}]^{-1}[\mathbf{W}][\mathbf{A}]\right] = 0 \tag{3.19}$$

As [**X**] and [**Y**] are both diagonal matrices their inverses are easy to obtain, ie invert each diagonal element. The eigenvalues of equation (3.19) are the resonant frequencies

of the structure and these can be determined by finding the frequencies at which the determinant of the overall matrix is zero. In this lossless case the elements of the matrix are all real.

3.2.4 Radial Basis Function Coefficients

To check that the mode matching solution is physically sensible, it is good practice to calculate and plot the field patterns. Also in high power applications, there may be a requirement to determine the peak electric field strength within the structure, to check if dielectric breakdown is likely. In order to plot these patterns, the coefficients of the radial basis function field expansions must first be determined. The unknown coefficient equations (3.16) and (3.18) can be rearranged into the form

$$\begin{bmatrix} \mathbf{W} & -\mathbf{X} \\ \mathbf{Y} & -\mathbf{Z} \end{bmatrix} \begin{bmatrix} \mathbf{A} \\ \mathbf{B} \end{bmatrix} = 0 \tag{3.20}$$

A selected coefficient is then chosen as unity or some appropriate factor. In the program that was written the chosen coefficient was the first TM basis function in region II (B_1^{TM}). Consequently the associated inner product values are b_{11}^{TMTM} to b_{q1}^{TMTM}. The $\mathbf{B}$ coefficients are reduced by one to $\mathbf{B}_r$ and $\mathbf{X}$ and $\mathbf{Z}$ matrices are reduced by a column to $\mathbf{X}_r$ and $\mathbf{Z}_r$. Hence equation (3.20) can then be written as:

$$\begin{bmatrix} \mathbf{A} \\ \mathbf{B}_r \end{bmatrix} = \begin{bmatrix} \mathbf{W} & -\mathbf{X}_r \\ \mathbf{Y} & -\mathbf{Z}_r \end{bmatrix}^{-1} \begin{bmatrix} b_{11}^{TMTM} \\ \vdots \\ 0 \\ b_{11}^{TMTM} \\ \vdots \\ b_{q1}^{TMTM} \end{bmatrix} \tag{3.21}$$

The system of equations (3.21) has more equations than unknowns (ie overdetermined) but can still be solved for the normalised values of the unknown coefficients by matrix inversion or the use of QR decomposition provided by the Matlab operator '\'. This function has the advantage that it gives a least squares solution of the basis function truncated equations, and so produces a best fit result (Penny & Lindfield, 1995).

Once the coefficients are found they can then be substituted into the field equations, so that the field components can be determined from the sum of the basis functions at a number of spatial grid points, and the resultant field in the structure can be plotted as a superposition of the components.

3.3 Mode Matching Computer Program for Resonant Frequency Calculation

The programing steps to find the TEM mode resonant frequencies in a coaxial resonator are shown in the flow chart of Figure 3.3 and the details are as follows:

1. Allocate resonator dimensions, relative permittivity of regions I and II, general constants, number of basis functions used in each region and calculation of the coupling integrals for all the combinations of the basis functions and testing functions as described by expressions (3.12) and (3.14).

2. Provide a 'for' loop of the frequency range in which the resonator is thought to have resonances. The resonances can be estimated by calculating the inductive reactance of a shorted length of coaxial line (length of the inner rod) using transmission line formula and resonating this with capacitance calculated by an approximate parallel plate capacitance model of the resonator end gap.

3. Provide a 'for' loop of the region I basis functions indices.

4. Calculate the radial wave propagation coefficient β_{ρ_I} of the current region I basis function.

   Calculate the ρ directed Bessel function factors of the region I basis function E_{z_I} and H_{ϕ_I} of the current region I basis function. If the basis function is propagating use the Bessel functions of the first kind J and their derivatives or if evanescent use the modified Bessel functions of the first kind I and their derivatives [2].

[2] When the arguments for J become imaginary (evanescent modes) this is equivalent to using I with real arguments. The latter was adopted in the program for convenience.

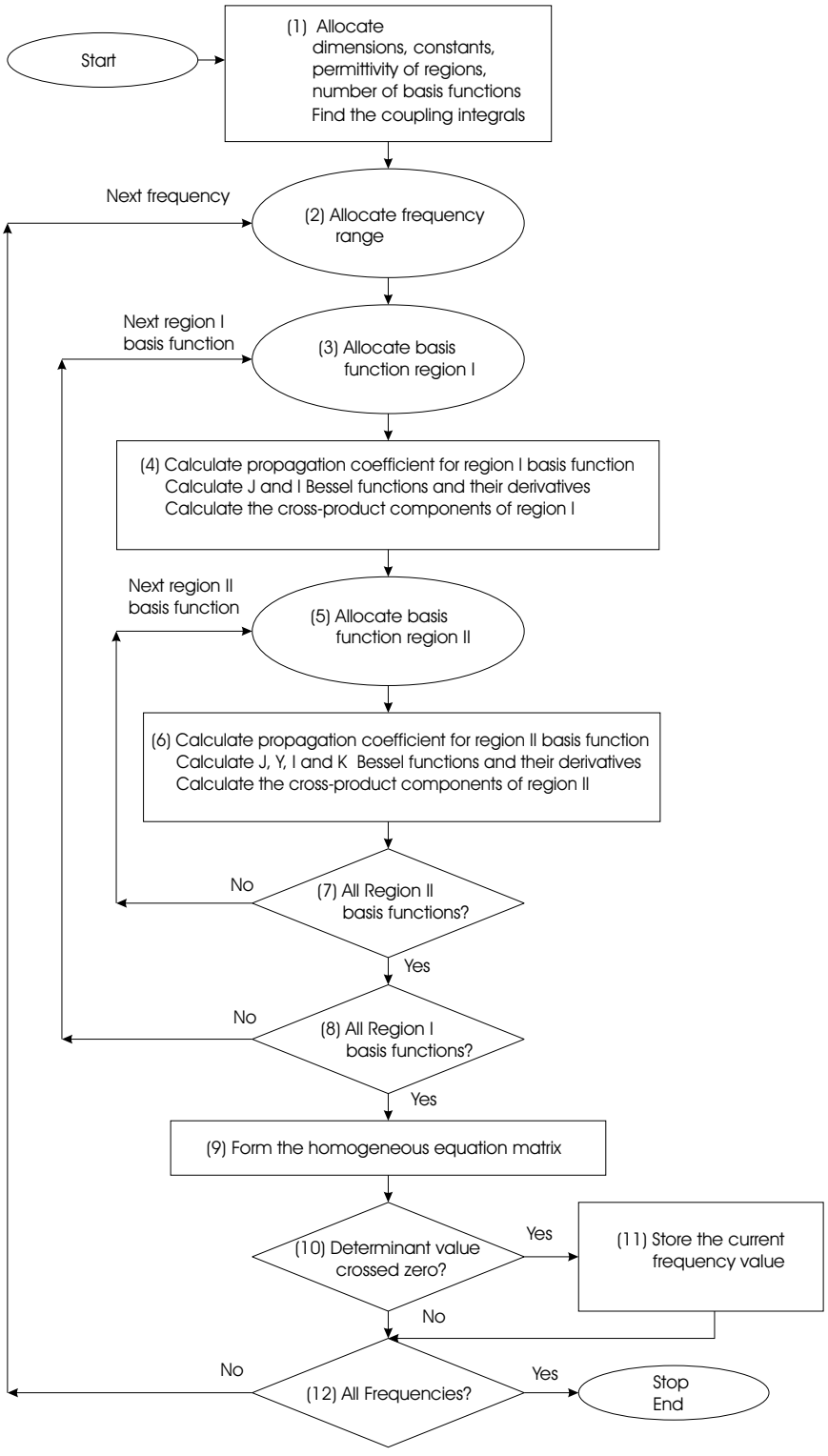

Figure 3.3: Flow chart of the mode matching program to find the TEM mode resonant frequencies of the coaxial resonator

Using these Bessel function factors calculate the integrated cross-product element of the region I basis function H_{ϕ_I} and the region I testing function e_{z_I}.

5. Provide a 'for' loop of the region II basis functions indices.

6. Calculate the radial wave propagation coefficient $\beta_{\rho_{II}}$ of the current region II basis function.

   Calculate the ρ directed Bessel function factors of the region II basis functions $E_{z_{II}}$ and $H_{\phi_{II}}$ of the current region II basis function. If the basis function is propagating use the Bessel functions of the first kind J and second kind Y and their derivatives or, if evanescent, use the modified Bessel functions of the first kind I and second kind K and their derivatives [3].

   Using the Bessel function factors from step 4 calculate the integrated cross-product elements of the region I basis function E_{z_I} and region II testing function $h_{\phi_{II}}$. Using the Bessel function factors from this step calculate the remaining integrated cross-product elements, $E_{z_{II}}$ and $h_{\phi_{II}}$, and $H_{\phi_{II}}$ and e_{z_I}. The equations used in steps 4 and 6 are the result of the appropriate orthogonality relations presented in section 3.2.2 and are shown in full in Appendix A.

7. Repeat steps 5 and 6 until all the allocated region II basis functions are used with the current region I basis function.

8. Repeat for the next region I basis function until all allocated region I basis functions are used for the current frequency.

9. Use the cross-product elements calculated for this frequency to form the homogeneous set of linear equations in the form of matrix equation (3.19).

10. Check to see if the trend suggested by the current determinant value, of the LHS of equation (3.19), and the previous value, indicate that zero has been crossed.

11. If so, store the current frequency value as a resonant frequency (eigenvalue) of the coaxial resonator.

[3] When the arguments for J and Y become imaginary (evanescent modes) this is equivalent to using I and K with real arguments. The latter was adopted in the program for convenience.

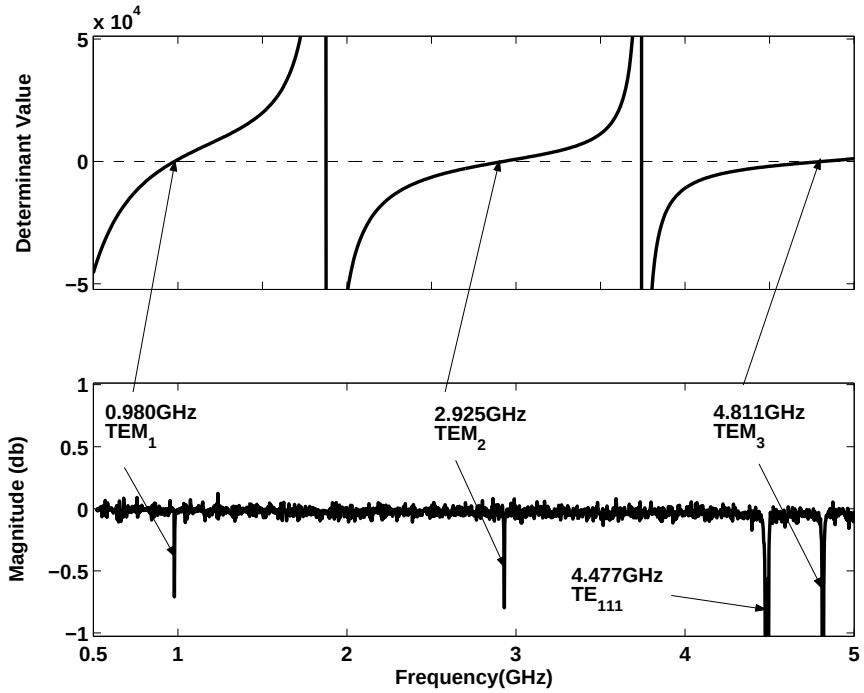

Figure 3.4: Resonant frequencies of the coaxial resonator calculated from mode matching program (top) and measured S_{11} data (lower). Frequency resolution = 2.8MHz. a = 17.42mm, b = 80mm, b_1 = 0mm, b_2 = 10mm, r_0 = 5.65mm, region I basis functions = 5, region II basis functions = 40

12. Allocate the next frequency value until all frequencies have been used.

The accuracy of this method is therefore dependent on the size of the steps in the allocated frequency range. To speed up the process the resonant frequencies were initially calculated roughly using large steps. The resonant frequencies were then determined, to the required accuracy, by dividing the range between the each rough frequency and its previous coarse step into much smaller steps and re-running the program. For a lossless coaxial resonator the elements of equation (3.19) are always real and therefore so is its determinant value. A typical set of determinant values calculated over a range of frequencies is shown in the top graph of Figure 3.4. The zero crossings indicate the first three TEM resonances calculated for the test resonator of section 3.4. For comparison the lower graph shows the magnitude of a reflection coefficient S_{11} measurement verses frequency using a vector network analyser. The TEM calculated and measured resonant frequencies are within 0.2%. The lower graph also shows a resonance of the

coaxial TE_{11} mode (see section 3.5, last paragraph) which is not modeled by the simplified mode matching procedure. This TE_{111} resonator mode is the most dominant of the TE and TM coaxial modes which are cut-off below 4.22GHz in this structure (Pozar, 1998, pp.143-145).

The magnitude of the reflection coefficient S_{11} shown in Figure 3.4 will be dependent on the degree of impedance mismatch between the network analyser and the resonator at the resonant frequencies. This will depend on a number of factors such as the length of the probe and its orientation in the field. Both of these will vary the degree of coupling. For the same length probe the coupling will be different for the different resonant modes and hence the respective magnitudes of the reflection coefficients will vary. The length of the probe used was a compromise between providing a large enough value for sufficient pick up of the fields (to allow low noise measurement) and small enough so as not to perturb the resonator fields and change the resonant frequencies significantly.

A copy of the computer program described in this section can be seen on the companion CD-ROM for this thesis and operating details are given in Appendix D.

3.4 Comparison of Calculated and Measured Results

A number of mode matching calculations were performed to determine the resonant frequencies of the lowest order TEM mode for various gap sizes $(b_2 - b_1)$. A sufficient overall number of basis functions were used to allow convergence of the resonate frequency to a value that changed by less than 1MHz, when compared to the previous value obtained with less basis functions.

A single coaxial resonator was constructed (as shown in Figure 3.5), so that S_{11} measurements could be made with a vector network analyser (50 ohm input impedance). The frequencies of the resonances obtained from the S_{11} data could then be compared with calculated values. The mechanical dimensions were constrained by the use of

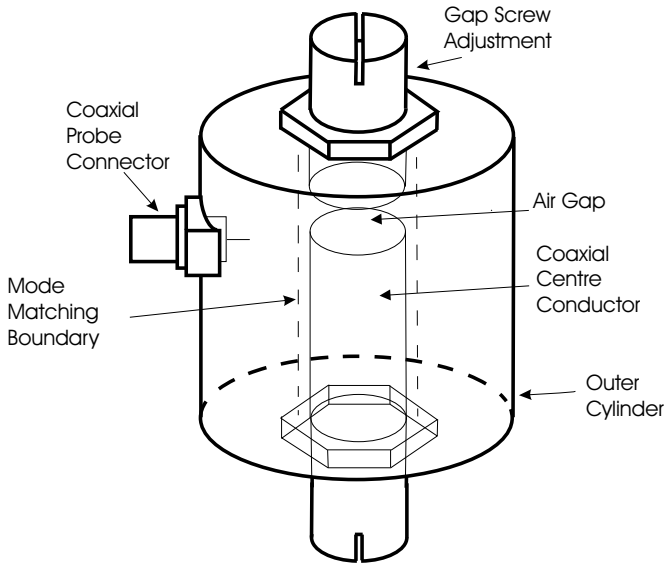

Figure 3.5: Single Coaxial Resonator used in Measurements ($r_o = 0.565$cm, $a = 1.742$cm, $b = 8$cm)

readily available materials, so that the inner and outer radii are $r_o = 0.565$ cm and $a = 1.742$ cm respectively.

The ratio a/r_o is 3.0832, corresponding to a characteristic impedance of 67.5Ω which is not quite optimum for minimum attenuation due to conductor loss. The equation for the attenuation of a coaxial line is given by Sander (1987) as:

$$\alpha_c = \frac{1}{2}\frac{R_s}{\eta b}\left(1 + \frac{b}{a}\right) \Big/ \ln\left(b/a\right)$$

where
$R_s = \left(\omega\mu/2\sigma\right)^{1/2}$, $\eta = \sqrt{\mu/\varepsilon}$ and b and a are the radii of the outer and inner conductors respectively.
From Sander (1987, p. 24) this function has a minimum when

$$\ln\left(b/a\right) = 1 + a/b$$

and from this the optimum value of b/a for minimum attenuation due to conductor loss (or in the case of this structure a/r_o) can be found to be 3.591.

The coaxial connector, shown in Figure 3.5, was located 1/3 of the length of the outer cylinder from the gap end.

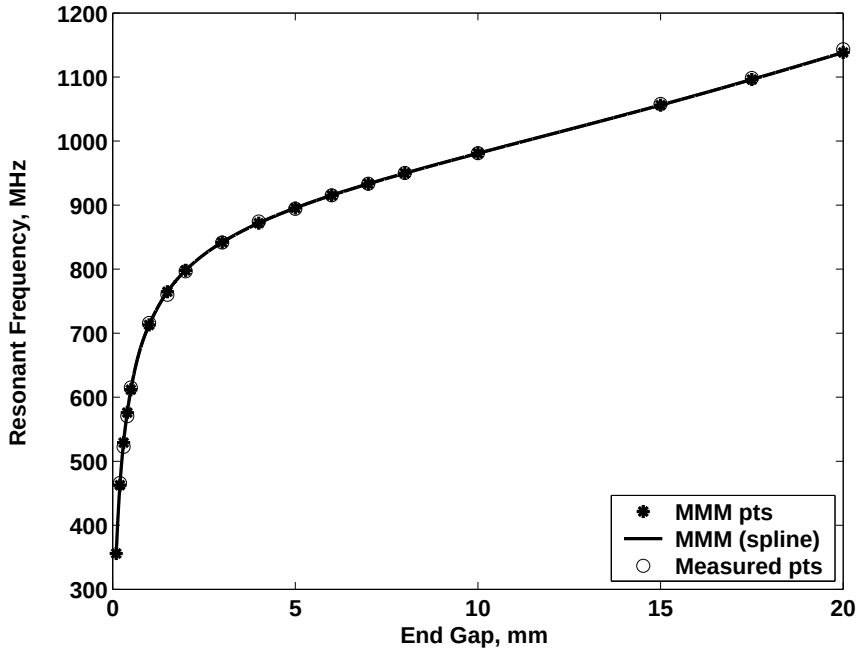

Figure 3.6: Single coaxial resonator resonant frequencies, $b_1 = 0$ mm and b_2 varied from 0 to 20 mm ($r_o = 0.565$cm, $a = 1.742$cm, $b = 8$cm)

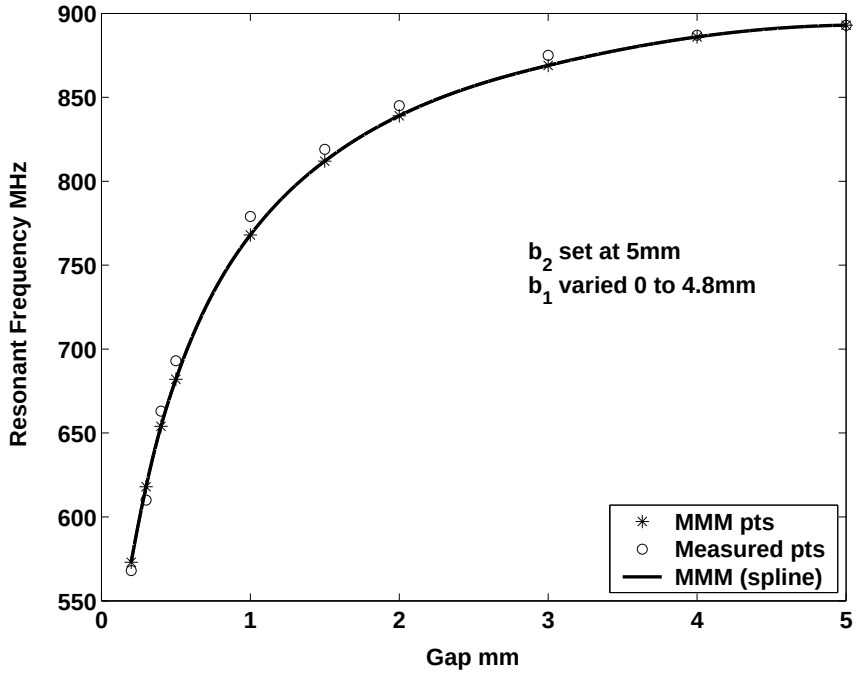

Figure 3.7: Single coaxial resonator resonant frequencies with adjustment of tuning screw, $b_2 = 5$ mm and b_1 varied from 0 to 4.8 mm ($r_o = 0.565$cm, $a = 1.742$cm, $b = 8$cm)

The probe of the connector lay in the direction of the ρ co-ordinate so that the expected radial electric field of the TEM mode would coincide with it. The 1/3 distance was used as it was thought that the amplitudes of the TEM fundamental and first few lower order electric fields would be of sufficient value at this point for a low noise S_{11} measurement ie far enough away from any nulls.

Both the measured and calculated results obtained, with the tuning screw penetration set to zero ($b_1 = 0$), are shown in Figure 3.6. The variation in gap size was obtained by increasing b_2 from 0.1 to 20mm . On this scale the mode matching results cannot be distinguished from the measured results. Typically, the difference between them is of the order of 1%. Another set of calculations and measurements were performed with b_2 = 5mm and $b_1$was varied from 0 to 4.8mm to simulate adjustment of the tuning screw. The results are shown in Figure 3.7. The calculated results are within 2% of the measured values. The larger difference in values compared to the previous example was found to be due to increased difficulty in setting the b_1 and b_2 distances accurately in the test resonator.

3.5 Discussion

It is useful to interpret the results shown in Figure 3.6 in terms of the transmission line equivalent circuit shown in Figure 3.1. The capacitance Cg for the gap g can be calculated from the resonant frequency and the inductive reactance of the shorted length of coaxial line. Since the capacitance is proportional to the overall size of the structure, it is convenient to normalise the capacitance values, by dividing them by one of the radial dimensions. In this case the radius of the inner conductor was used. A graph of both the calculated and measured results, presented in this format, is shown in Figure 3.8. The calculated results agree very well with measured results, the difference being of the order of 1%. To minimise the coaxial conductor loses, and maximise the Q factor of the resonator, the optimum ratio of the radii is a/r_o=3.591 corresponding to a characteristic impedance of 76.6 Ω.

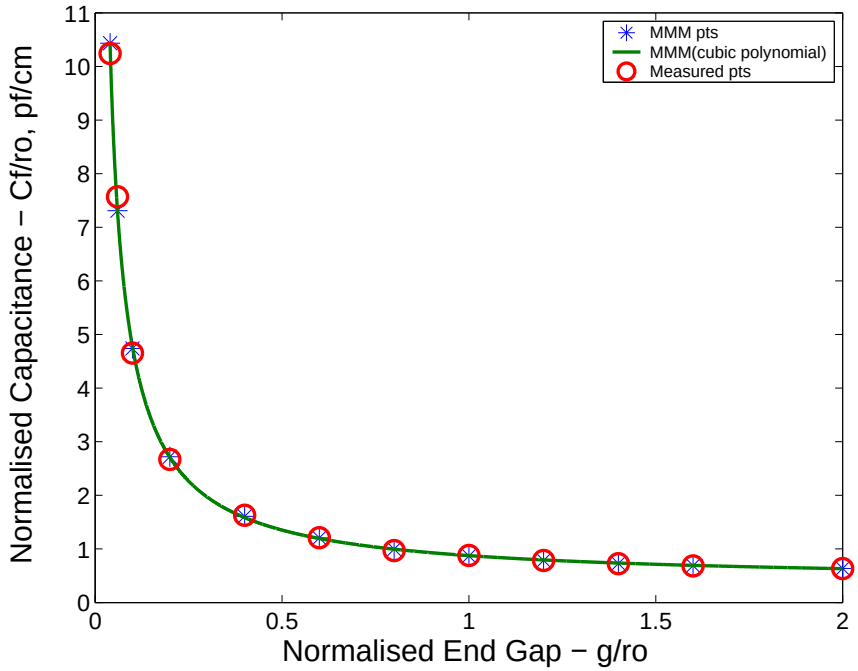

Figure 3.8: Normalised Capacitance vs Normalised End Gap ($b2 = 0$, end gap(g) = $b1$, $a/r_o = 3.0832$)

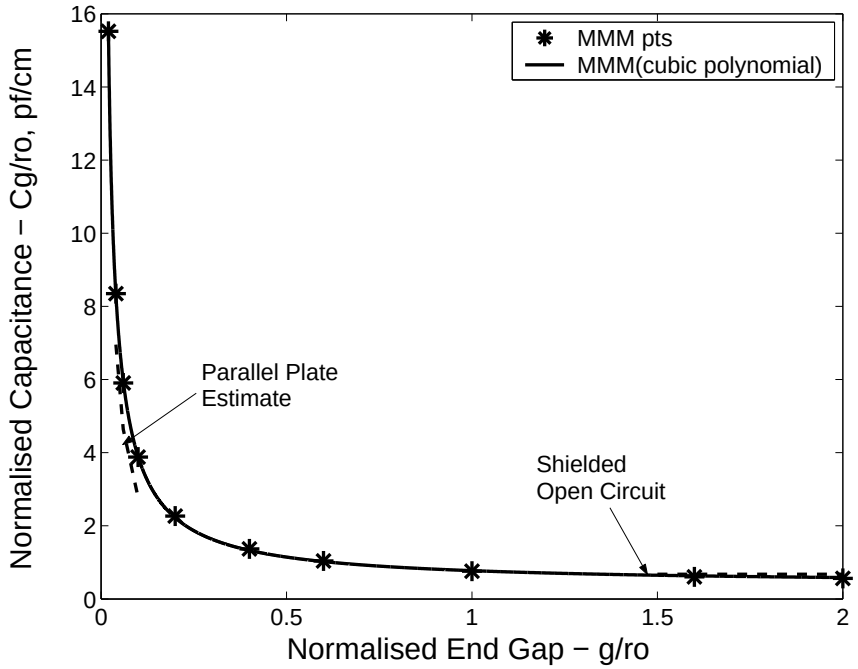

Figure 3.9: Comparison of the calculated polynomial curve of the normalised gap capacitance with parallel plate and shielded open circuit estimates. Normalised Capacitance vs Normalised End Gap ($b_2 = 0$, end gap(g) = b_1, $a/r_o = 3.591$)

For this characteristic impedance, a normalised graph of calculated capacitance versus gap size g is shown in Figure 3.9. The curve is the result of a least squares cubic polynomial fitted to the calculated points, and is of the form:

$$\frac{C_g}{r_o} = a_o + \frac{a_1}{\left(\frac{g}{r_o}\right)} + \frac{a_2}{\left(\frac{g}{r_o}\right)^2} + \frac{a_3}{\left(\frac{g}{r_o}\right)^3} \tag{3.22}$$

where $a_o = 0.1977$, $a_1 = 0.09551$, $a_2 = -4.5 \times 10^{-4}$, $a_3 = 2.5 \times 10^{-6}$ and the norm of the residuals is 0.0451.

It is constructive to compare the values of capacitance for large and small gaps to those obtained from other sources. For small gaps the parallel plate value of capacitance calculated from the inner conductor end area and gap distance can be used. The normalised value for a 0.02 cm gap (0.04 normalised) is 6.954 and this can be compared to the calculated value of 8.348 when the fringing effects are taken into account. A few values for the parallel plate approximation are plotted in Figure 3.9. For larger gaps Rizzi (Rizzi, 1998) states that the plane of the coaxial open circuit is approximately $0.6(a - r_o)$ past the end of the inner conductor. For the coaxial line used in this section this length works out to be 0.777 cm. Using the Zo of the line a normalised capacitance of 0.676 can be calculated. This compares favorably to the value (0.561) from mode matching for large gaps plotted in the figure.

A further source of validation is that obtained from the Waveguide Handbook (Marcuvitz, 1951, p. 178). The equation:

$$BZ_0 = \frac{4b}{\lambda} \ln\left(\frac{a}{b}\right) \left(\frac{\pi}{4}\frac{b}{r_o} + \ln\frac{a-b}{r_o}\right) \tag{3.23}$$

gives the normalised susceptance of an infinite length coaxial line terminated by a capacitive gap where λ is the wavelength in free space. Approximate values of gap capacitance for the resonator can be calculated from $C = \omega B$ using the resonant frequencies calculated by mode matching. A comparison with the previous cubic polynomial curve is shown in Figure 3.10 . One of the restrictions on the Marcuvitz formulation is that $\frac{g}{a-r_0} \ll 1$. This means in this example that $g \ll 2.6$ normalised. The effect of this can be seen from the figure where the Marcuvitz points stray markedly from the polynomial

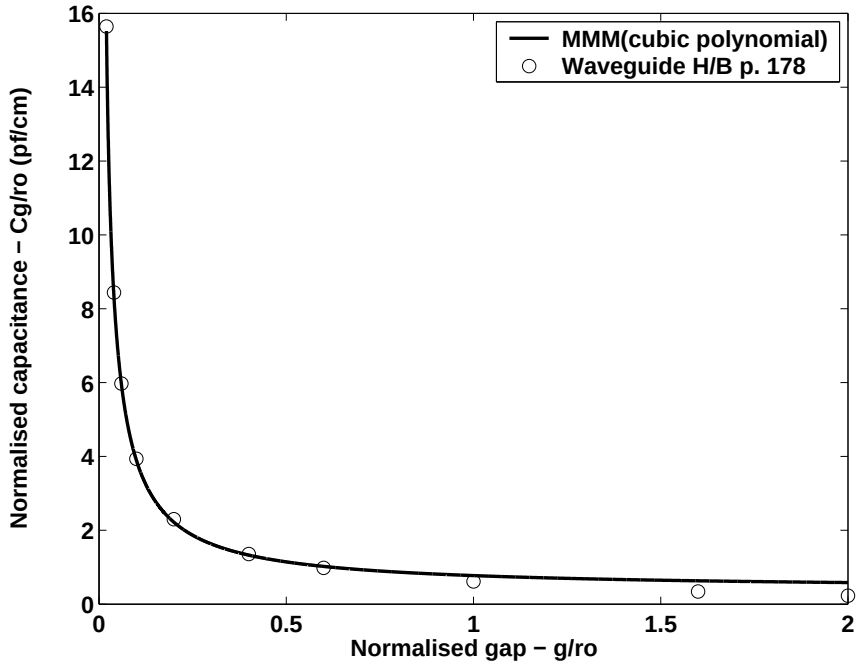

Figure 3.10: Comparison of the calculated polynomial curve of the normalised gap capacitance with results from the Waveguide Handbook. Normalised Capacitance vs Normalised End Gap.($b_2 = 0,$ end gap(g) $= b_1,$ $a/r_o = 3.591$).

above a normalised gap of about 1. Below 0.25 the Marcuvitz points are within 2% of the polynomial curve. The formula from Marcuvitz appears to be a good approximation for small gaps but, of cause, it does not allow for a the use of a tuning screw. In a coaxial resonator situation it also requires the calculation of the resonant frequency before the capacitance can be calculated.

When the measurements were performed the measuring equipment was connected to the cavity by means of a small probe, as shown in Figure 3.6. Since the probe couples to the radial electric field of the coaxial TEM mode and introduces asymmetry into the cavity, it will also excite higher order coaxial modes having circumferential variation. As referred to previously in section 3.3 the first of these to propagate (TE_{11}) has a cut-off frequency of 4.22GHz, so they will all be well below cut-off over the measured frequency range (Pozar, 1998). Hence although they contribute to the local field of the probe, they will have otherwise little effect.

3.6 The Limitations of the Coaxial Resonator Mode Matching Solution

3.6.1 Resonant Frequency Calculation

One of the difficulties in obtaining an accurate mode matching solution is the problem of relative convergence (Mittra & Lee, 1971) (Leroy, 1983). This problem is a consequence of the truncation of the theoretical infinite number of basis functions existing in each region to some practical value. It was found that for good convergence, a ratio of region I to region II basis functions (basis function region ratio BFRR), close to the ratio of the heights of the regions, was required. This can be determined from the expression:

$$\frac{n}{m} = \frac{b_2 - b_1}{b} \tag{3.24}$$

where n and m are the number of basis functions used in regions I and II respectively. Proof of better convergence for this criteria can be seen in Figure 3.11 for a BFRR of 1/8. This value coincides with the region height ratio of 1/8 (ie 10mm/80mm). It is interesting to note that the other basis function region ratio examples converge to nearly the same value. This confirms the premise in literature that as long as the number of basis functions are high the numerical result will converge to near the correct value (Itoh, 1989, p. 613). In real terms the three examples in the figure all converge to within 0.3% of the measured value (see section 3.4). The structure in this example has a height $b = 80$mm, $b_2 = 10$mm, $b_1 = 0$ (ie gap=10mm) and $r_0 = 5.65$mm.

The same basis function ratio criteria as described by equation (3.24) was used in Figure 3.12 where the convergence properties for a structure of different gap sizes is compared. It can be seen that relatively few basis functions in region I are required before good convergence occurs in both cases, however the number of basis functions required in region II for the 1mm gap has to be 10 times that of the 10mm gap.

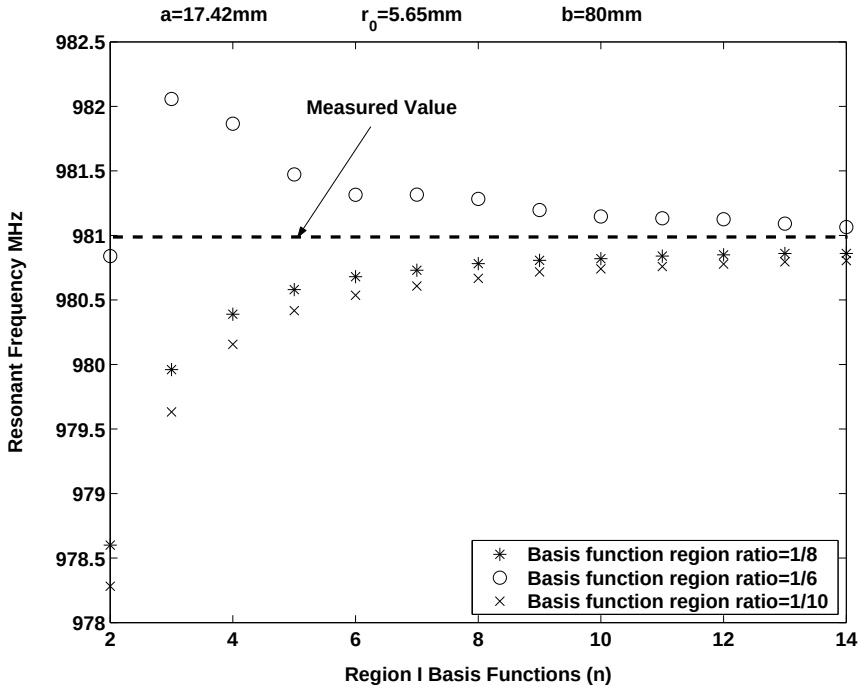

Figure 3.11: Resonant frequency convergence properties for different ratios of region I to region II basis functions. $b_2 = 10$mm, $b_1 = 0$ (ie gap=10mm)

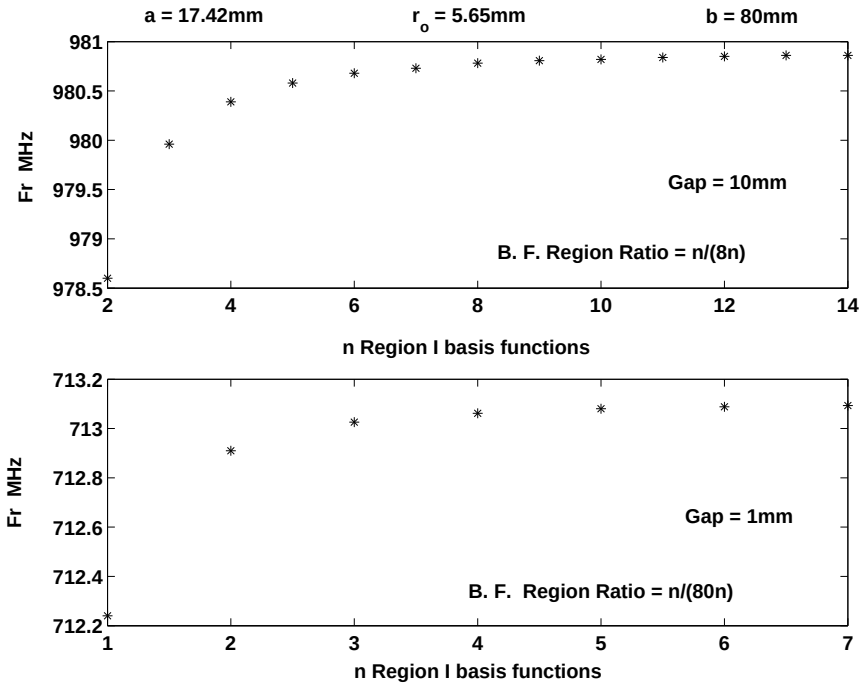

Figure 3.12: Resonant frequency convergence properties using the criteria of a basis function region ratio equal to the region height ratio, for different gap sizes.

Problems can arise for very narrow gaps (< 0.2mm in this case) where the higher order basis functions created have Bessel function values that can exceed the maximum or minimum possible floating point number of the computer. The matrix element operations created are considered mathematically undefined by the software (Matlab etc) and no solution can be given. For a 0.2mm gap the BFRR is 2/800 for the current case but only a 1/400 BFRR can be used before numerical problems occur. Up to a point the problem can be overcome by multiplying the row of the matrix containing the offending element by a suitable constant as this does not change the value of the determinant or, the region basis function ratio criteria can be relaxed somewhat sacrificing accuracy.

3.6.2 Unknown Coefficients and Field Plotting

It was found that there is a limit to the number of basis functions for which an unknown coefficient solution is feasible. Rank deficient matrices, giving inaccurate matrix inverse results, occurred when more than about 20 basis functions where used in region II. This is due again to the very large dynamic range of the element values in the matrix, which approach the limited numerical range of the computer. The element values in some rows are rounded off to the extent that they become indistinguishable with other rows creating the rank deficiency. Specifically the higher order basis function Bessel function values in the region II equations become very large and cause the problem. In any case, the number of basis functions that can be used is not sufficient to obtain results as accurate as the resonant frequencies of section 3.2.3 where only the value of the determinant of a matrix had to be found. However, it is sufficient to generate reasonably accurate field patterns as long as region height ratios are not less than about 1/8.

A magnified view of the electric field vectors in the vicinity of a 10mm gap is shown in Figure 3.13 and represents the superposition of 3 TM basis functions in region I, and 20 TM basis functions in region II. The cavity dimensions are: $a = 17.42$mm, $b = 80$mm, $r_0 = 6$mm. Some discontinuity may be seen at the boundary between the

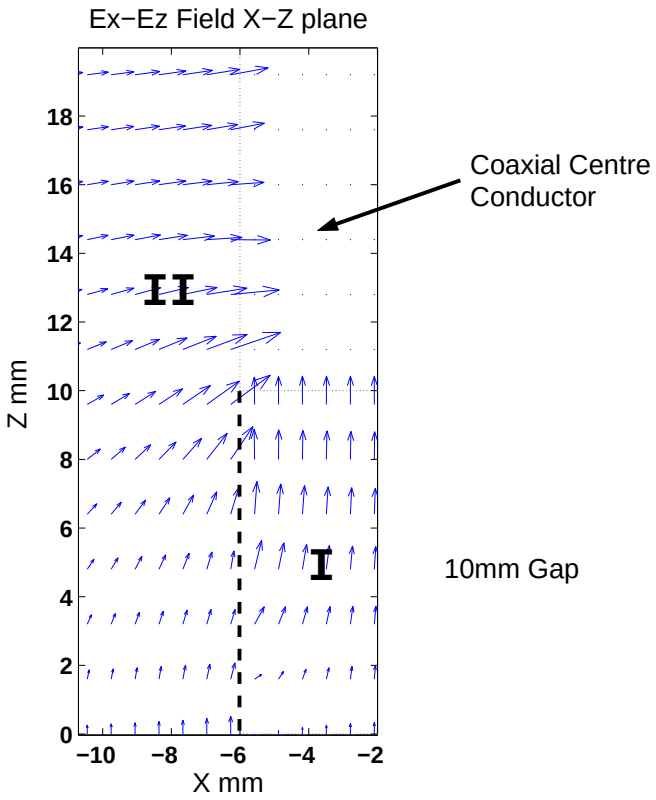

Figure 3.13: Ey - Ez Magnified Field Plot in the vicinity of a 10mm gap. a=17.42mm, b=80mm, r_0=6mm, BFRR=3/20, Fr=979.7MHz

regions in Figure 3.13 and this is more obvious when the matching of the E_ρ and E_z field components, at the mode matching boundary, are viewed as in Figure 3.14. For larger gaps the matching is much improved as shown by Figure 3.15 for a 40mm gap size.

As was the case when finding the resonant frequencies, it becomes more difficult to obtain accurate results as the gap size becomes smaller. For small gaps the preferred basis function region ratio, to satisfy relative convergence, can only be approached if the number of basis functions overall is also made low.

Another reason for the less than optimum matching over the boundary in Figures 3.14 and 3.15 is the singularity of the field component solutions at the bottom corners of the inner conductor.

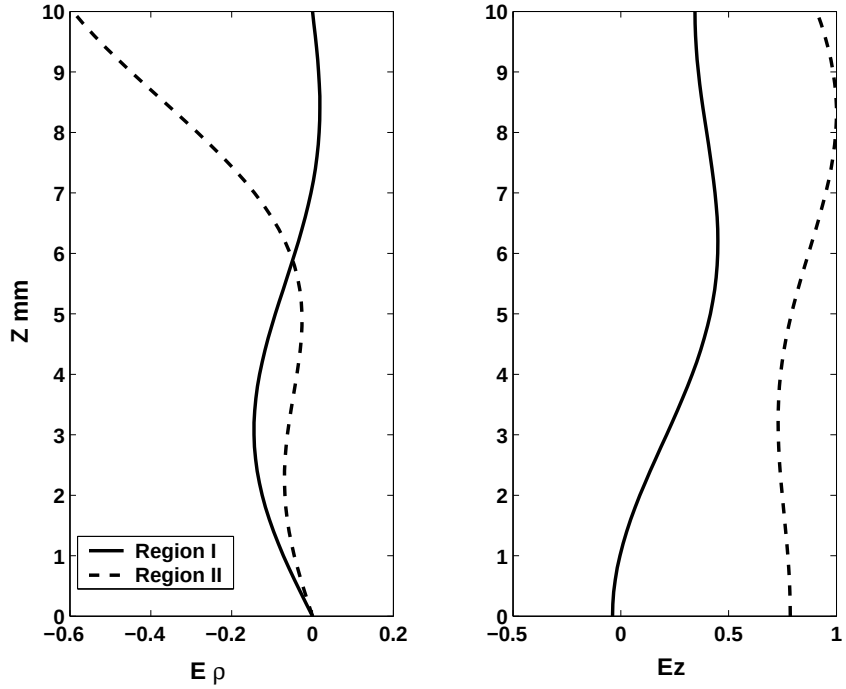

Figure 3.14: Matching of the normalised field components at the mode matching boundary for a 10mm gap. a=17.42mm, b=80mm, r_0=6mm, BFRR=3/20, Fr=979.7MHz

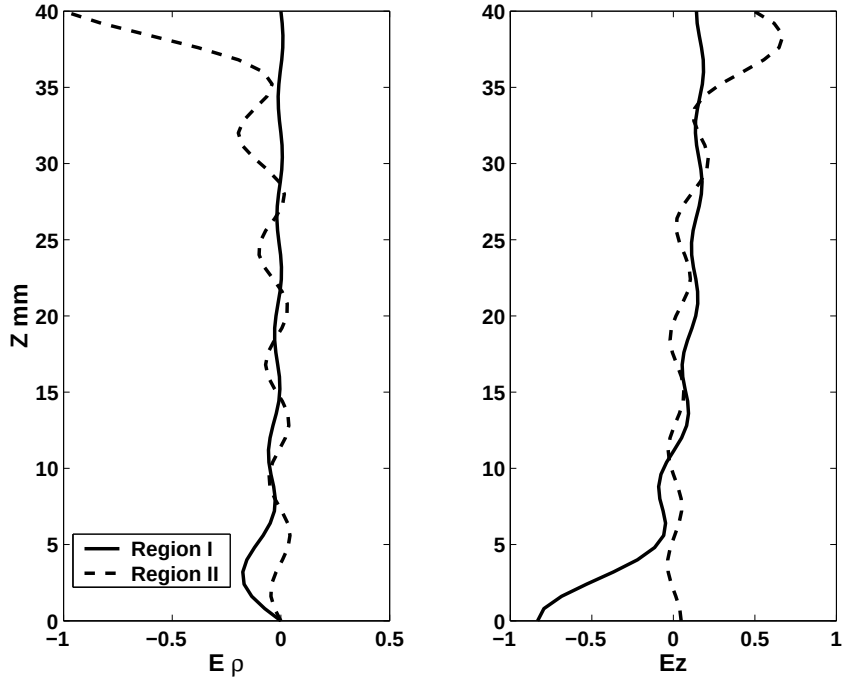

Figure 3.15: Matching of the normalised field components at the mode matching boundary for a 40mm gap. a=17.42mm, b=80mm, r_0=6mm, BFRR=11/22, Fr=1631.9MHz

The modeling of a this type of discontinuity with continuous basis functions can be likened to the Gibbs phenomenon in Fourier analysis where a series will converge slowly and exhibit oscillations near the discontinuity (Sudbo, 1992). In this case the discontinuity is an $r^{-1/3}$ singularity (Collin, 1991, p. 25) which describes the variation in the field solution for distance r from the corner.

3.7 Conclusion

In this chapter a simplified radial mode matching solution has been described which provides a numerically efficient method of calculating the TEM resonant frequency and gap capacitance of a coaxial resonator (Wells & Ball, 2004). Minimum conductor loss and hence maximum Q factor occur for a radii ratio $a/r_o = 3.591$. For this case the gap capacitance results are well represented by a best fit least squares cubic polynomial, which may be useful in design calculations.

The specific results reported can be applied to the calculation of gap capacitance, tuning range or temperature drift in coaxial resonators, as used in cellular base station multicavity filters. They may also be applied to the calculation of a coaxial open circuit end effect correction. The general method is also applicable to the calculation of the equivalent circuit of a gap in a coaxial centre conductor, and hence to the design of coaxial diode mounts.

This exercise in the analysis of the coaxial resonator has shown that there are some generic properties that are likely to be common to all mode matching solutions:

- The solution was found to be quite accurate when compared to measured results and those calculated from other methods.
- A solution of required accuracy could be obtained in only minutes on a standard personnel computer.

However:

- Accuracy and good convergence to a solution in eigenvalue problems can be difficult to maintain when the difference in size of the regions either side of the mode matching boundary is extremely large. This is because the number of basis functions in the larger region has to be kept below the limit where the maximum or minimum possible floating point number of the computer will be exceeded. It then becomes difficult to maintain the optimum basis function region ratio BFRR, and hence satisfy the relative convergence criteria.

- There can be matching difficulties close to boundary discontinuities, especially those where the field components become singular. These will compromise accuracy to some degree.

- When solving for unknown coefficients and field component intensities, large differences in region size can create the same difficulties as occurred with the eigenvalue problem. However in this case the required BFRR and the number of basis functions in each region will require further compromise (ie less than the optimum number of basis functions in the larger region) to prevent rank deficiencies that can occur in the equation matrix.

These limitations of the mode matching method for the coaxial resonator would seem to be general for MM and appear not to have been emphasised in literature.

Chapter 4

The Shielded Rectangular Dielectric Rod Waveguide

4.1 Introduction

Dielectric waveguides are an attractive alternative to metal waveguides at millimeter wave frequencies due to their lower propagation loss, lower cost and easier fabrication (Lioubtchenko et al., 2003). Rectangular dielectric waveguides form a large proportion of these and have uses in integrated optics and millimeter-wave integrated circuits, transmission lines and filter applications. However there has always been difficulty obtaining accurate propagation coefficients for the various modes on these structures. There is no closed form solution to the problem (Lioubtchenko et al., 2003) and the methods used either rely on approximations, as in the procedure originated by Marcatili (1969) and improved by Knox & Toulios (1970), or are numerical in nature. The main numerical techniques range from the circular harmonic analysis of Goell (1969), finite element (Rahman & Davies, 1984) (Valor & Zapata, 1995) and finite difference (Schweig & Bridges, 1984) procedures, to mode matching.

In this chapter a mode matching method will be developed to allow the computation of

the propagation coefficients and field patterns of the fundamental modes in a shielded rectangular dielectric rod waveguide. This structure has only partially been investigated in literature, in the form of the shielded dielectric image line (Strube & Arndt, 1985), and the full solution described in this chapter shows the result of the existence of a dominant mode and other fundamental modes not previously presented in public literature.

This work will give guidance on multimode problems and the understanding of losses in shielded rectangular resonators (pursued in Chapter 5 of this thesis). In addition this work could possibly be extended to a study of the cubic dielectric resonator.

The principal results of this chapter have been published in *IEEE Transactions on Microwave Theory and Techniques* (Wells & Ball, 2005*b*).

4.2 Background

Mode matching methods have been applied to the dielectric image line by Solbach & Wolff (1978), and to the homogeneous inverted strip guide by Mittra et al. (1980). The latter used a similar procedure to Solbach & Wolff (1978), with the mode-matching techniques developed by Mittra & Lee (1971).

In a very comprehensive paper, Strube & Arndt (1985) have applied the method of Solbach & Wolff (1978) to the shielded dielectric image line. The first part of their paper used this procedure, together with the inclusion of an extra electric wall, to analyze propagation on infinite shielded image guide. As well as propagating modes and evanescent modes, complex modes and backward[1] waves were identified and thoroughly investigated. Complex modes can only exist in pairs having complex conjugate propagation coefficients, and couple such that the total power flow is always reactive. The second part of their paper finds the scattering matrix of a transition from shielded

[1] A backward wave is defined as one in which the power flows in the opposite direction to the wavefronts.

dielectric image guide to rectangular waveguide, by matching the tangential fields at the interface. A comparison of measured and calculated S_{11} results were used to verify the method. The results obtained by Strube & Arndt (1985) correspond to those modes that can exist in the dielectric rod waveguide shown in Figure 4.1 when the x axis is an electric wall. However, these do not include some of the dominant modes, for which the x axis is a magnetic wall. To obtain the full set of modes for this waveguide it is necessary to consider all four types of symmetry.

An analysis of complex and backward waves in inhomogeneously filled waveguide has been carried out by Omar & Schunemann (1987). A method to predict the presence of complex modes in inhomogeneous lossless dielectric waveguide can be found in the paper by Marozowski & Mazur (1990).

An alternative mode matching (boundary element) method for the shielded dielectric rod waveguide, incorporating dyadic Green's functions, was also developed by Collin (1991, p. 454), (Collin & Ksienski, 1987). Only the results using a dielectric rod with a low value of relative permittivity ($\varepsilon_r = 2.22$) was presented.

A problem with numerical solutions is that they can suffer from slow convergence due to divergence of the electric field at the corners of the dielectric where the refractive index changes abruptly (Sudbo, 1992). However, for most purposes, a sufficient degree of convergence to the extrapolated solution (see sections 4.6.1 and 4.10.2) can still be obtained for a relatively small number of basis functions.

In a typical situation the permittivity of the dielectric ε_{r2} will be higher than the surrounding medium ε_{r1} (usually air) so that the electromagnetic fields will be concentrated in the dielectric, and the proportion outside it will decay away exponentially. The ability of a high permittivity material to contain and concentrate the fields, together with the availability of high Q temperature stable materials, has led to the development of the dielectric resonator as a filter element. In filter applications the dielectric resonators are often enclosed in metallic shields or cavities to prevent unwanted coupling, as shown in Figure 4.1. Cavity filters incorporating dielectric resonators are

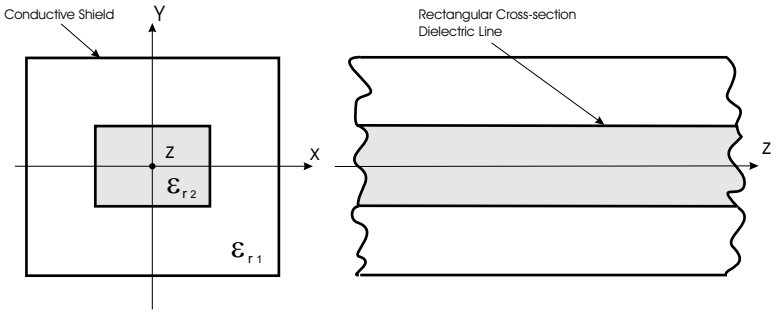

Figure 4.1: Rectangular dielectric line and shield.

widely used in mobile base stations and other demanding applications. Traditionally, many of these have used cylindrical resonators. Designers have sought to reduce the size of these filters, by using multiple mode cavities. This has led to increased interest in resonators that have a square cross-section, and also in cubical resonators. Dielectric filter cavities may be analysed using the methods developed by Zaki & Atia (1983). The propagation characteristics of an infinite cylindrical waveguide containing a dielectric rod were first established. Then a cylindrical cavity was modeled as a length of this guiding structure, terminated in short lengths of empty waveguide (Zaki & Atia, 1983). In a later paper this was extended to cylindrical dielectric resonators in rectangular waveguide and cavities (Liang & Zaki, 1993). This chapter represents the first step in a similar study of the shielded rectangular cross-section dielectric resonator.

4.3 The Designation of Modes for Dielectric Waveguides

Rectangular metallic closed waveguides, filled with a uniform dielectric material, have modes which are designated as transverse electric with respect to z or TE (H modes), and transverse magnetic or TM (E modes), where a double subscript specifies the number of half waves in the x and y directions. A subscript of zero specifies no variation.

Dielectric waveguides, however, consist of a high permittivity central core surrounded by a lower permittivity dielectric cladding (usually air). The boundary conditions created allow the coupling of the electric and magnetic longitudinal fields and so other

modal types are formed (Lioubtchenko et al., 2003).

For dielectric waveguides, with a core of circular cross-section, the modes can only be pure TE or TM with respect to z if they are independent of the co-ordinate ϕ (Chambers, 1953). The rest of the modes (with ϕ dependency) are combinations of TE and TM modes and are called "hybrid".

These fields extend further from the rod and their attenuation lessens with a decrease in the radius of the dielectric core (Balanis, 1988, p. 508). The attenuation decreases as less of the field occurs in the rod where some dielectric loss will always exist. Therefore minimum sized radius rods are usually used in dielectric waveguides (Balanis, 1988, pp. 508, 513) (this may not apply in filters using high Q dielectrics). The modes in the dielectric waveguide are cut off below a minimum value of electrical radius a/λ (Collin, 1991, p. 721) (Balanis, 1988, p. 507). The dominant mode, sometimes called the HEM_{11} mode (this designation will be described below) in theory has no cut-off frequency.

Rectangular dielectric waveguides have similar hybrid modes to the circular cross-section versions (including a dominant HEM_{11} mode) but have no TE and TM axially symmetric modes (Lioubtchenko et al., 2003) (Chambers, 1953).

Unlike metallic waveguides the field patterns of the modes in dielectric waveguide are sensitive to dielectric constant, frequency, and aspect ratio (if rectangular) or radius (if circular). This complicates the problem of finding a suitably descriptive classification scheme and as a consequence a number exist which have been created to suit the particular structure being investigated at the time. That is, an overall standard does not exist. For clarity, it is worthwhile to list some of the main schemes used in literature up to date:

1. The method used by Marcatili (1969) and Goell (1969) in which modes are designated as:

$$E_{pq}^{m}$$

The superscript m is the direction of polarisation x or y of the dominant electric field component. Subscripts p and q denote the number of maxima of the dominant electric field component in the x and y directions respectively. This scheme is generally used when describing the modes of rectangular cross-section dielectric waveguide.

2. The method proposed by Kobayashi et al. (1981) and used by Solbach & Wolff (1978) and Collin (1991) in which modes are designated as:

$$EH_{mn}, \quad HE_{mn}$$

This method is in agreement with that of Marcatili (1969) as to the meaning of the subscripts but has no superscript. The designation EH is used to indicate when the longitudinal field is mainly electric (TM) and HE when the longitudinal field is mainly magnetic (TE). This method is used with rectangular and circular cross-section dielectrics.

Referring to the work of Schweig & Bridges (1984) for a rectangular dielectric rod in free space :

EH_{11} corresponds to E_{11}^{y},

HE_{11} corresponds to E_{11}^{x},

EH_{21} corresponds to E_{21}^{x} and

HE_{21} corresponds to E_{21}^{y} etc.

A third subscript (p) is used with dielectric resonators and dielectric loaded cavity resonators (a dielectric rod in a metallic cavity) to denote the number of maxima in the longitudinal direction.

3. The method used by Kajfez & Guillon (1986), Balanis (1988) and others in literature to describe modes in circular cross-section dielectric waveguide and resonators. This scheme has been designated by IEEE (*IRE Standards on Antennas and Waveguides: Definition of Terms,* (1953)) as:

$$HEM_{mn}$$

Balanis (1988, p. 512) states that subscript m refers to the order of the Bessel functions used in the cylindrical dielectric rod hybrid mode field equations. Eigen-

value equations, which can be used to determine the wave-numbers and propagation coefficient of the circular dielectric waveguide, can only have eigenvalue solutions that give real radially directed wavenumbers outside the dielectric and thereby give decaying fields. If these wavenumbers were to become imaginary the structure would cease to be a waveguide and become an antenna. The subscript n refers to the propagation order of each mode for a particular m, that will allow the wavenumbers to remain real. Again from Balanis (1988, p. 512), a consequence of this is that odd values of n give EH modes and even n give HE modes. Thus:

$HEM_{m,2n-1}$ $(n = 1, 2, 3, ...)$ corresponds to $HE_{m,n}$ and

$HEM_{m,2n}$ $(n = 1, 2, 3, ...)$ corresponds to $EH_{m,n}$.

A third subscript p is used with dielectric resonators to denote the number of maxima in the longitudinal direction. This scheme does not appear to have been used for rectangular dielectrics.

4. A simpler scheme, applied only to circular cross-section dielectric loaded resonators, was proposed by Zaki & Chen (1986) and uses only two subscripts. It uses the designations:

$$HEH_{nm} \text{ and } HEE_{nm}$$

The first two letters denote a hybrid mode. The third letter denotes whether a transverse symmetry plane is a magnetic or electric wall. The subscript n indicates the order of the ϕ variation ($\cos n\phi$ or $\sin n\phi$) in the field equations of a particular mode. Subscript m classifies the resonant frequencies of modes in increasing order for a particular n.

In this dissertation the scheme used will be that of Marcatili. This is because the transverse field pattern plots, generated from the field solving method of this chapter, can easily be recognised and then allocated a mode designation from this scheme.

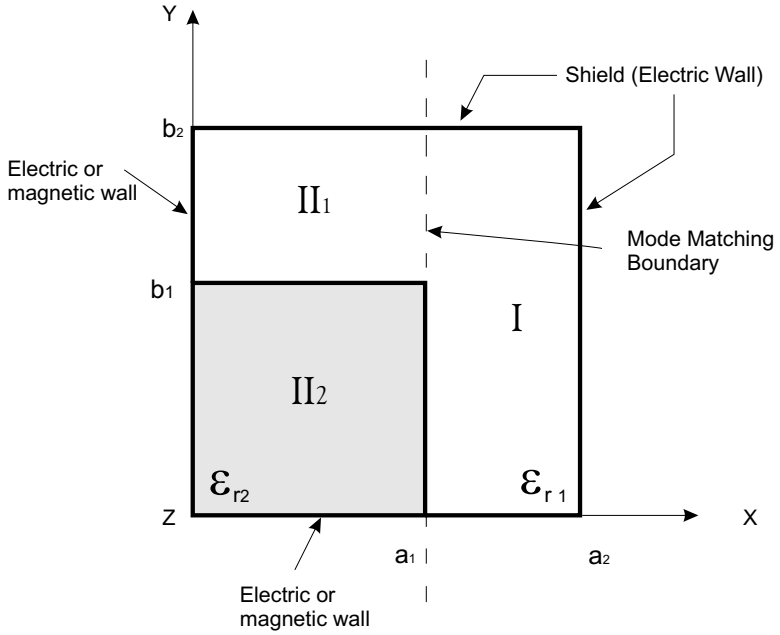

Figure 4.2: One quarter of the rectangular dielectric line with shield, showing mode-matching regions.

4.4 Analysis using the Mode Matching Method

An advantage of a mode matching method is that it has relatively good processing speed due to its semi-analytical nature. It allows visualization of the fields in the structure by solving for the unknown coefficients of the basis function equations. Another advantage is that it can be used with reasonably high values of permittivity (Strube & Arndt (1985) show results as high as $\varepsilon_r = 50$ for the shielded dielectric image line). The other numerical methods cited, with the exception of the finite difference method of Schweig & Bridges (1984), have only been applied to relatively low values ($\varepsilon_r \simeq 2.5$). Due to the symmetrical nature of the shielded dielectric waveguide only one quarter of the structure needs to be analysed. Figure 4.2 shows how the cross-section is divided into three regions. Regions I and II_1 surround the dielectric rod and are filled with a medium of permittivity ε_{r1}, which will be considered to be air ($\varepsilon_{r1} = 1$) in this chapter. Region II_2 is the dielectric rod with permittivity ε_{r2}. The outer shield will be considered as a perfect electric conductor (electric wall). The bottom and left side symmetry planes, coincident with the x and y axes, may be either electric or magnetic

walls. The selection of wall types will determine the types of symmetry that can exist in the structure.

In this chapter, as in Mittra et al. (1980) and Strube & Arndt (1985), a modification of the mode matching method of Solbach & Wolff (1978) will be used so that the effect of the proximity of the shield to the dielectric can be ascertained. However to provide calculation of all modes possible in this structure, additional basis functions[2] to cater for the full range of symmetries (see section 4.4.1), have had to be provided. This variation will be called the modified Solbach and Wolff method (MSW) through the rest of this chapter.

4.4.1 Basis Functions

The modes which can propagate in a shielded rectangular dielectric rod waveguide are all hybrid modes, ie they always have field variation along either the horizontal or vertical dielectric rod boundaries, and so have both electric and magnetic field components in the longitudinal direction (Chambers, 1953). In each of the regions in Figure 4.2, the field patterns for these modes can be built up from superpositions of appropriate basis functions, which are transverse magnetic or transverse electric with respect to the y direction. These will be designated TM^y (electric) and TE^y (magnetic) respectively, and indicated by subscripts e and h.

When using mode matching the basis functions used in each region must satisfy the boundary conditions except at the mode-matching boundary (Itoh, 1989, p. 592). TM^y and TE^y are used as they satisfy the boundary conditions on the upper dielectric to air boundary. Other formulations such as TM^x and TE^x do not (Harrington, 2001, p. 158).

The cross-section has two axes of symmetry, which means there are four possible symmetries. In this chapter these will be classified according to the behaviour of the H_z

[2]To reduce confusion with the term 'modes', the modes of rectangular waveguide, used to 'build up' the actual modes of the structure, will be called basis functions in this chapter.

field component, following Schweig & Bridges (1984). For example, superscript EO will indicate that H_z is an even function of x and an odd function of y.

It is most efficient to derive the basis function fields from vector potentials. From Balanis (1988), the magnetic vector potential for a TM^y wave propagating in a non-magnetic region in the z direction in a region with rectangular boundaries is of the form:

$$A_y(x,y,z) = [C_1\cos(\beta_x x) + D_1\sin(\beta_x x)][C_2\cos(\beta_y y) + D_2\sin(\beta_y y)]e^{-\gamma z} \tag{4.1}$$

The longitudinal field components can then be obtained from:

$$E_z(x,y,z) = -j\frac{1}{\omega\mu_o\epsilon}\frac{\partial^2 A_y}{\partial y \partial z} \tag{4.2}$$

$$H_z(x,y,z) = \frac{1}{\mu_o}\frac{\partial A_y}{\partial x} \tag{4.3}$$

From these expressions it can be seen that E_z and H_z will have opposite types of symmetry. The longitudinal electric field will be as follows:

$$E_z(x,y,z) = j\frac{\beta_y\gamma}{\omega\mu_o\epsilon}[C_1\cos(\beta_x x) + D_1\sin(\beta_x x)][D_2\cos(\beta_y y) - C_2\sin(\beta_y y)]e^{-\gamma z} \tag{4.4}$$

Using the boundary conditions imposed by the shield, appropriate equations for E_z can be selected in each region and for each symmetry. For the case of an even function of x axis and odd function of y (EO) these are as follows:

$$\begin{aligned}
E_{z_{me}}^{(I)EO} &= j\frac{A_{me}^{(I)}\beta_{yme}^{(I)}\gamma}{\omega\mu_o\epsilon_o}\sin(\beta_{x_{me}}^{(I)}(a_2-x))\cos(\beta_{y_{me}}^{(I)}y)e^{-\gamma z} \\
E_{z_{ne}}^{(II_1)EO} &= j\frac{B_{ne}^{(II_1)}\beta_{y_{ne}}^{(II_1)}\gamma}{\omega\mu_o\epsilon_o}\sin(\beta_{x_{ne}}^{(II_1)}x)\sin(\beta_{y_{ne}}^{(II_1)}(b_2-y))e^{-\gamma z} \\
E_{z_{ne}}^{(II_2)EO} &= j\frac{B_{ne}^{(II_2)}\beta_{y_{ne}}^{(II_2)}\gamma}{\omega\mu_o\epsilon_o\epsilon_{r2}}\sin(\beta_{x_{ne}}^{(II_2)}x)\cos(\beta_{y_{ne}}^{(II_2)}y)e^{-\gamma z}
\end{aligned} \tag{4.5}$$

Where

$$\begin{aligned}
\beta^{I}_{y_{me}} &= \frac{m\pi}{2b_2} \quad \text{where} \quad m = 1, 3, 5... \\
\beta^{(I)2}_{x_{me}} &= \beta^2_o - \beta^{(I)2}_{y_{me}} + \gamma^2 \\
\beta^{(II_1)2}_{y_{ne}} &= \beta^2_o - \beta^{(II_1)2}_{x_{ne}} + \gamma^2 \\
\beta^{(II_2)2}_{y_{ne}} &= \beta^2_d - \beta^{(II_2)2}_{x_{ne}} + \gamma^2 \\
\beta^2_o &= \omega^2 \mu_o \epsilon_o \\
\beta^2_d &= \omega^2 \mu_o \epsilon_o \epsilon_{r2}
\end{aligned} \tag{4.6}$$

and n is the mode number in region II.

From equations (4.2) and (4.5) the resultant magnetic vector potential equations for the dielectric waveguide are then:

$$\begin{aligned}
A^{(I)EO}_{y_{me}} &= A^{(I)}_{me} \sin(\beta^{(I)}_{x_{me}}(a_2 - x)) \sin(\beta^{(I)}_{y_{me}} y) e^{-\gamma z} \\
A^{(II_1)EO}_{y_{ne}} &= B^{(II_1)}_{ne} \sin(\beta^{(II_1)}_{x_{ne}} x) \cos(\beta^{(II_1)}_{y_{ne}}(b_2 - y)) e^{-\gamma z} \\
A^{(II_2)EO}_{y_{ne}} &= B^{(II_2)}_{ne} \sin(\beta^{(II_2)}_{x_{ne}} x) \sin(\beta^{(II_2)}_{y_{ne}} y) e^{-\gamma z}
\end{aligned} \tag{4.7}$$

Then using equation (4.3) the equations for H_z are:

$$\begin{aligned}
H^{(I)EO}_{z_{me}} &= -\frac{A^{(I)}_{me}\beta^{(I)}_{x_{me}}}{\mu_o} \cos(\beta^{(I)}_{x_{me}}(a_2 - x)) \sin(\beta^{(I)}_{y_{me}} y) e^{-\gamma z} \\
H^{(II_1)EO}_{z_{ne}} &= \frac{B^{(II_1)}_{ne}\beta^{(II_1)}_{x_{ne}}}{\mu_o} \cos(\beta^{(II_1)}_{x_{ne}} x) \cos(\beta^{(II_1)}_{y_{ne}}(b_2 - y)) e^{-\gamma z} \\
H^{(II_2)EO}_{z_{ne}} &= \frac{B^{(II_2)}_{ne}\beta^{(II_2)}_{x_{ne}}}{\mu_o} \cos(\beta^{(II_2)}_{x_{ne}} x) \sin(\beta^{(II_2)}_{y_{ne}} y) e^{-\gamma z}
\end{aligned} \tag{4.8}$$

From equations (4.7) the other components of the TM^y basis functions for each region can be derived using the partial differential equations from Balanis (1988).

Similarly the electric vector potential equation for a TE^y mode propagating in the z direction is of the form:

$$F_y(x, y, z) = [C_1 \cos(\beta_x x) + D_1 \sin(\beta_x x)][C_2 \cos(\beta_y y) + D_2 \sin(\beta_y y)] e^{-\gamma z} \tag{4.9}$$

The longitudinal field components can then be found from:

$$E_z(x,y,z) = -\frac{1}{\epsilon}\frac{\partial F_y}{\partial x} \tag{4.10}$$

$$H_z(x,y,z) = -j\frac{1}{\omega\mu_o\epsilon}\frac{\partial^2 F_y}{\partial y \partial z} \tag{4.11}$$

E_z will then be:

$$E_z(x,y,z) = -\frac{1}{\epsilon}[D_1\cos(\beta_x x) - C_1\sin(\beta_x x)][C_2\cos(\beta_y y) + D_2\sin(\beta_y y)]e^{-\gamma z} \tag{4.12}$$

Using the boundary conditions and symmetry as for the TM^y example the E_z equations in each region can be selected as:

$$\begin{aligned}
E_{z_{mh}}^{(I)EO} &= -\frac{A_{mh}^{(I)}\beta_{x_{mh}}^{(I)}}{\epsilon_o}\sin(\beta_{x_{mh}}^{(I)}(a_2-x))\cos(\beta_{y_{mh}}^{(I)}y)e^{-\gamma z} \\
E_{z_{nh}}^{(II_1)EO} &= \frac{B_{nh}\beta_{x_{nh}}^{(II_1)}}{\epsilon_o}\sin(\beta_{x_{nh}}^{(II_1)}x)\sin(\beta_{y_{nh}}^{(II_1)}(b_2-y))e^{-\gamma z} \\
E_{z_{nh}}^{(II_2)EO} &= \frac{B_{nh}^{(II_2)}\beta_{x_{nh}}^{(II_2)}}{\epsilon_o\epsilon_{r2}}\sin(\beta_{x_{nh}}^{(II_2)}x)\cos(\beta_{y_{nh}}^{(II_2)}y)e^{-\gamma z}
\end{aligned} \tag{4.13}$$

where h is TE^y.

Then a set of electric vector potential equations for the structure will be:

$$\begin{aligned}
F_{y_{mh}}^{(I)EO} &= A_{mh}^{(I)}\cos(\beta_{x_{mh}}^{(I)}(a_2-x))\cos(\beta_{y_{mh}}^{(I)}y)e^{-\gamma z} \\
F_{y_{nh}}^{(II_1)EO} &= B_{nh}\cos(\beta_{x_{nh}}^{(II_1)}x)\sin(\beta_{y_{nh}}^{(II_1)}(b_2-y))e^{-\gamma z} \\
F_{y_{nh}}^{(II_2)EO} &= B_{nh}^{(II_2)}\cos(\beta_{x_{nh}}^{(II_2)}x)\cos(\beta_{y_{nh}}^{(II_2)}y)e^{-\gamma z}
\end{aligned} \tag{4.14}$$

Then using equation (4.11) the equations for H_z are:

$$\begin{aligned}
H_{z_{mh}}^{(I)EO} &= -j\frac{A_{mh}^{(I)}\beta_{y_{mh}}^{(I)}\gamma}{\omega\mu_o\epsilon_o}\cos(\beta_{x_{mh}}^{(I)}(a_2-x))\sin(\beta_{y_{mh}}^{(I)}y)e^{-\gamma z} \\
H_{z_{nh}}^{(II_1)EO} &= -j\frac{B_{nh}\beta_{y_{nh}}^{(II_1)}\gamma}{\omega\mu_o\epsilon_o}\cos(\beta_{x_{nh}}^{(II_1)}x)\cos(\beta_{y_{nh}}^{(II_1)}(b_2-y))e^{-\gamma z} \\
H_{z_{nh}}^{(II_2)EO} &= -j\frac{B_{nh}^{(II_2)}\beta_{y_{nh}}^{(II_2)}\gamma}{\mu_o\epsilon_o\epsilon_{r2}}\cos(\beta_{x_{nh}}^{(II_2)}x)\sin(\beta_{y_{nh}}^{(II_2)}y)e^{-\gamma z}
\end{aligned} \tag{4.15}$$

The other components of the TE^y basis functions can again be found from the partial differential equations from Balanis (1988).

A summary of the vector potential and longitudinal basis function equations for all symmetries is shown in Appendix B.1.

Continuity of the tangential field components at the boundary $y = b_1,\ 0 \leq x \leq a_1$ between region II_1 and region II_2 must also be taken into account so that wavenumbers $\beta_{y_n}^{(II_2)}$ and $\beta_{y_n}^{(II_1)}$ can be found. At this boundary wavenumbers $\beta_{x_n}^{(II_1)} = \beta_{x_n}^{(II_2)}$ to allow for continuity of phase. Then for even x, odd y symmetry and TM^y modes:

$$E_{z_{ne}}^{(II_1)EO} = E_{z_{ne}}^{(II_2)EO} \tag{4.16}$$

and from this:

$$K_{ne} = \frac{B_{ne}^{(II_1)}}{B_{ne}^{(II_2)}} = \frac{\beta_{y_{ne}}^{(II_2)} \cos(\beta_{y_{ne}}^{(II_2)} b_1)}{\beta_{y_{ne}}^{(II_1)} \epsilon_{r2} \sin(\beta_{y_{ne}}^{(II_1)} (b_2 - b_1))} \tag{4.17}$$

then also:

$$H_{z_{ne}}^{(II_1)EO} = H_{z_{ne}}^{(II_2)EO} \tag{4.18}$$

substituting equation (4.17) into (4.18) gives the transcendental equation:

$$\frac{1}{\beta_{y_{ne}}^{(II_1)}} \cot(\beta_{y_{ne}}^{(II_1)} (b_2 - b_1)) = \frac{\epsilon_{r2}}{\beta_{y_{ne}}^{(II_2)}} \tan(\beta_{y_{ne}}^{(II_2)} b_1) \tag{4.19}$$

The wavenumbers can then be obtained from (4.19) by substitution of the relation:

$$\beta_{y_{ne}}^{(II_2)2} = \beta_{y_{ne}}^{(II_1)2} + \beta_o^2 (\epsilon_r - 1) \tag{4.20}$$

which is derived using $\beta_{x_{ne}}^{(II_1)} = \beta_{x_{ne}}^{(II_2)}$ and the region II equations of (4.6).

Similarly for the TE^y modes:

$$K_{nh} = \frac{B_{nh}^{(II_1)}}{B_{nh}^{(II_2)}} = \frac{\cos(\beta_{y_{nh}}^{(II_2)} b_1)}{\epsilon_{r2} \sin(\beta_{y_{nh}}^{(II_1)} (b_2 - b_1))} \tag{4.21}$$

and the transcendental equation for the wavenumbers becomes:

$$\beta_{y_{nh}}^{(II_1)} \cot(\beta_{y_{nh}}^{(II_1)} (b_2 - b_1)) = \beta_{y_{nh}}^{(II_2)} \tan(\beta_{y_{nh}}^{(II_2)} b_1) \tag{4.22}$$

The equations for the other symmetries of the TM^y and TE^y basis functions can similarly be derived.

A summary of the equations derived from the continuity of the longitudinal fields at the boundary $y = b_1,\ 0 \leq x \leq a_1$, for all symmetries, is shown in Appendix B.2.

4.4.2 Mode Matching at the Boundary Between Regions

The transverse fields $\mathbf{E}_T$ and $\mathbf{H}_T$ must be continuous at the mode matching boundary between regions I and II ($x = a_1,\ 0 \leq y \leq b_2$). In the case of the electric field this leads to the equations:

$$\sum_{p=1}^{\infty} A_{ph}^{(I)} E_{z_{ph}}^{(I)} + \sum_{p=1}^{\infty} A_{pe}^{(I)} E_{z_{pe}}^{(I)} = \sum_{n=1}^{\infty} B_{nh}^{(II_2)} (K_{nh} E_{z_{nh}}^{(II_1)} + E_{z_{nh}}^{(II_2)}) + \sum_{n=1}^{\infty} B_{ne}^{(II_2)} (K_{ne} E_{z_{ne}}^{(II_1)} + E_{z_{ne}}^{(II_2)}) \tag{4.23}$$

and

$$\sum_{p=1}^{\infty} A_{pe}^{(I)} E_{y_{pe}}^{(I)} = \sum_{n=1}^{\infty} B_{ne}^{(II_2)} (K_{ne} E_{z_{ne}}^{(II_1)} + E_{z_{ne}}^{(II_2)}) \tag{4.24}$$

For continuity of the magnetic fields:

$$\sum_{p=1}^{\infty} A_{ph}^{(I)} H_{z_{ph}}^{(I)} + \sum_{p=1}^{\infty} A_{pe}^{(I)} H_{z_{pe}}^{(I)} = \sum_{n=1}^{\infty} B_{nh}^{(II_2)} (K_{ne} H_{z_{nh}}^{(II_1)} + H_{z_{nh}}^{(II_2)}) + \sum_{n=1}^{\infty} B_{ne}^{(II_2)} (K_{ne} H_{z_{nh}}^{(II_1)} + H_{z_{ne}}^{(II_2)}) \tag{4.25}$$

and

$$\sum_{p=1}^{\infty} A_{ph}^{(I)} H_{y_{ph}}^{(I)} = \sum_{n=1}^{\infty} B_{nh}^{(II_2)} (K_{nh} H_{z_{nh}}^{(II_1)} + H_{z_{nh}}^{(II_2)}) \tag{4.26}$$

where K is the RHS of equations (4.17) and (4.21) for TM^{EO} and TE^{EO} basis functions respectively and was introduced to reduce the number of unknown coefficients. The above equations constitute a doubly infinite set of linear equations for the modal coefficients A_p and B_n. To simplify these equations, and to expand their number to equal the number of unknowns the electric and magnetic fields in region I were used as testing functions. Only the y dependent factors are required, and these have been designated $e_q^{(I)}(y)$ and $h_q^{(I)}(y)$ respectively. The following orthogonality relations are

required:

$$\int_0^{b_2} \mathbf{E}_{Tm}^{(I)} h_q^{(I)}(y) d_y = 0 \tag{4.27}$$

$$\int_0^{b_2} \mathbf{H}_{Tm}^{(I)} e_q^{(I)}(y) d_y = 0 \tag{4.28}$$

$$\text{for } m \neq q$$

where m and q are the indices used to find wavenumbers $\beta_{y_m}^{(I)}$ or $\beta_{y_q}^{(I)}$ (as in (4.6)) for each mode number p in region I. That is, for the electric fields, equation (4.23) is multiplied by a $h_q^{(I)}(y)$, TE^y testing function and equation (4.24) is multiplied by a $h_q^{(I)}(y)$, TM^y testing function. For the magnetic fields, equation (4.25) is multiplied by a $e_q^{(I)}(y)$, TE^y testing function and equation (4.26) is multiplied by a $e_q^{(I)}(y)$, TM^y testing function. The resultant equations are then integrated over the interval $0 \leq y \leq b_2$ at $x = a_1$ continuing the procedure outlined by Mittra et al. (1980). The integrals derived from equations 4.27 and 4.28 for all symmetries are summarised in Appendix B.3.

The infinite set of equations so formed is reduced by truncating the number of basis functions used, to a value that can be practically computed and will give a desired degree of convergence to the extrapolated solution (see sections 4.6.1 and 4.10.2). The maximum values of the mode indices p and n are P and N respectively. An equal number of basis functions were used ($P = N$) in both regions I and II to alleviate any problems with relative convergence (Mittra, 1963)(Leroy, 1983). In matrix form the equations using the electric field and odd y symmetry are:

$$\begin{bmatrix} \begin{bmatrix} a_{11} & \cdots & 0 \\ \vdots & \ddots (TE_{E_z}^{(I)} TE_{h_y(y)}^{(I)}) & \vdots \\ 0 & \cdots & a_{PP} \end{bmatrix} & \begin{bmatrix} a_{11} & \cdots & 0 \\ \vdots & \ddots (TM_{E_z}^{(I)} TE_{h_y(y)}^{(I)}) & \vdots \\ 0 & \cdots & a_{PP} \end{bmatrix} \\ \begin{bmatrix} 0 & \cdots & 0 \\ \vdots & \ddots (TE_{E_y}^{(I)} TM_{h_z(y)}^{(I)}) = 0 & \vdots \\ 0 & \cdots & 0 \end{bmatrix} & \begin{bmatrix} a_{11} & \cdots & 0 \\ \vdots & \ddots (TM_{E_y}^{(I)} TM_{h_z(y)}^{(I)}) & \vdots \\ 0 & \cdots & a_{PP} \end{bmatrix} \end{bmatrix} \begin{bmatrix} A_1^{TE} \\ \vdots \\ A_P^{TE} \\ A_1^{TM} \\ \vdots \\ A_P^{TM} \end{bmatrix} =$$

$$\begin{bmatrix} \begin{bmatrix} b_{11} & \cdots & b_{1N} \\ \vdots & \ddots (TE^{(II)}_{E_z} TE^{(I)}_{h_y(y)}) & \vdots \\ b_{N1} & \cdots & b_{NN} \end{bmatrix} & \begin{bmatrix} b_{11} & \cdots & b_{1N} \\ \vdots & \ddots (TM^{(II)}_{E_z} TE^{(I)}_{h_y(y)}) & \vdots \\ b_{N1} & \cdots & b_{NN} \end{bmatrix} \\ \begin{bmatrix} 0 & \cdots & 0 \\ \vdots & \ddots (TE^{(II)}_{E_y} TM^{(I)}_{h_z(y)}) = 0 & \vdots \\ 0 & \cdots & 0 \end{bmatrix} & \begin{bmatrix} b_{11} & \cdots & a_{1N} \\ \vdots & \ddots (TM^{(II)}_{E_y} TM^{(I)}_{h_z(y)}) & \vdots \\ a_{N1} & \cdots & b_{NN} \end{bmatrix} \end{bmatrix} \begin{bmatrix} B_1^{TE} \\ \vdots \\ B_N^{TE} \\ B_1^{TM} \\ \vdots \\ B_N^{TM} \end{bmatrix} \tag{4.29}$$

The sub matrices of the LHS of equation (4.29) are P x P diagonal matrices the elements of which are the result of equation (4.27). The elements of the N x N sub matrices of the RHS of equation (4.29) are coupling integrals of the form:

$$\int_0^{b_2} \mathbf{E}^{(II)}_{Tn} h^{(I)}_q(y) d_y \tag{4.30}$$

The zero sub-matrices are the result of the E_y component which is zero for TE^y. This is also indicated by equation (4.24). In abbreviated form the matrix equations can be written as:

$$[\mathbf{W}][\mathbf{A}] = [\mathbf{X}][\mathbf{B}] \tag{4.31}$$

The magnetic field equations are similar and can be written as:

$$\begin{bmatrix} \begin{bmatrix} a_{11} & \cdots & 0 \\ \vdots & \ddots (TE^{(I)}_{H_y} TE^{(I)}_{e_z(y)}) & \vdots \\ 0 & \cdots & a_{PP} \end{bmatrix} & \begin{bmatrix} 0 & \cdots & 0 \\ \vdots & \ddots (TM^{(I)}_{H_y} TE^{(I)}_{e_z(y)}) = 0 & \vdots \\ 0 & \cdots & 0 \end{bmatrix} \\ \begin{bmatrix} a_{11} & \cdots & 0 \\ \vdots & \ddots (TE^{(I)}_{H_z} TM^{(I)}_{e_y(y)}) & \vdots \\ 0 & \cdots & a_{PP} \end{bmatrix} & \begin{bmatrix} a_{11} & \cdots & 0 \\ \vdots & \ddots (TM^{(I)}_{H_z} TM^{(I)}_{e_y(y)}) & \vdots \\ 0 & \cdots & a_{PP} \end{bmatrix} \end{bmatrix} \begin{bmatrix} A_1^{TE} \\ \vdots \\ A_P^{TE} \\ A_1^{TM} \\ \vdots \\ A_P^{TM} \end{bmatrix} =$$

$$\begin{bmatrix} \begin{bmatrix} b_{11} & \cdots & b_{1N} \\ \vdots & \ddots (TE^{(II)}_{H_y} TE^{(I)}_{e_z(y)}) & \vdots \\ b_{N1} & \cdots & b_{NN} \end{bmatrix} & \begin{bmatrix} 0 & \cdots & 0 \\ \vdots & \ddots (TM^{(II)}_{H_y} TE^{(I)}_{e_z(y)}) = 0 & \vdots \\ 0 & \cdots & 0 \end{bmatrix} \\ \begin{bmatrix} b_{11} & \cdots & b_{1N} \\ \vdots & \ddots (TE^{(II)}_{H_z} TM^{(I)}_{e_y(y)}) & \vdots \\ b_{N1} & \cdots & b_{NN} \end{bmatrix} & \begin{bmatrix} b_{11} & \cdots & a_{1N} \\ \vdots & \ddots (TM^{(II)}_{H_z} TM^{(I)}_{e_y(y)}) & \vdots \\ a_{N1} & \cdots & b_{NN} \end{bmatrix} \end{bmatrix} \begin{bmatrix} B_1^{TE} \\ \vdots \\ B_N^{TE} \\ B_1^{TM} \\ \vdots \\ B_N^{TM} \end{bmatrix} \tag{4.32}$$

The sub matrices of the LHS of equation (4.32) are P x P diagonal matrices the elements of which are the result of equation (4.28). The elements of the N x N sub

matrices of the RHS of equation (4.32) are coupling integrals of the form:

$$\int_0^{b_2} \mathbf{H}_{Tn}^{(II)} e_q^{(I)}(y) d_y \tag{4.33}$$

The zero sub-matrices are the result of the H_y component which is zero for TM^y. This is also indicated by equation (4.26). In abbreviated form the magnetic field matrix equations can be written as:

$$[\mathbf{Y}][\mathbf{A}] = [\mathbf{Z}][\mathbf{B}] \tag{4.34}$$

For this odd y case, for both electric and magnetic field equations, the subscripts m and q are odd integers only and are equivalent in number to the number of basis functions used N. For the even y case there will be a total of N even integers (including zero).

A summary of coupling integrals for all symmetries derived from equations (4.30) and (4.33) is shown in Appendix B.4.

4.4.3 Propagation Coefficient and Unknown Mode Coefficients of the Structure

A homogeneous system of equations may be formed from (4.31) and (4.34)

$$\begin{bmatrix} \mathbf{W} & -\mathbf{X} \\ \mathbf{Y} & -\mathbf{Z} \end{bmatrix} \begin{bmatrix} \mathbf{A} \\ \mathbf{B} \end{bmatrix} = 0 \tag{4.35}$$

The eigenvalues of equation (4.35) are the propagation coefficients of the modes of the structure. These can be found by substituting a range of propagation coefficient values into the equation and finding those values for which the determinant is zero.

To determine that the propagation coefficients found are physically sensible, and also to find the type of mode each represents, it is essential to calculate the unknown coefficients and plot the field patterns. Also there may be a requirement to calculate the loss in the dielectric and shield walls. In high power applications, it may be desirable to determine the peak electric field strength so as to check if air or dielectric breakdown is likely.

A selected coefficient is then chosen as unity (or some appropriate factor), so that equation (4.35) can then be written as:

$$\begin{bmatrix} \mathbf{A} \\ \mathbf{B}_r \end{bmatrix} = \begin{bmatrix} \mathbf{W} & -\mathbf{X}_r \\ \mathbf{Y} & -\mathbf{Z}_r \end{bmatrix}^{-1} \begin{bmatrix} (electric) \\ b_{11}^{TMTE} \\ \vdots \\ b_{N1}^{TMTM} \\ (magnetic) \\ b_{11}^{TMTE} \\ \vdots \\ b_{N1}^{TMTM} \end{bmatrix} \tag{4.36}$$

For example if the coefficient chosen is the first TM mode in region II (B_1^{TM}) the associated matrix element values will be b_{11}^{TMTE} (electric) to b_{N1}^{TMTM} (magnetic) as shown. Consequently the $\mathbf{B}$ coefficients are reduced by one to $\mathbf{B}_r$ and the $\mathbf{X}$ and $\mathbf{Z}$ matrices are reduced by a column to $\mathbf{X}_r$ and $\mathbf{Z}_r$. The linear system of equations can then be solved by matrix inversion or QR decomposition (see section 4.5.2) using the Matlab operator '\'.

Once the coefficients are found they can then be substituted into the field equations, so that the field components can be determined from the sum of the basis functions at a number of spatial grid points, and the resultant field in the structure can be plotted as a superposition of all the components.

4.5 Programing Methods

4.5.1 Propagation Coefficient Calculation

The programing steps to find the propagation coefficients in a shielded rectangular dielectric rod waveguide are shown in the flow chart of Figure 4.3 and the details are as follows:

1. Allocate the dimensions of the structure, number of basis functions for sufficient convergence, discrete steps of frequency and propagation coefficient values over the ranges required, permittivity of the dielectric rod and constants (μ_0, ε_0 etc).

2. Provide a 'for' loop of the frequency range.

3. Calculate using equations (4.6) the wavenumbers of the air β_0 and dielectric rod β_d region materials.

4. Find the wavenumbers $\beta_{y_n}^{(II_2)}$, $\beta_{y_n}^{(II_1)}$ for the TE and TM basis functions and desired symmetry from the transcendental equations of Appendix B.2 and equation (4.20). The roots of the transcendental equations were found by the use of the Matlab function 'Fzero'. A wide enough range of wavenumber values has to be provided, in this function, so that a sufficient number of roots are found to cover the number of basis functions used. Also caution has to be exercised when assigning the step size between estimates used in the root finding function otherwise wavenumbers may be missed. See section 4.10.1 for more details. The equations were tested for real and imaginary wavenumber roots and the results were stored in a vector array.

5. An array of the coupling integrals of region II, as shown in Appendix B.4, was calculated for all the combinations of the basis functions and test functions used. The solutions to these integrals can be found analytically.

6. Calculate the constants K. These can be seen in equations (4.23), (4.24), (4.25) and (4.26) and are used to reduce the number of unknown coefficients in the region II equations.

7. Provide a 'for' loop of the anticipated propagation coefficient range:

   (a) For propagating modes and backward waves the values will lie between 0 and $j\beta_d$.

   (b) There will be an infinite number of evanescent modes, so a range from 0 to a practical value which will give a sufficient number of roots to cover requirements is needed.

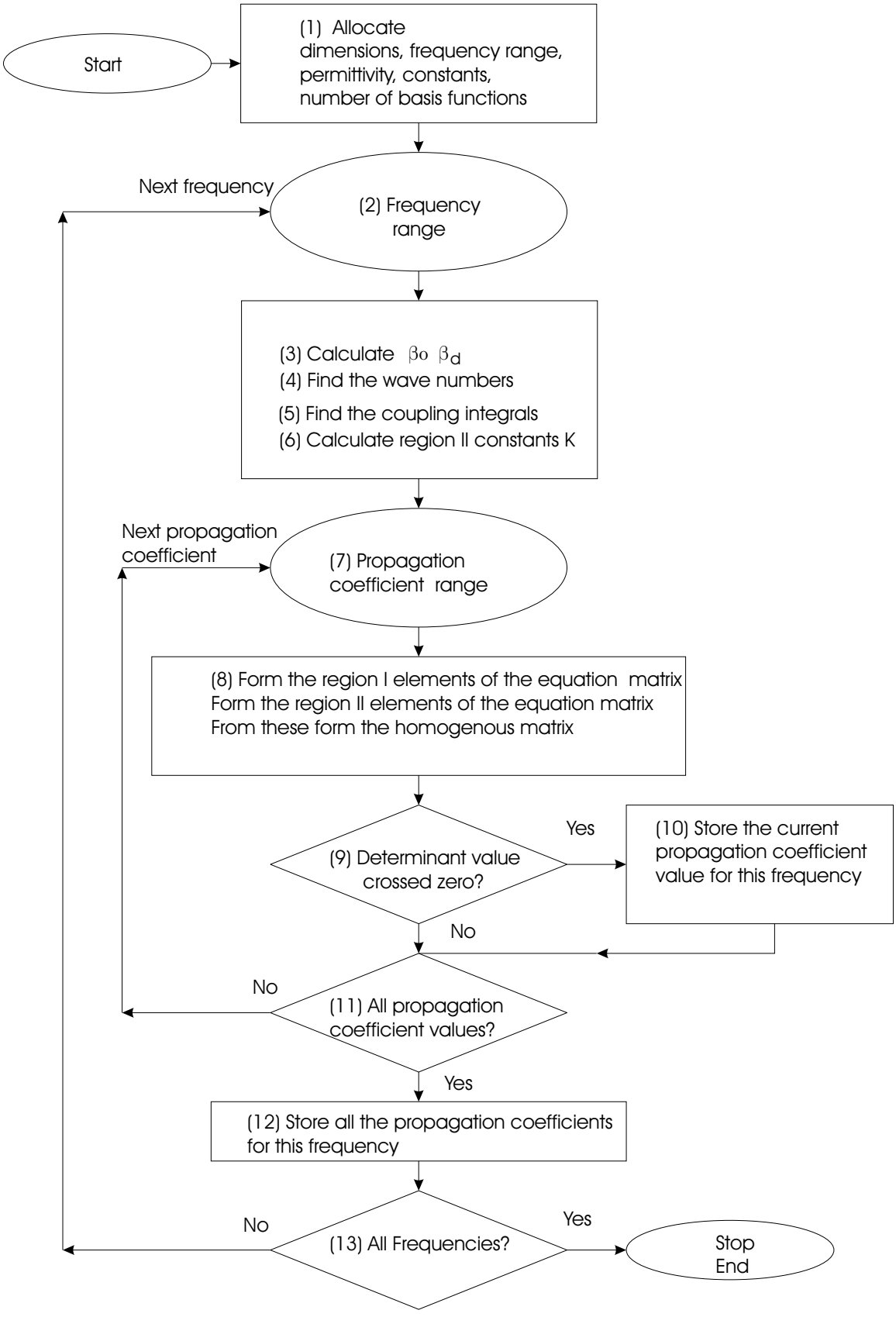

Figure 4.3: Flow chart of the program to find the propagation coefficient of the shielded rectangular dielectric rod waveguide

(c) The propagation coefficient range of complex modes and the frequency range over which they occur is difficult to estimate. They fill in areas of the frequency range where a conversion takes place between propagating and evanescent modes (Oliner et al., 1981). The characteristics of complex modes can be seen in a paper by Strube & Arndt (1985) and a mathematical method of predicting them is described by Marozowski & Mazur (1990).

8. Form the region I elements of the LHS sub-matrices of equations (4.29) and (4.32). These are diagonal matrices derived from the orthogonality relations depicted by equations (4.27) and (4.28). Nested 'for' loops of the region I basis function and region I testing function indices are used in their formation. The integrals and their solutions can be found in Appendix B.3

   Form the region II elements of the RHS sub matrices of the equations (4.29) and (4.32). These matrices are formed from integral expressions (4.30) and (4.33). The integrals solutions were already calculated in step 5 and are sourced from that stored array. Nested 'for' loops of the region II basis function and region I testing function indices are used in the formation of these sub matrices.

   Matrix equations (4.29) and (4.32) are then formed into the square matrix of the LHS of homogeneous equation (4.35).

9. The determinant of the square matrix for the current propagation coefficient and frequency is then determined using the Matlab function 'det'.

10. A trend in the determinant value is ascertained by comparing the current value with the previous one. If this indicates that the determinant value would have passed through zero an eigenvalue is specified and the current propagation coefficient is stored as a propagation coefficient value for the structure. Therefore part of the procedure accuracy is dependent on the size of the steps used over the propagation coefficient range.

11. The next propagation coefficient value is used until all in the required range have been applied.

    A procedure of "zeroing in", not shown on the flow chart, was used in the program

to reduce the time needed to find suitably accurate propagation coefficients that can exist in the large numerical range. Essentially steps 7 to 11 were repeated, firstly with coarse steps to find rough values and the total number of them in the range. Secondly, the area between each rough value found, and each preceding coarse step of those values, was searched with much finer steps. The same procedure could then be repeated again until the required degree of convergence to the extrapolated solution (see sections 4.6.1 and 4.10.2) was obtained for each propagation coefficient found. The initial coarse step size has to be chosen with caution so as not to step over two values that are close together or, step over a value which is close to where a "real/imaginary change-over" ReImC/O point occurs (more detail on this below). In either case an eigenvalue may be missed by the computer code written to detect a zero crossing.

When the data used in Figures 4.14 and 4.21 were produced the initial coarse step size was 2 and then a succession of two finer searches of a tenth and then a hundredth of that size were implemented at each rough propagation coefficient value found.

12. All the propagation coefficient values (eigenvalues) found in step 9 are then stored for the current frequency.

13. The next frequency value is used until all in the required range have been applied.

Plots of typical determinant values verses propagation coefficient for EO symmetry and lossless dielectric are shown in Figures 4.4, 4.5 and 4.6. When searching for the propagation coefficients of propagating modes and backward waves, imaginary testing propagation coefficients are used. For evanescent modes the testing propagation coefficients are real. In both cases, for a lossless dielectric, the resultant determinant values are either purely real or purely imaginary except for the occasional "real/imaginary change-over" ReImC/O point . See Figures 4.4 and 4.5.

As indicated these ReImC/O points occur in the eigenvalue tests for both propagating and evanescent mode propagation coefficients.

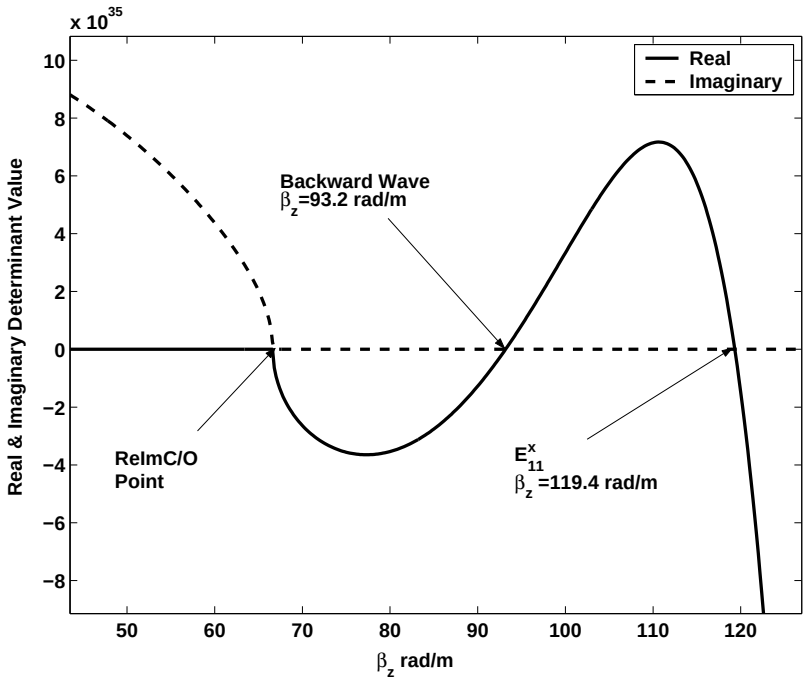

Figure 4.4: Determinant value verses propagation coefficient for the E_{11}^x propagating mode and backward wave at a frequency of 2.81GHz. $a_1 = b_1$=6mm, $a_2 = b_2$=12mm, $\varepsilon_{r2} = 37.13$, EO symmetry

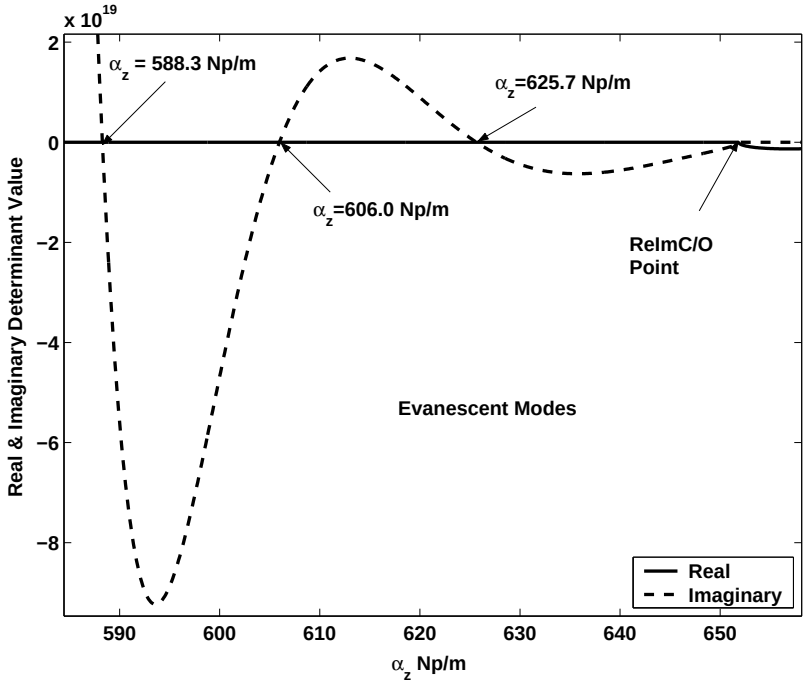

Figure 4.5: Determinant value verses propagation coefficient of some of the evanescent modes at 2.81GHz. $a_1 = b_1$=6mm, $a_2 = b_2$=12mm, $\varepsilon_{r2} = 37.13$, EO symmetry

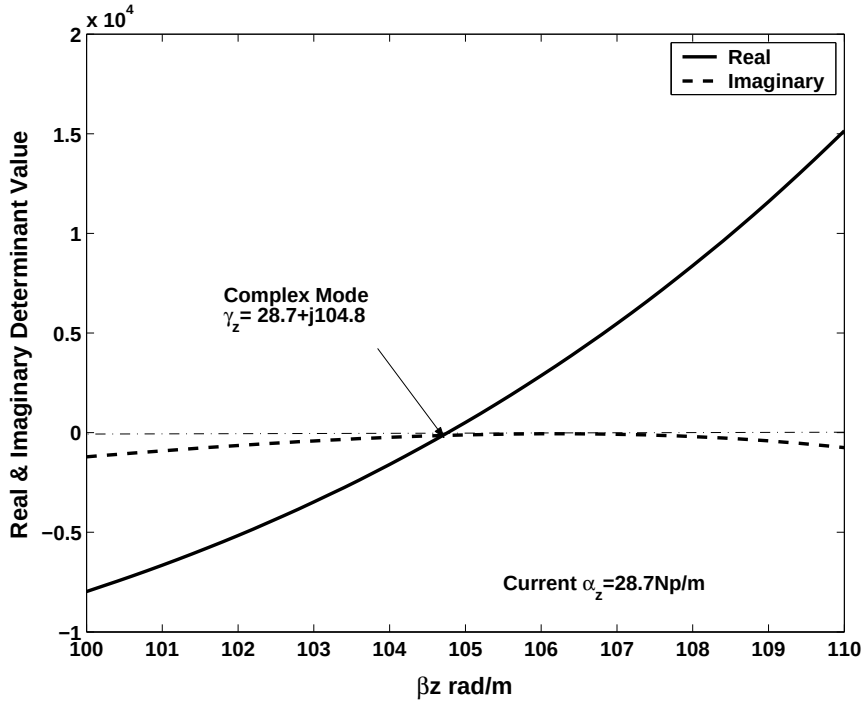

Figure 4.6: Determinant value verses propagation coefficient of a complex mode at 2.78GHz. $a_1 = b_1$=6mm, $a_2 = b_2$=12mm, $\varepsilon_{r2} = 37.13$, EO symmetry

They do not coincide with any mode seen in measurement or have a sensible place on the calculated mode chart (section 4.6.5) and so appear to have no physical meaning.

When searching for complex modes, complex testing propagation coefficients have to be used and the determinant values obtained are also complex. For complex modes the eigenvalues occur at points where both the real and imaginary determinant components cross zero as shown in Figure 4.6. This complicates the programing as two propagation coefficient 'for' loops have to be provided. One for a range of α_z values and another for a range of $j\beta_z$ values. Extra programing then determines when real and imaginary determinant values ,which are very close to being numerically equal (real/imaginary intersection points), pass through zero. The program then records the current $\alpha_z + j\beta_z$ propagation coefficient value. An initial starting range of $j\beta_z$ values for the program can be determined from the cutoff propagation coefficient found previously, for the propagating mode that stems from the complex mode to be calculated. For example, see the evolution of the complex mode to the E_{11}^x mode in Figure 4.14

To calculate the propagation coefficient of a propagating mode when the dielectric has some loss (complex permittivity) nearly the same programing procedure can be used as in the lossless case. The only significant difference is that the region II wavenumbers, $\beta_{y_n}^{(II_2)}$ and $\beta_{y_n}^{(II_1)}$, are now complex, and consequently the transcendental equations cannot be solved by the Matlab function 'Fzero'. Newtons method can be used to find complex roots but it requires a very good estimate of the root and this can be difficult to obtain. It was found that the most convenient method to use was Muller's method (Conte & DeBoor, 1980). Although more complicated and slower than 'Fzero' it will also find real and imaginary as well as complex roots and does not need a complex estimate of the root, ie complex roots can be found with only an estimate of the real or imaginary part of the complex root. However the rate of convergence of Muller's method is fairly dependent on the initial estimate chosen.

A method using this programming variation for calculating the attenuation due to dielectric loss for the rectangular shielded dielectric rod waveguide will be described in the next chapter in section 5.4.

4.5.2 Calculation of the Unknown Coefficients and Field Plotting of a Propagating Mode

The programing steps to find the unknown coefficients of the basis functions for a shielded rectangular dielectric rod waveguide are shown in the flow chart of Figure 4.7 and the details are as follows:

1. Download the parameters, including wavenumbers, and dimensions of the structure that was used in the previous program to calculate the propagation coefficients at a particular frequency. Downloading rather than regenerating the wavenumbers is preferred as the process of obtaining them accurately is time consuming.

   Select and input a propagation coefficient of interest.

   The next three steps are the same as steps 3, 5 and 6 of the program of section

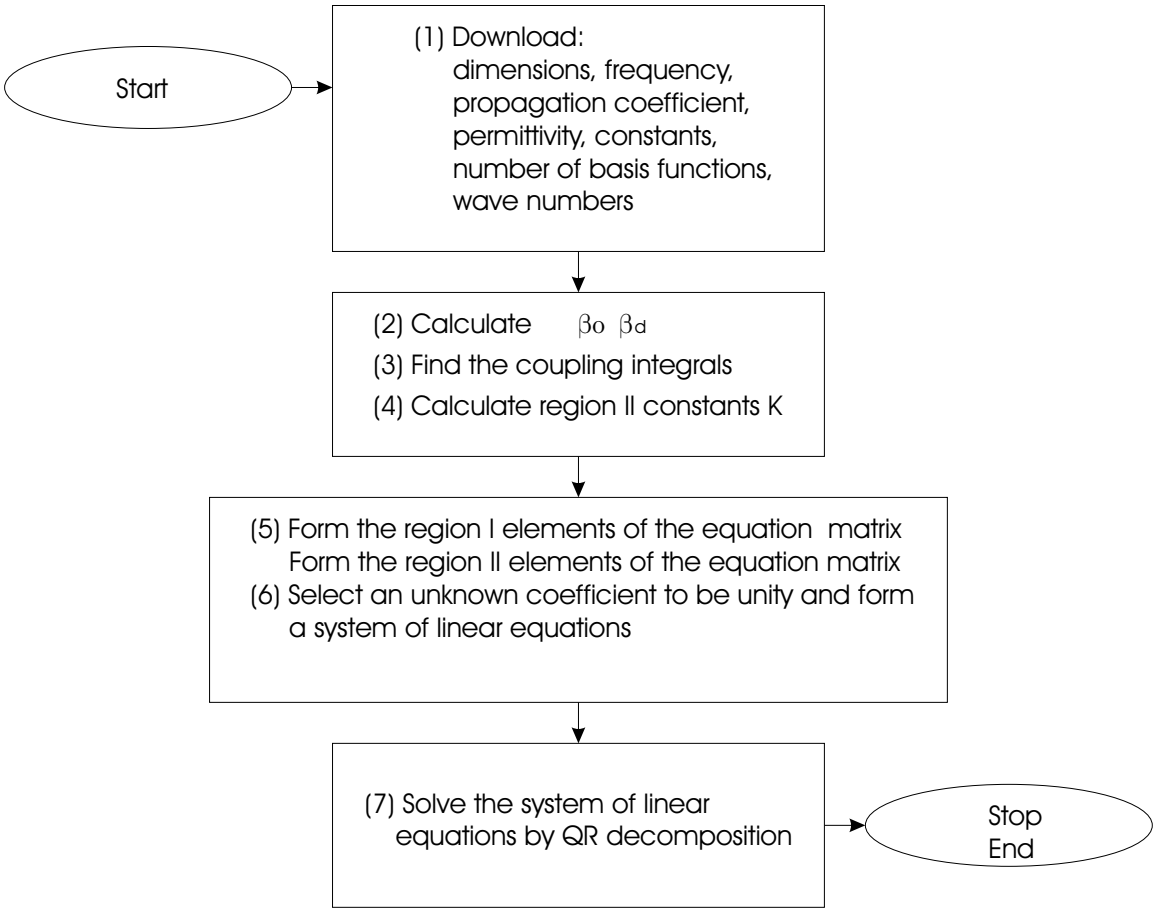

Figure 4.7: Flow chart of the program to find the unknown coefficients of the basis function equations associated with a mode of the shielded rectangular dielectric rod waveguide.

4.5.1 to find the propagation coefficients:

2. Calculate using equations (4.6) the wavenumbers of the air β_0 and dielectric rod β_d region materials.

3. Calculate an array of the coupling integrals of region II.

4. Calculate the constants K which are used to reduce the number of unknown coefficients in the region II equations.

5. This step is essentially the same as step 8 of section 4.5.1 but in this case an unknown coefficient is made unity (or some convenient factor) so that a column of the LHS of matrix equation (4.35) can be transposed to the RHS forming the

set of linear equations (4.36). Theoretically it does not matter which unknown coefficient is selected to be made unity and in practice only very small variations (<0.001%) were noted in calculated values of dielectric and shield wall losses (see Chapter 5) when a different selected coefficient was used. It is thought that the variation is associated with round off error as some of the matrix columns have elements that do not have as many significant figures as others. This is due to the very large range of element magnitudes that can occur in the matrix.

6. As an unknown coefficient has been removed but the number of equations remains the same the system now has more equations than unknowns. This overdetermined system of equations (4.36) can be solved for the normalised values of the unknown coefficients by QR decomposition using the Matlab operator '\'.

   A problem with rank deficiency of the equation matrix can be encountered when the number of basis functions used in calculation exceeds a threshold value. When this happens no solutions can be found. However the number of basis functions required for a desired degree of convergence to the extrapolated solution of the propagation coefficient (see sections 4.6.1 and 4.10.2) is well below this threshold.

If the unknown coefficients of the basis functions of a propagating mode are found the field patterns of the mode can be plotted. The flowchart of a program to create 2 dimensional plots in coordinate planes of interest is shown in Figure 4.8 and the details are as follows:

1. Download the parameters, including wavenumbers, and dimensions of the structure that was used in the previous program to calculate the unknown coefficients. Download the calculated basis function coefficients.
   Calculate using equations (4.6) the wavenumbers of the air β_0 and dielectric rod β_d region materials.
   Calculate the constants K which are used to reduce the number of unknown coefficients in the region II equations.

2. Provide a 'for' loop of the indices allocated to each mode so that the calculated

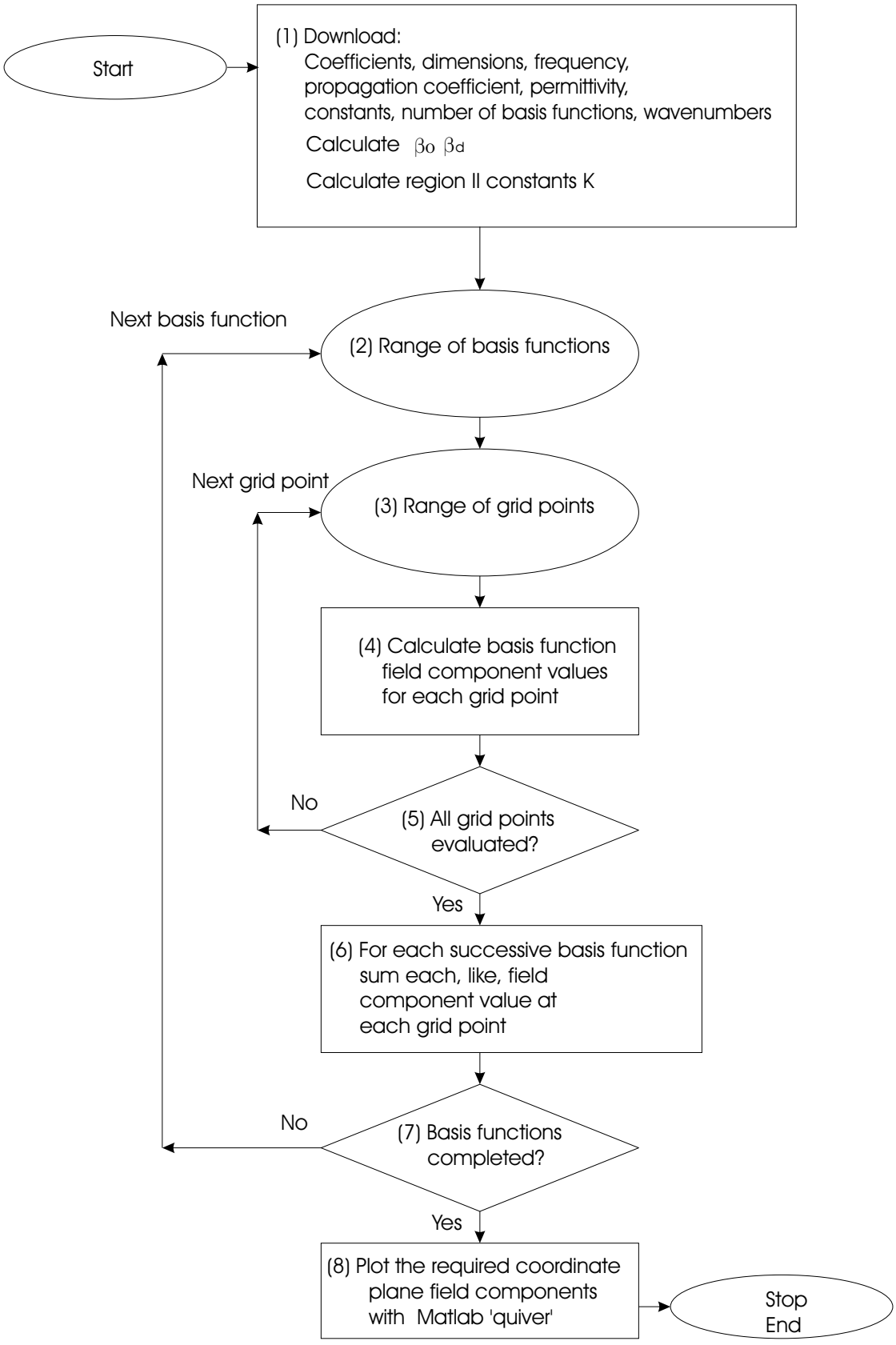

Figure 4.8: Flow chart of the program to plot the 2 dimensional coordinate plane field patterns of a propagating mode in the shielded rectangular dielectric rod waveguide.

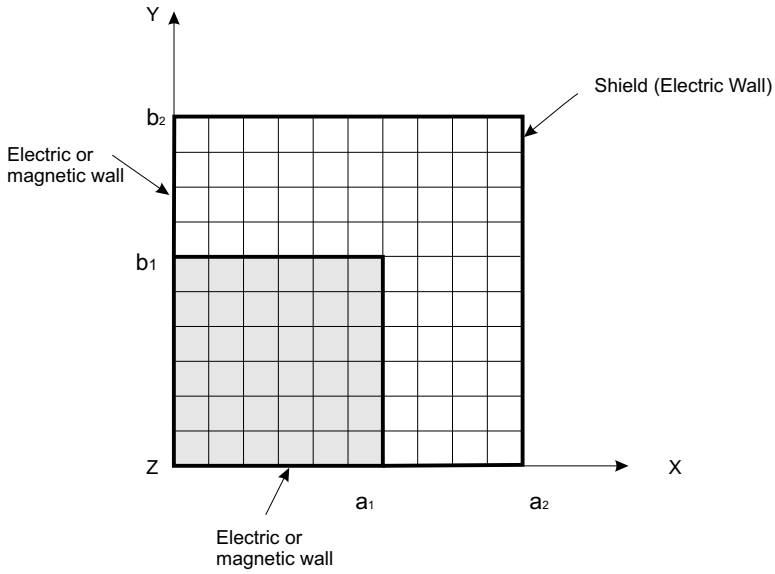

Figure 4.9: Example of a grid constructed to allow the plotting of 2 dimensional x-y coordinate plane field patterns of the shielded rectangular dielectric rod waveguide.

coefficients for each mode can be accessed as required.

3. Provide 'for' loops of the indices of coordinate points assigned to a plane at the intersection of grid lines. For example see Figure 4.9 where a grid has been assigned to the x y plane of quarter of the structure.

4. Using the basis function equations of Appendix B calculate the field intensities for each field component at a grid point in the desired plane.

5. Calculate the field component values until all points in the plane are completed for this mode.

6. For each successive mode sum all, like, component values at each point.

7. Continue until all basis functions assigned are used.

8. Plot the electric field components of a coordinate plane against each other by use of the Matlab function 'quiver'. Likewise for the magnetic field components of the same coordinate plane. This will create a 2 dimensional vector field representation of the electric field and one of the magnetic field corresponding to the previously calculated propagation coefficient.

A copy of the computer programs described in this section can be seen on the companion CD-ROM for this thesis and operating details are given in Appendix D.

4.6 Discussion and Comparison of Results with other Methods

To confirm the validity of this method the propagation coefficients were calculated for a number of frequency ranges and permittivity values, and compared to the results from other methods. All of the calculations and measurements reported here are for a square cross-section, ie a square dielectric rod symmetrically located within a square shield. The structure will be characterized by the aspect ratio $DDR = a_1/b_1$ for the dielectric rod and $SDDR = a_2/a_1$ for the shield. In some of the following results the normalization applied by Schweig & Bridges (1984) will be used, where V and B are the normalised frequency and propagation coefficient respectively.

$$\begin{aligned} V &= 2a_1\beta_0\sqrt{\varepsilon_{r2}} \\ B &= \frac{(\beta_z/\beta_0)^2}{\varepsilon_{r2}} \\ \beta_0 &= \omega\sqrt{\mu_0\varepsilon_0} \end{aligned} \tag{4.37}$$

The method described in this chapter gives the propagation coefficients of the possible modes for each symmetry used. The designations of the modes on the dielectric line in this chapter are same as that used by Marcatili, Goell and others. Modes will be identified as E^y_{mn} or E^x_{mn}, where x or y denotes the direction of polarization of the main electric field, and m and n are the number of maxima in the x and y directions over the x-y plane of the dielectric.

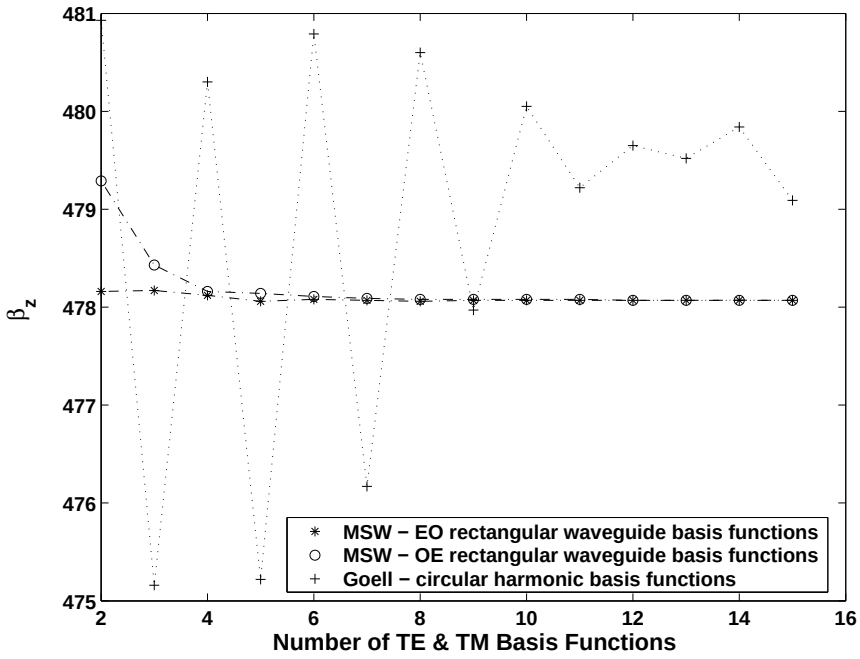

Figure 4.10: Comparison of the convergence properties of the Goell and MSW methods when used with a square cross-section dielectric rod waveguide ($\varepsilon_{r2} = 37.4$) in free-space. The propagation coefficients of the degenerate modes E_{11}^x and E_{11}^y are calculated using EO and OE symmetry respectively.

4.6.1 Comparison of Method Convergence Properties

A comparison of the convergence properties of Goell's method and the modified Solbach and Wolff method (MSW), versus the number of basis functions used, is shown in Figure 4.10. The dielectric rod was square ($DDR = 1$, 6.025mm x 6.025mm) with $\varepsilon_{r2} = 37.4$, and in free space with a frequency of 4.532GHz (V=7 nornmalised frequency). The square shield dimension ratio in the MSW method had $SDDR = 3$ which is of sufficient distance from the dielectric so as to be a good approximation of free space. Evidence of this can be seen in Figure 4.11 where the propagation coefficient results are virtually constant above an $SDDR$ of 2. The propagation coefficients of the degenerate modes E_{11}^x and E_{11}^y are calculated using EO and OE symmetry respectively.

The convergence of the MSW method for both symmetries shown in Figure 4.10 is good with the propagation coefficient values calculated with 4 TM^y and 4 TE^y basis functions within 0.02% of that at 15 TM^y and 15 TE^y basis functions.

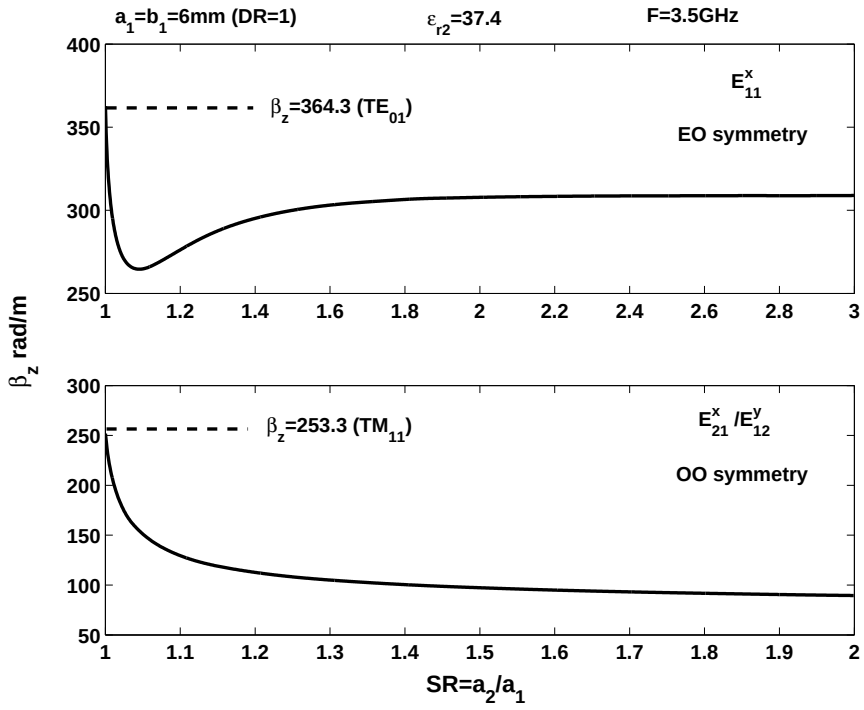

Figure 4.11: Effect of the proximity of the shield on β_z, $\varepsilon_{r2} = 37.4$, $a_1 = b_1$=6mm, frequency=3.5GHz.

At 11 TM^y and 11 TE^y basis functions, and above, the MSW method and Goell's results are within 0.4%.

4.6.2 The Effect on the Propagation Coefficient of the Proximity of the Shield to the Dielectric Rod

The effect of the proximity of the shield on the propagation coefficients of the first few modes to propagate (E_{11}^y and E_{21}^x/E_{12}^y) is shown in Figure 4.11. It can be seen that for a shield-to-dielectric dimension ratio value $SDDR > 2$ the shield has only a small effect on the propagation coefficient. These results are verified by considering the situation where the shield size approaches that of the dielectric ($SDDR = 1$). In both cases the propagation coefficients found using the MSW method approached those calculated for dielectric filled rectangular waveguide (Pozar, 1998, p. 128), as shown on the figure.

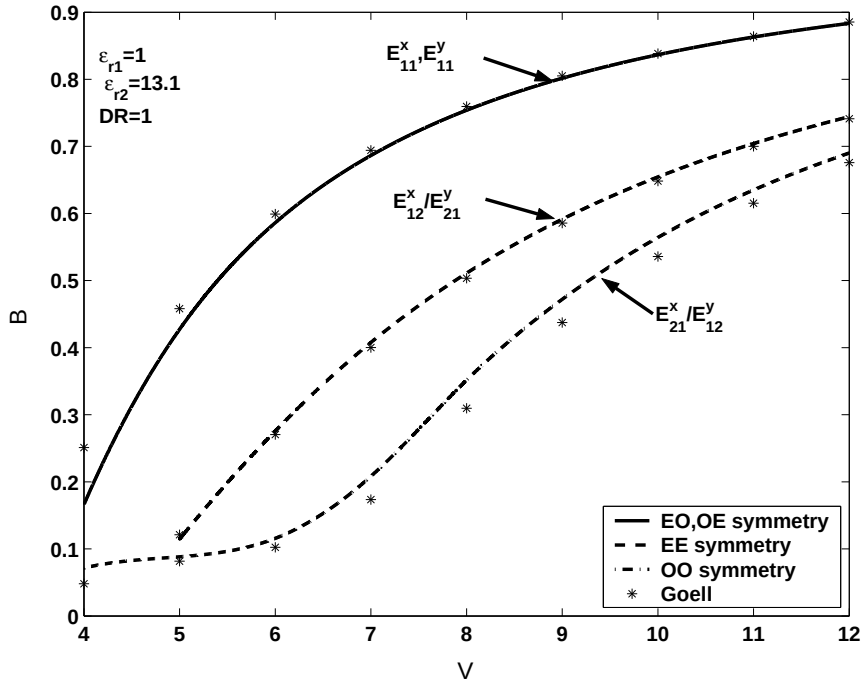

Figure 4.12: Comparison of the β_z calculation methods of MSW and Goell for a square cross-section dielectric rod waveguide in free-space, where B and V are the normalised propagation coefficient and frequency respectively ($\varepsilon_{r2} = 13.1$).

4.6.3 Comparison of Methods used for Calculation of the Rod Propagation Coefficient in Free Space

With the dielectric in free space, $\varepsilon_{r2} = 13.1$ and $DDR = 1$, Figure 4.12 shows the propagation coefficients of the first modes to propagate for normalised frequencies from $V = 4$ to $V = 12$. To simulate a free-space situation, $SDDR = 3$ is used in the MSW program. One can see that there is good agreement with the free space method of Goell. Some differences at low frequencies are due to the effect of the use of the shield in the MSW program. Modes E^x_{11} and E^y_{11} are degenerate while E^x_{21}/E^x_{12} and E^x_{12}/E^x_{21} are degenerate and coupled (discussed later in section 4.7).

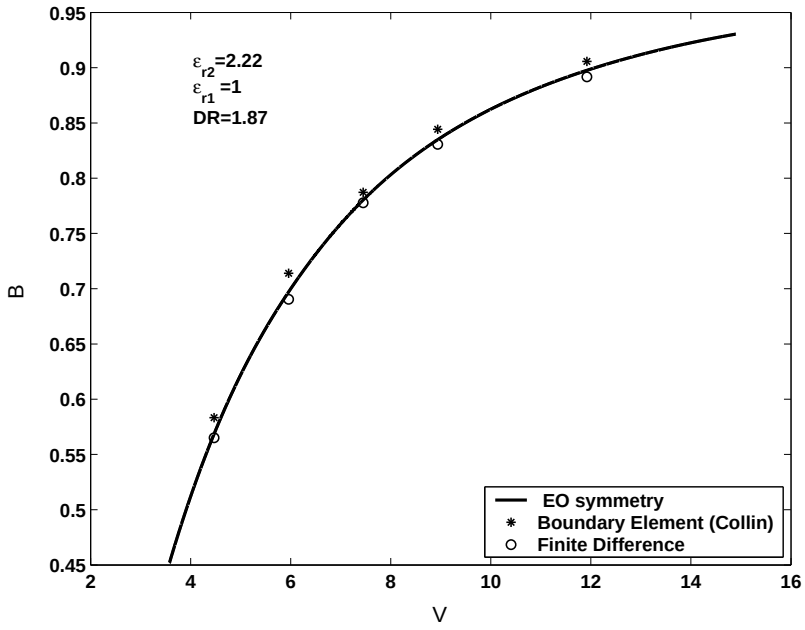

Figure 4.13: Comparison of the β_z calculation methods of MSW, the boundary element method of Collin and the finite difference method of Schweig and Bridges for a shielded square cross-section dielectric rod waveguide, $SDDR = 1.87$, $\varepsilon_{r2} = 2.22$, where B and V are the normalised propagation coefficient and frequency respectively.

4.6.4 Comparison of Methods for Calculation of the Shielded Dielectric Rod Propagation Coefficient

The MSW method with EO symmetry shows good agreement with propagation coefficients obtained by Collin (1991, pp.454-459)(Collin & Ksienski, 1987), using a boundary element method, and the finite difference method of Schweig & Bridges (1984). These results are shown in Figure 4.13. The mode is E_{11}^x, $DDR = 1$, $SDDR = 1.87$ and $\varepsilon_{r2} = 2.22$.

4.6.5 Propagation Coefficient verses Frequency Mode Diagram of the Shielded Dielectric Rod Waveguide

The propagation coefficient verses frequency mode diagram, of the first few modes to propagate, is shown in Figure 4.14. The 12mm square dielectric has a permittivity

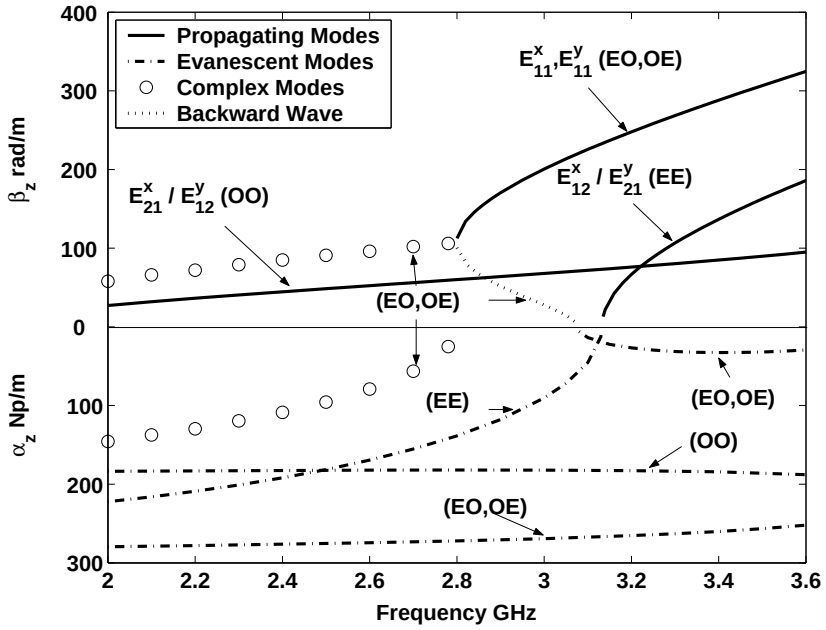

Figure 4.14: Mode diagram for the first few modes to propagate in a shielded dielectric rod waveguide plus some of the associated complex modes, evanescent modes and backward waves. $DDR = 1(a_1$=6mm), $SDDR = 2(a_2$=12mm),$\varepsilon_{r2} =$ 37.13. The modes are labeled with their associated symmetry in parentheses.

$\varepsilon_r = 37.13$, the shield is 24mm square ($SDDR = 2$). The figure shows differences from that of the dielectric image line reported by Strube & Arndt (1985). The MSW method (for a shielded dielectric rod waveguide with $DDR = 1$ and $SDDR = 2$) reveals a coupled E^x_{21}/E^y_{12} mode which is dominant in this structure and also the E^y_{11} mode is associated with a degenerate E^x_{11}. The E^x_{11} and E^x_{21}/E^y_{12} modes and their associated higher order modes do not occur in the dielectric image line and the studies of this structure in Solbach & Wolff (1978) and Strube & Arndt (1985) use only a combination of OE and EE symmetry. Some of the complex, evanescent and backward wave modes for the shielded dielectric rod, mentioned in section 4.4.3, are also shown in Figure 4.14. The symmetry associated with each mode is shown in parentheses.

A point of interest about this structure is that the propagating frequency range of the hybrid modes shown is well below the cutoff frequency of an empty rectangular waveguide of the same dimensions as the shield, ie 6.2457GHz for TE_{01}/TE_{10} modes in a 24mm square waveguide.

4.7 Field Patterns of the First Few Modes to Propagate on the Shielded Dielectric Rod Waveguide

The transverse electric and magnetic fields of the E_{11}^x mode, in one quarter of the structure, and determined from EO symmetry, are shown in Figure 4.15. The E_{11}^y mode is degenerate with the E_{11}^x mode and is shown in Figure 4.16. It has OE symmetry. Both these modes have a calculated propagation coefficient of $\beta_z = 305.42$ at $3.5GH_z$. The 12mm square dielectric has a permittivity $\varepsilon_r = 37.13$, the shield is 24mm square (SDDR=2).

The E_{21}^x/E_{12}^x coupled modes have OO symmetry. In a square cross-section, using the same parameters, these are also degenerate, as they have the same propagation coefficient $\beta_z = 89.2$. The resultant field plot is a superposition of both modes, as shown in Figure 4.17. These modes are coupled together, as described by Goell (1969, p. 2150), such that their propagation coefficients remain locked together for a range of cross-section aspect ratios. The coupled modes separate when DDR is somewhat greater or less than 1 depending on the frequency. For example if, for this same structure, $DDR = 4/3$ (a_1=8mm, b_1=6mm) is used, the E_{21}^x mode is now uncoupled and is found to have a propagation coefficient of $\beta_z = 136.4$. The E_{12}^y mode was found not to propagate. The field pattern of the mode is shown in Figure 4.18. If $DDR = 3/4$ (a_1=6mm, b_1=8mm) is used instead, the roles of the modes are reversed. The same type of situations occur when the E_{12}^x/E_{21}^y modes are produced with EE symmetry (see Figure 4.19).

It is interesting to note that the transverse field patterns of Figures 4.16 (E_{11}^x) and 4.17 (E_{21}^x/E_{12}^x) in the dielectric rod are not unlike the TE_{10} and TM_{11} modes in dielectric filled rectangular waveguide respectively, as was indicated in section 4.6.2. The E_{12}^x/E_{21}^y coupled modes however cut off as $SDDR$ approaches 1 and have no similarity to any rectangular dielectric filled waveguide mode.

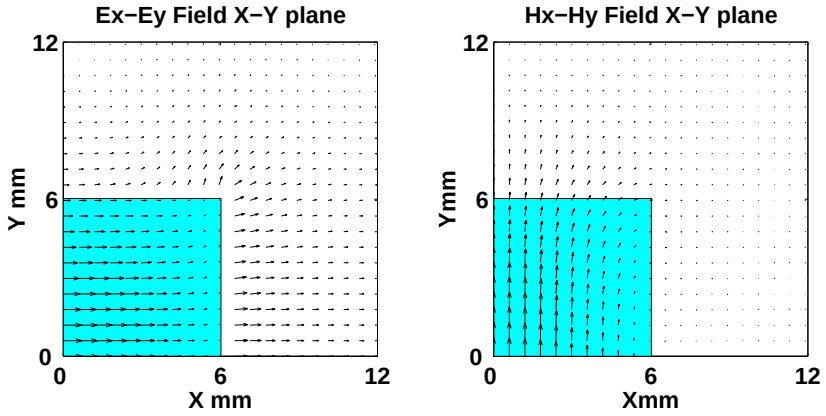

Figure 4.15: Plot of the electric and magnetic fields ($\varepsilon_{r2} = 37.13$) of the E_{11}^{x} mode from the MSW method and EO symmetry. Quarter of the structure.

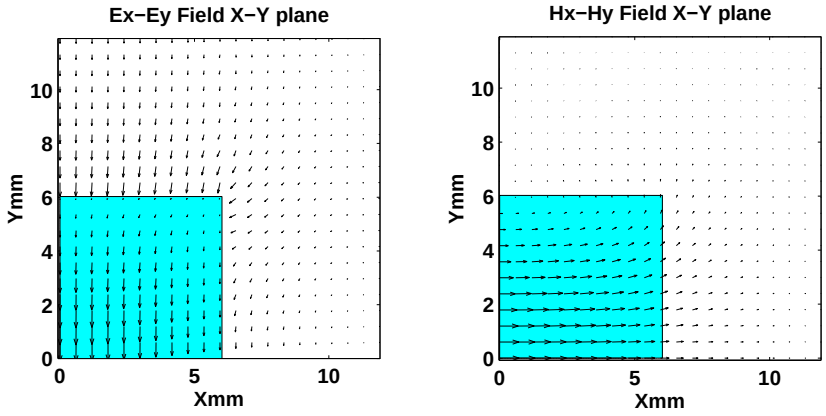

Figure 4.16: Plot of the electric and magnetic fields ($\varepsilon_{r2} = 37.13$) of the E_{11}^{y} mode from the MSW method and OE symmetry. Quarter of the structure.

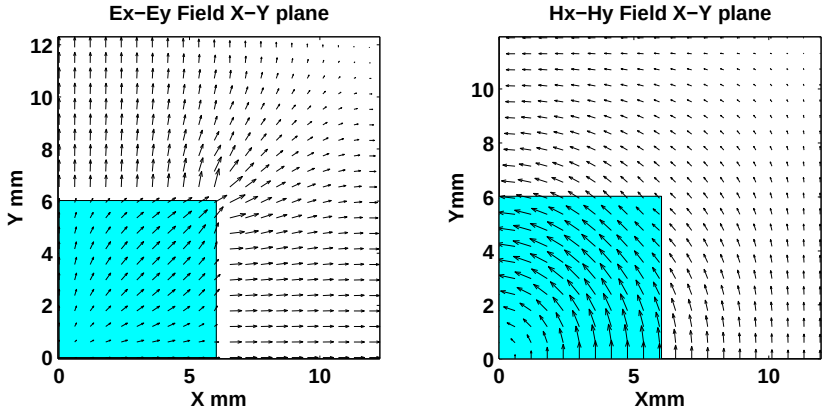

Figure 4.17: Plot of the electric and magnetic fields of the coupled E_{21}^{x} and E_{12}^{y} modes with dielectric aspect ratio $DDR = 1$, OO symmetry. NB electric field intensity in the dielectric x 5. Quarter of the structure.

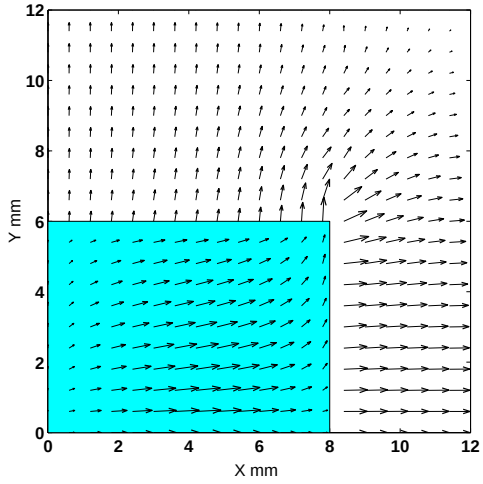

Figure 4.18: Plot of the electric field ($\varepsilon_{r2} = 37.13$) of the E_{21}^x mode with dielectric aspect ratio $DDR = 1.33$ (E_{12}^y now non propagating), OO symmetry. NB electric field intensity in the dielectric x 10. Quarter of the structure.

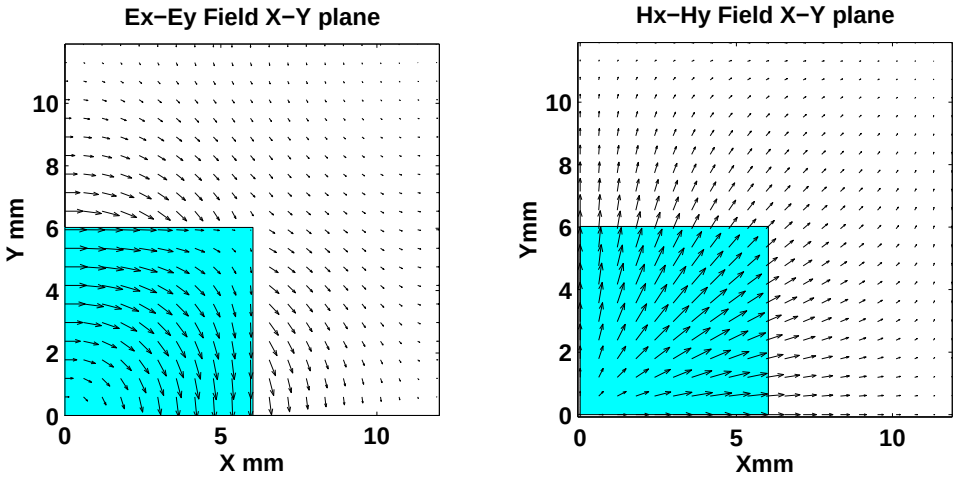

Figure 4.19: Plot of the electric and magnetic fields of the coupled E_{12}^x and E_{21}^y modes with dielectric aspect ratio $DDR = 1$, EE symmetry. Quarter of the structure.

The electric field intensities in the dielectric in Figures 4.17 and 4.18 have been artificially increased by factors of 10 and 5 respectively in the plots. This is so that field patterns in the dielectric can be shown effectively at the same time as the larger intensity field of the air region.

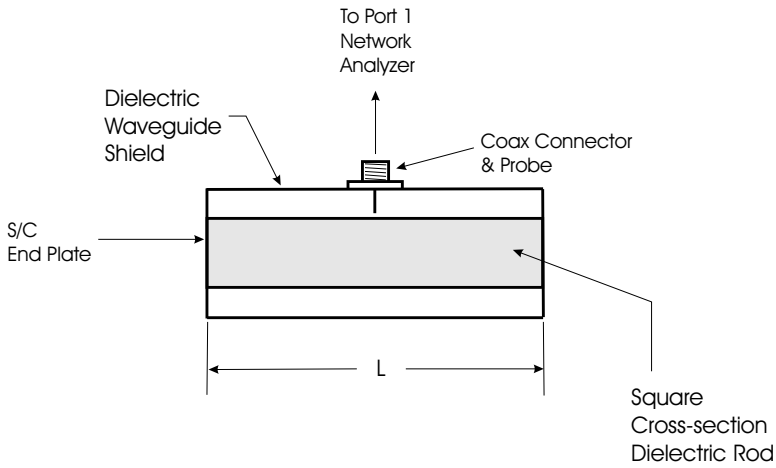

Figure 4.20: Setup for an S_{11} measurement of the shielded dielectric waveguide.

4.8 Measurement Technique

Apart from the boundary element method results of Collin mentioned in section 4.6, there does not appear to be any published results on the specific effects of the shield on the propagation coefficient of the structure described in this chapter. Therefore to verify the method when the shield is close to the dielectric, a measurement approach was devised whereby the propagation coefficient could be calculated from the measured reflection coefficient S_{11} of the structure. A length L of shielded square cross-section dielectric rod was fitted with end plates, and a connector and probe were installed mid way to allow measurement by a vector network analyzer. See Figure 4.20. To provide a situation where there would be a sufficient effect from the shield, dielectric dimensions of a_1=b_1=6 mm and a_2=b_2=9 mm ($SDDR = 1.5$) where chosen. The dielectric used was 153.3 mm long and had a nominal relative permittivity of 37.4 ± 1. This structure behaves as a resonant cavity and the resonant frequencies produced are related to multiple half wavelengths between the plates and can be measured at minimum points in the S_{11} magnitude data. The propagation coefficient at these points can then be calculated from:

$$\beta_z(N) = \frac{\pi N}{L} \tag{4.38}$$

where N is the number of multiple half wavelengths of the resonant modes that can exist in the shielded dielectric rod waveguide, and L is the distance between the planes.

These propagation coefficient values $\beta_z(N)$ can then be compared to calculated values from the MSW method at the measured resonant frequencies.

4.9 Comparison of Calculated and Measured Results

A plot of calculated propagation coefficient over a frequency range that covers the first few modes to propagate is shown in Figure 4.21. The coupled E^x_{21}/E^y_{12} modes are dominant, and the degenerate modes E^x_{11} and E^y_{11}, which are normally dominant in the free space situation, are found to be cut off at just below 2.9GHz.

With this frequency range applied to the test set up of Figure 4.20 the S_{11} data produced is as shown in Figure 4.22. It was found that the frequencies at the resonant dips shown were within 1% of calculated resonant frequencies for the E^x_{21}/E^y_{12} coupled and E^x_{11}, E^y_{11} degenerate modes. The E^x_{12}/E^y_{21} mode did not couple to the measurement probe, nor did $N = 5$ for the E^x_{21}/E^y_{12} mode and $N = 11$ for the E^x_{11}, E^y_{11} modes.

It can be seen that some of the resonant dips associated with E^x_{11} and E^y_{11} are in pairs and some are not. Some of these are too small to be seen due to the scale of the figure. The pairing indicates that these modes are not quite degenerate in the test unit due to some asymmetry in its dimensions. In these cases the measurement frequency was averaged. Where only a single resonant dip was measured it appears that either the E^x_{11} or E^y_{11} mode did not couple sufficiently to the probe to be visible or they overlap.

The figure also shows that there are no resonances below 2.9GHz for the E^x_{11} and E^y_{11} modes and so the E^x_{21}/E^y_{12} coupled mode is truly dominant. The propagation coefficients, calculated from (4.38) at the measured frequencies for E^x_{11}, E^y_{11}, are compared against MSW calculated values in Figure 4.23. An estimated permittivity of the dielectric of $\varepsilon_{r2} = 37.13$ was used. The extremes of the permittivity tolerance for this dielectric are also shown in the figure.

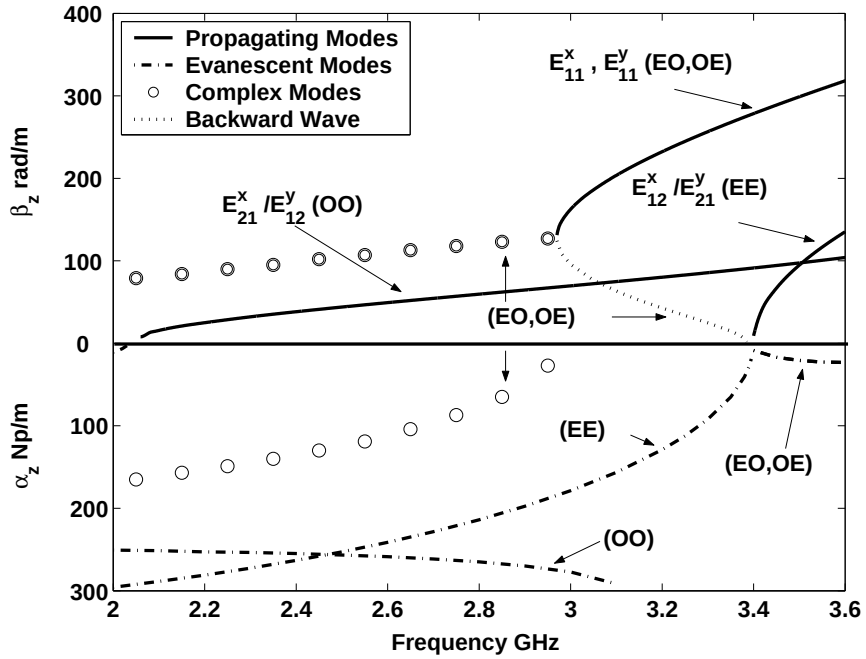

Figure 4.21: Calculated propagation coefficient values for the first few modes to propagate, shield-to-dielectric dimension ratio $SDDR = 1.5$. The modes are labeled with their associated symmetry in parentheses.

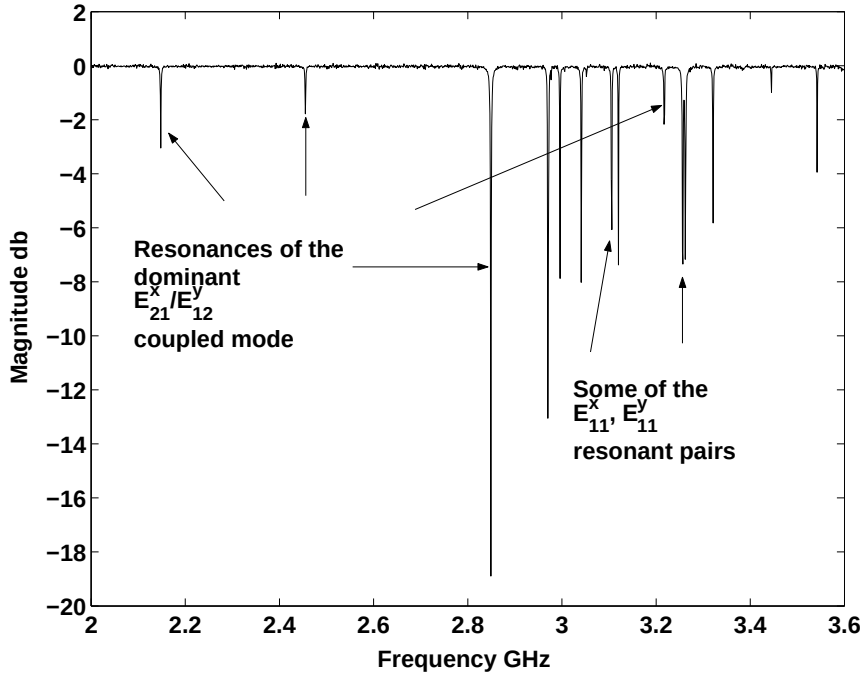

Figure 4.22: S_{11} Magnitude Data for the frequency range 2.0 to 3.6 GHz

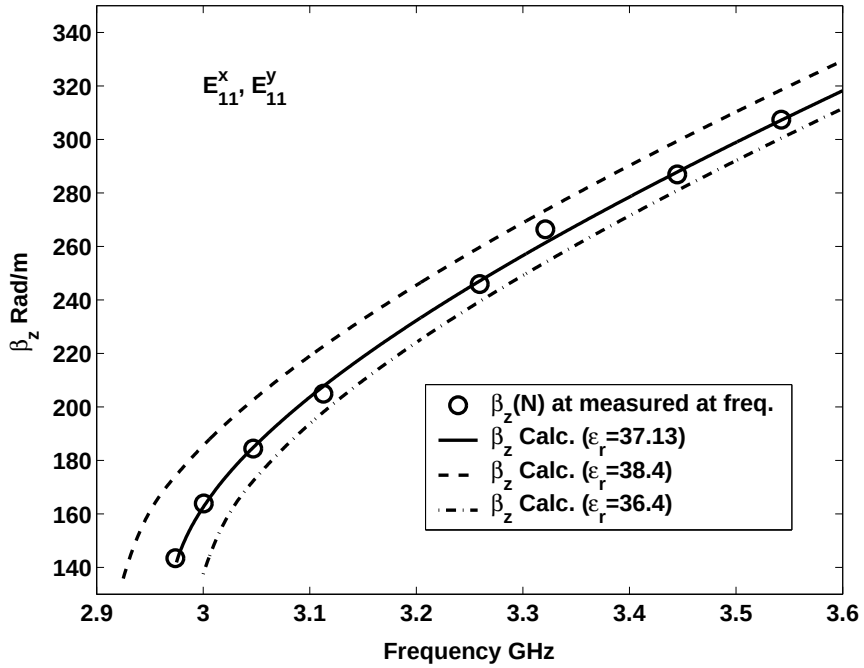

Figure 4.23: Comparison of $\beta_z(N)$ propagation coefficients, at the measured resonant frequencies, and calculated propagation coefficients for the E_{11}^x or E_{11}^y mode.

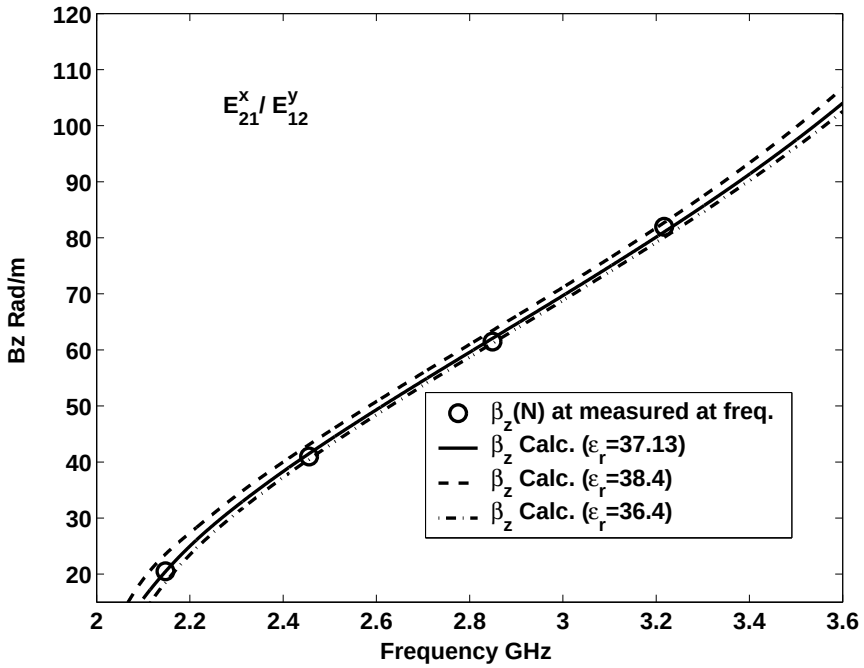

Figure 4.24: Comparison of $\beta_z(N)$ propagation coefficients, at the measured resonant frequencies, and calculated propagation coefficients for the E_{21}^x/E_{12}^y coupled mode.

The measured propagation coefficient values for the E_{11}^x, E_{11}^y modes are within 2% of the MSW values above 3GHz. Similarly the measured propagation values for the E_{21}^x/E_{12}^y coupled mode are also within 2% as shown in Figure 4.24.

4.10 Problems and Limitations of the Mode Matching Solution

4.10.1 Wavenumber Calculations

During the mode matching program procedure, wavenumbers $\beta_{y_n}^{(II_2)}$ and $\beta_{y_n}^{(II_1)}$ for both the TE and TM modes, are calculated from the transcendental equations of Appendix B.2 and equation (4.20) using the Matlab function 'Fzero' or some other root finding algorithm. Caution has to be observed while searching that none in the selected range are overlooked. Missed values generally occurred when, in an effort to speed up the root finding process, too large a step size was used between the wavenumber estimates. This can have the effect that only one wavenumber will be found when two wavenumbers are very close together or a wavenumber will be missed when one is very close to singularity points that occur in the transcendental equations. See Figure 4.25. This problem can cause poor convergence and inaccuracy in propagation coefficient calculations and in extreme cases no solution will be found. Fortunately this problem can be detected easily by graphing the calculated propagation coefficient values verses frequency and checking for any discontinuity. The step size is then decreased for this particular frequency until the discontinuity disappears. For example, as long as the wavenumber step size was equal to or below 0.5 when compiling the data for Figures 4.14 and 4.21, no wavenumber problems occurred.

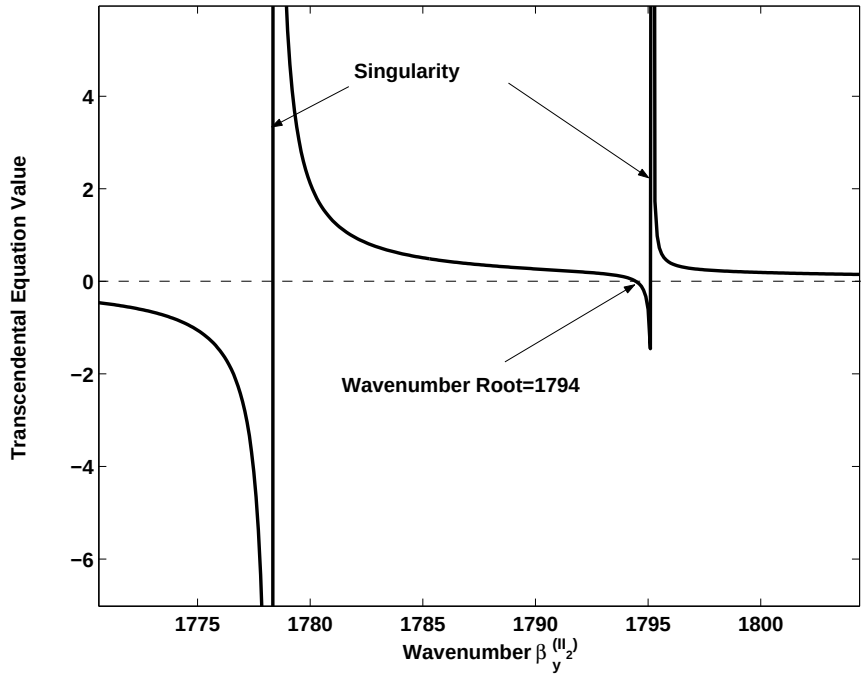

Figure 4.25: A root of a transcendental equation close to a singularity. This wavenumber can be missed by a root finding function if the estimate step size is too high.

4.10.2 Propagation Coefficient Calculation

The method used in the coaxial resonator problem of Chapter 3 used testing functions from one region with the electric basis functions, and from the other region with the magnetic basis functions. This allowed the final equation/testing function matrix (see equation (4.35)) to be in the correct form for solution so that different numbers of basis functions could be used in each region. The modified Solbach and Wolff method however uses testing functions from region I only with the electric and magnetic basis functions. This enables simple expansion of the tangential basis function components at the mode matching boundary, as the integrals formed from the orthogonality relations, are easy to solve. The consequence of this however is that, for the final equation/testing function matrix to be in the correct form, equal numbers of basis functions must be used in regions I and II. Fortunately this does not create any problems with relative convergence (Mittra & Lee, 1971) (Leroy, 1983).

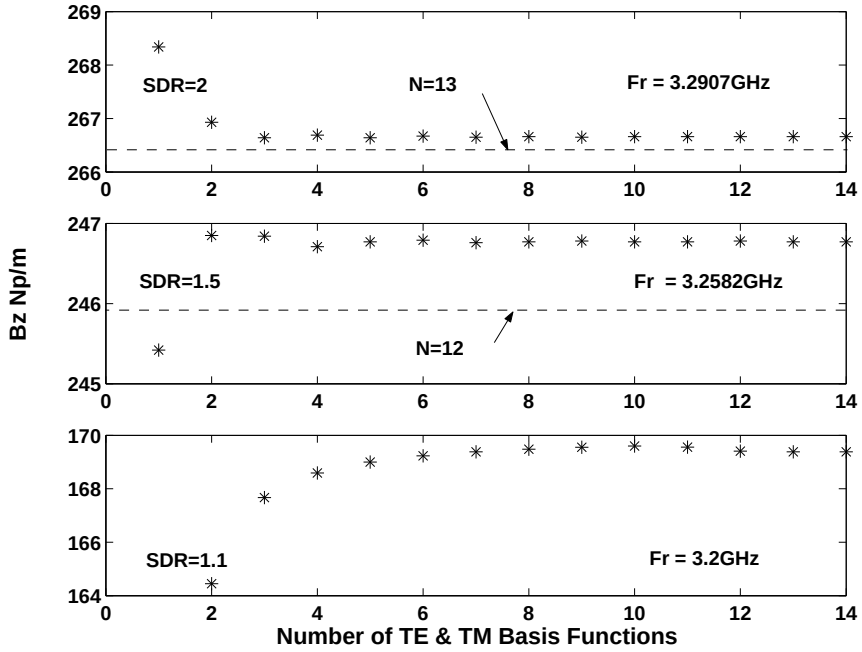

Figure 4.26: Convergence properties of rectangular shielded dielectric rod resonator for different shield-to-dielectric dimension ratios $SDDRs$ and a comparison with the propagation coefficients corresponding to measured resonant frequencies.

The convergence properties of the MSW method using EO symmetry for three different shield square cross-section sizes are shown in Figure 4.26. The dielectric is of square cross-section (12mm x 12mm) and $\varepsilon_r = 37.13$. Shield-to-dielectric ratios $SDDR$ of 2.0, 1.5, and 1.1 are calculated. The degree of convergence can be observed by comparing the propagation coefficient values at 4 and 14 TE and TM basis functions. For $SDDRs$ of 2 and 1.5 these are within 0.002% and 0.025% respectively. For $SDDR = 1.1$, where the shield is a lot closer to the dielectric, the propagation coefficient is within 0.5% but reducing to 0.15% at 10 TE and TM basis functions.

With reference to the resonator set up of section 4.8, the dashed lines in the upper and centre graphs of Figure 4.26 are propagation coefficients at N=13 and N=12 half wavelengths respectively, calculated from the relationship $\beta_z(N) = \frac{\pi N}{L}$ ($L = 153.3mm$). The propagation coefficient points in the upper and centre graphs were calculated using the measured frequencies at these N half wavelengths. The difference in propagation coefficient values at 14 TE and TM basis functions is less than 0.1% for $N = 13$ and less than 0.4% for $N = 12$.

There is a maximum limit to the number of basis functions that can be used in calculation. This is due to the very large numbers that occur when trigonometric functions are evaluated with imaginary arguments which can exceed the maximum floating point number of the computer. The indication of this is a message from the software (Matlab etc) declaring mathematically undefined operations in the equation/testing function matrix and that no solution is possible. This problem can be overcome for practical numbers of basis functions by multiplying the equation/testing function matrix with a suitable constant. For calculated values within 1% of those measured no more than 14 basis functions were ever needed in this research and this value was always well below the onset of any numerical problems. For example a result for the structure with $SDDR = 2$ depicted in the top graph of Figure 4.26 could still be obtained with 35 TE and TM basis functions. The structure with $SDDR = 1.1$ in the lower graph did have numerical problems and failed to give a result at 31 TE and TM basis functions. However, convergence to a sufficiently constant value had occurred, as shown, at less than half this number of basis functions.

4.10.3 Unknown Coefficients and Field Plotting

As was the case for the coaxial resonator of Chapter 3 it was found that there is a limit to the number of basis functions that can be used in the system of equations, before ill-conditioning occurs in the form of rank deficiency. This is due to the very large dynamic range of the element values in the matrix, which can approach the limited numerical range of the computer. The element values in some rows are rounded off to the extent that they become indistinguishable with other rows creating the rank deficiency. However the number of basis functions required for a reasonable degree of convergence (see sections 4.6.1 and 4.10.2) is well below the limit of about 10 to 12 TE and TM basis functions (depending on the dimensions of the structure).

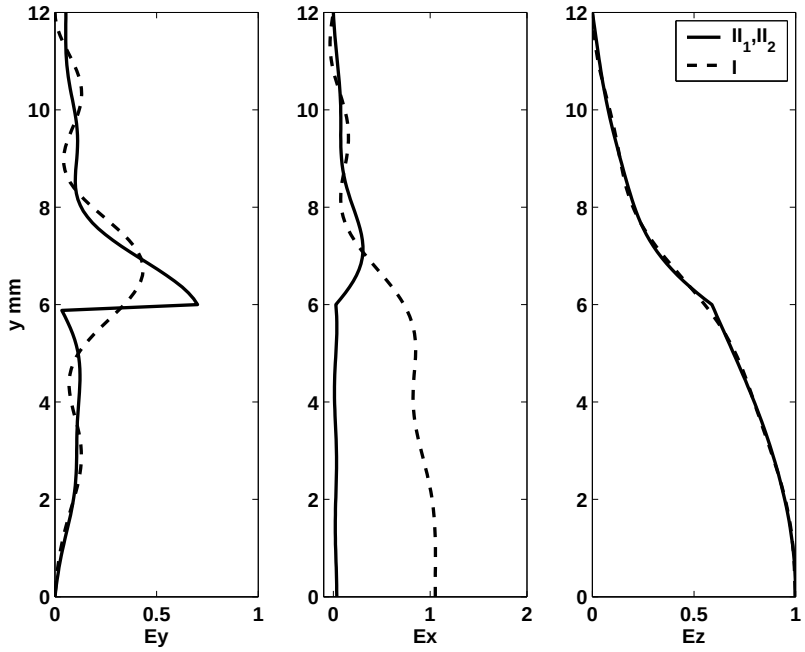

Figure 4.27: Normalised intensities of the electric field components at the mode matching boundary. Region II_1/II_2 is compared to region I. $N = 8$, $SDDR = 2$, $a_1 = b_1 = 6mm$, $a_2 = b_2 = 12mm$

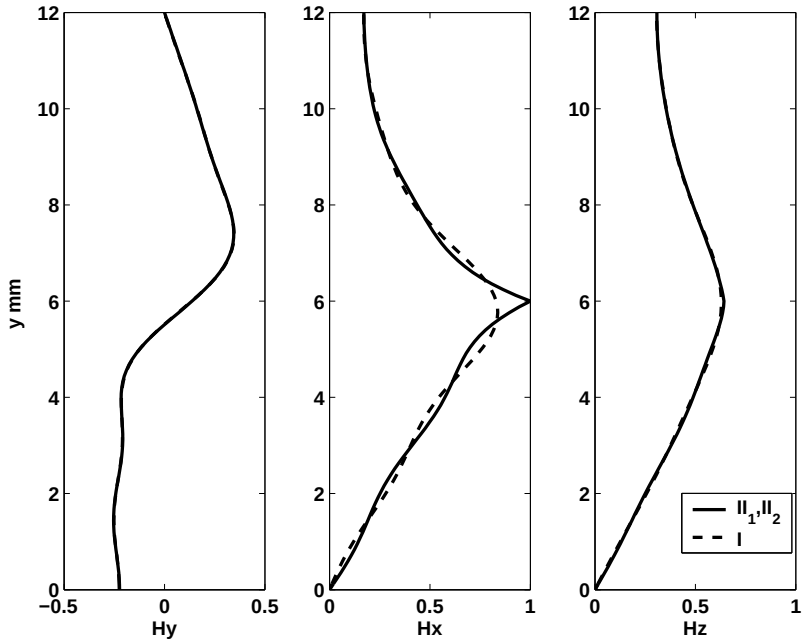

Figure 4.28: Normalised intensities of the magnetic field components at the mode matching boundary. Region II_1/II_2 is compared to region I. $N = 8$, $SDDR = 2$, $a_1 = b_1 = 6mm$, $a_2 = b_2 = 12mm$

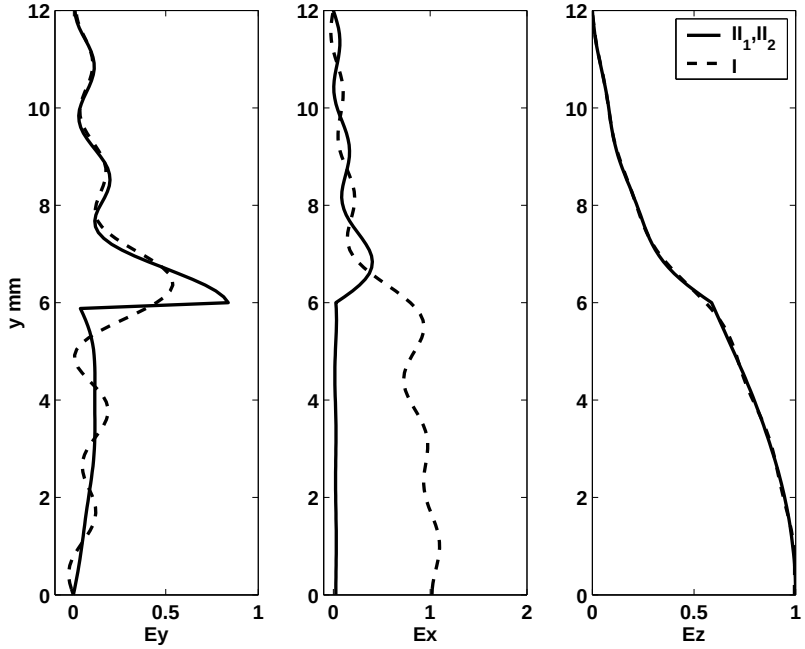

Figure 4.29: Normalised intensities of the electric field components at the mode matching boundary. Region II_1/II_2 is compared to region I. $N = 11$, $SDDR = 2$, $a_1 = b_1 = 6mm$, $a_2 = b_2 = 12mm$

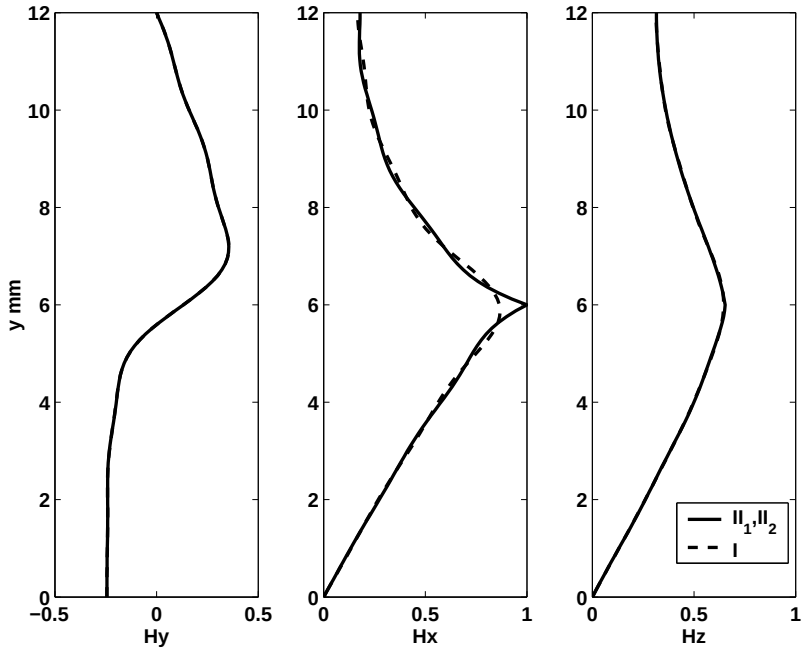

Figure 4.30: Normalised intensities of the magnetic field components at the mode matching boundary. Region II_1/II_2 is compared to region I. $N = 11$, $SDDR = 2$, $a_1 = b_1 = 6mm$, $a_2 = b_2 = 12mm$

In Chapter 5 it will be shown that values of attenuation loss for the rectangular shielded dielectric rod waveguide can be calculated and these results can be verified by comparing calculated and measured Q of a resonator, using this waveguide, to around 8% (section 5.7). In those calculations only 8 TE and TM basis functions were used to find the unknown coefficients of the basis functions and the reason for this can be seen by comparing Figures 4.27 and 4.28 with Figures 4.29 and 4.30. The first two figures show the matching of the basis function field components at the mode matching boundary between regions I and II (see Figure 4.2) for 8 TE and TM basis functions. The matching is good with some components matching so well that the curves are nearly coincident. The step in the E_x component values below 6mm is due to the change in permittivity at the boundary. This step in permittivity also creates poorer matching of the E_y component near 6mm due to the the field solution singularity at the dielectric rod corner (Sudbo, 1992). In this case the discontinuity creates a $r^{-1/3}$ singularity (Collin, 1991, p. 27) which describes the variation in the field solution for distance r from the corner. The ringing effects in E_x and E_y can be likened to the Gibbs phenomenon in Fourier analysis where a series will converge slowly and exhibit oscillations near discontinuities (Sudbo, 1992). The last two Figures (4.29 and 4.30) are for 11 TE and TM basis functions and show matching which is not significantly different to the first two with only 8 TE and TM basis functions.

4.11 Conclusion

A rigorous method for the computation of the propagation coefficients and field patterns of the fundamental modes in a shielded rectangular dielectric rod waveguide has been presented. The method, based on that of Solbach and Wolff, gives closely comparable results to that of Goell in free space, and the boundary element method of Collin, and has been verified by experiment for the case of a shield close to a dielectric of high permittivity. The method also reveals the original result that when the dielectric is shielded there exists a dominant E^x_{21}/E^y_{12} coupled modes, a fundamental E^x_{11} mode, and all the higher order modes associated with OO and EO symmetry not previously

identified (section 4.2). The method allows the effect of shield proximity to be assessed, and so has application to the design of cavity filters incorporating rectangular parallelepiped or cubic dielectric resonators. It is easily extended to include calculation of both dielectric losses, and conductor losses in the shield wall. This will be the subject of Chapter 5. There are some limitations to the method but knowledge of these will allow the achievement of sufficiently accurate results for most purposes. This work could provide a basis for the calculation of the resonant frequencies of fundamental mode dielectric-loaded cavity resonators.

Chapter 5

Attenuation of a Shielded Rectangular Dielectric Rod Waveguide

5.1 Introduction

Rectangular dielectric waveguides are used in integrated optics, millimeter-wave integrated circuits and as transmission lines. Compared to metal waveguides, at millimeter-wave frequencies, they have lower propagation loss (depending on the dielectric loss), lower cost and are easier to fabricate (Lioubtchenko et al., 2003). They are also significantly smaller (Engel-Jr. & Kathi, 1991). Shielded square cross-section dielectric resonators are also used in filter applications e.g. in multimode cubic dielectric resonator filters (Hunter, 2001).

The loss in open rectangular dielectric waveguides is due to that in the dielectric. However, if the waveguide is surrounded by a rectangular metallic shield, to prevent interference (see Figure(5.1)), then the total loss of the waveguide will also include loss due to induced currents in the inner surface of the shield walls. In Chapter 4 a modified

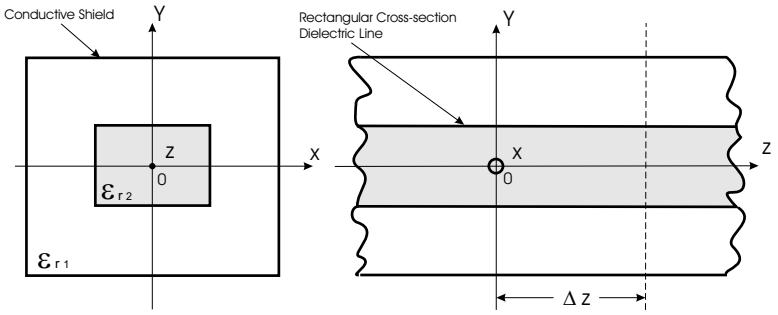

Figure 5.1: Shielded dielectric rod waveguide

version of the mode matching method devised by Solbach & Wolff (1978), called the MSW method, was used to find the propagation coefficients and field patterns of the hybrid modes of a shielded rectangular dielectric waveguide.

In this chapter the calculated fields for the commonly used E_{11}^y mode (Lioubtchenko et al., 2003) will be employed to find the wall and dielectric losses of the waveguide and hence its attenuation. For the E_{11}^y mode and the dominant E_{21}^x/E_{12}^y coupled mode the effect of the proximity of the shield on the attenuation will also be evaluated.

All of this chapter is original work, and the principal results have been submitted for publication in *IEEE Transactions on Microwave Theory and Techniques* (Wells & Ball, 2005*a*).

5.2 Analysis of Power Loss in the Dielectric Waveguide

One quarter of the cross-section of the rectangular dielectric waveguide is shown in Figure 5.2. In this chapter it will be considered that regions I and II_1 will be free space so that the permittivity ε_{r1} will be ε_0. From Poynting's theorem (Pozar, 1998, p. 28) the time average power P_0 over the full transverse cross-section ($z = 0$) of a wave

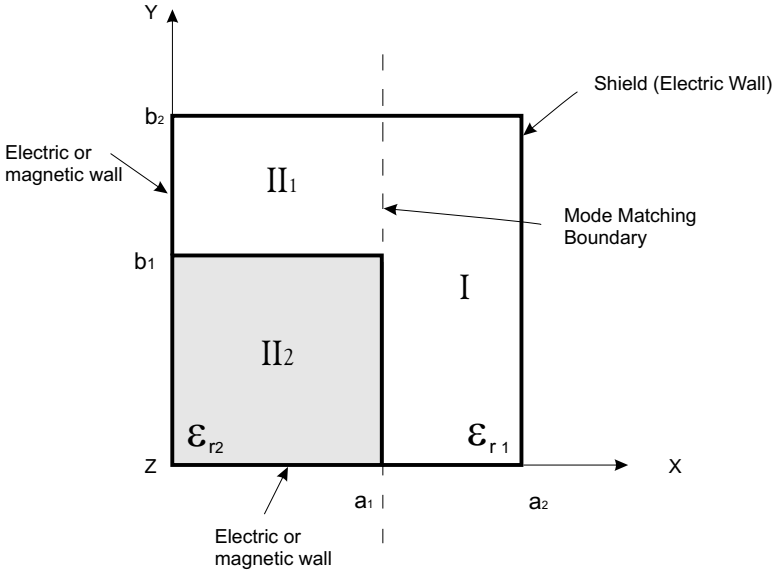

Figure 5.2: One quadrant of the cross-section, showing mode matching regions

traveling in the plus z direction can be written as:

$$P_0 = \frac{1}{2}\,\mathrm{Re}\,4\int_0^{b_2}\int_0^{a_2}\mathbf{E}\times\mathbf{H}^*\cdot\hat{z}\,dx\,dy \tag{5.1}$$

$$= 2\mathrm{Re}\int_0^{b_2}\int_0^{a_2}(E_xH_y^* - E_yH_x^*)\,dx\,dy \tag{5.2}$$

where * denotes a complex conjugate.

If the dissipation in the walls and dielectric is sufficiently small, the fields within the waveguide will be almost the same as the lossless case. This allows both types of loss to be estimated from the lossless fields using the perturbation method. The following subsections give expressions for the attenuation coefficient and the associated dielectric and shield wall loss for the rectangular shielded dielectric rod waveguide adapted from those of popular texts (Balanis, 1988) (Pozar, 1998):

5.2.1 Attenuation Coefficient

From Balanis (1988, p. 377) the attenuation coefficient per unit length (Np/m) can be written as:

$$\alpha = \frac{P_l}{2P_0} = \frac{P_d + P_w}{2P_0} = \alpha_d + \alpha_w \tag{5.3}$$

where P_d and P_w are the dielectric loss and shield wall loss respectively per unit length and α_d and α_w are the respective attenuation coefficients.

In practice conductor loss is increased by surface roughness, and this is normally taken into account by multiplying the theoretical value of the surface resistance by a roughness factor (Morgan, 1949).

5.2.2 Dielectric Loss

From Poynting's theorem the dielectric power loss for the full cross-section per unit length (Pozar, 1998, p. 61) can be written as:

$$P_d = \frac{\omega \varepsilon^{''} \varepsilon_o}{2} 4 \int_0^{b_1} \int_0^{a_1} |\mathbf{E}(x,y,z)|^2 \, dx \, dy \tag{5.4}$$

$$= \omega \varepsilon^{''} \varepsilon_o \, 2 \int_0^{b_1} \int_0^{a_1} (E_y E_y^* + E_x E_x^* + E_z E_z^*) \, dx \, dy \tag{5.5}$$

with

$$\varepsilon^{''} = \varepsilon^{'} \tan \delta$$

where ε_o is the permittivity of free space, $\varepsilon^{''}$ is the dielectric loss factor, $\varepsilon^{'}$ is the real part of the dielectric relative permittivity ε_{r2} in region II_2 and $\tan \delta$ is the dielectric loss tangent.

5.2.3 Shield Wall Loss

The conductor loss per unit length in the shield walls of a rectangular waveguide (Pozar, 1998, pp.38,125) can be written as:

$$P_w = \frac{1}{2} R_S \int_C |\mathbf{J}_s|^2 dl \tag{5.6}$$

$$= \frac{1}{2} R_S \int_C |\mathbf{H}_{\tan}|^2 dl \tag{5.7}$$

and

$$R_S = \sqrt{\frac{\omega \mu_o}{2\sigma}}$$

where $\bar{J}_s$ is the surface current density in the walls, $\bar{H}_{tan}$ is the magnetic field tangential to them, R_S is the wall surface resistance, μ_o is the permeability of free space, and σ is the conductivity of the wall material. Integration contour C encloses the interior cross-section perimeter of the guide walls.

Using equation (5.7) an equation for the loss per unit length of the top and right hand side walls for the full cross-section of the rectangular dielectric waveguide can then be found to be:

$$P_w = \frac{1}{2} R_S \, 4 \, (\int_0^{a_2} |\mathbf{H}^{(t)}(x,z)|^2 \, dx + \int_0^{b_2} |\mathbf{H}^{(s)}(y,z)|^2 \, dy) \tag{5.8}$$

$$= R_S \, 2 \, (\int_0^{a_2} (H_x^{(t)} H_x^{*(t)} + H_z^{(t)} H_z^{*(t)}) \, dx + \int_0^{b_2} (H_y^{(s)} H_y^{*(s)} + H_z^{(s)} H_z^{*(s)}) \, dy) \tag{5.9}$$

where superscripts t and s denote field components that are tangential to the top or right hand side walls respectively.

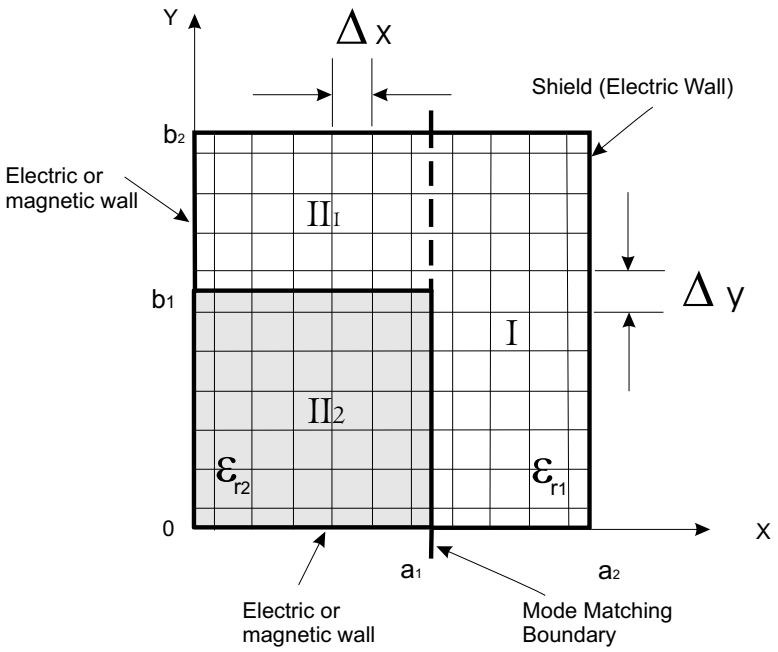

Figure 5.3: One quadrant of the cross-section, showing grid for power loss calculation.

5.3 Calculating the Attenuation Coefficient Using Mode Matching

The modes supported by a rectangular shielded dielectric rod waveguide were investigated using mode matching in Chapter 4, and this work has been reported in a recent paper (Wells & Ball, 2005*b*). The cross-section was divided into three separate regions, and the field within each region represented as a sum of basis functions particular to the region. Because of symmetry, it was only necessary to consider one quadrant of the cross-section, for which the mode matching regions are as shown in Figure 5.2. Continuity of the tangential fields was then enforced at the boundaries between the regions, allowing the amplitudes of the basis functions to be determined. Once this has been accomplished, the field components of any required mode can be calculated at any point in the cross-section.

To calculate the power losses within the waveguide, the cross-section is overlaid with a grid with lines spaced at $\triangle x$ and $\triangle y$, as illustrated in Figure 5.3. Field values and

power densities are calculated at intersection of the grid lines, and the total power flow and power dissipation are found by numerical integration. The total power flow, for the full cross-section, can be found by writing equation (5.2) in Riemannn sum form as:

$$\begin{aligned} P_0 \simeq 2\,\mathrm{Re}(&\sum_{i=1}^{n}(E_{xI}^{(i)}H_{yI}^{*(i)} - E_{yI}^{(i)}H_{xI}^{*(i)}) \\ &+\sum_{j=1}^{m}(E_{xII1}^{(j)}H_{yII1}^{*(j)} - E_{yII1}^{(j)}H_{xII1}^{*(j)}) \\ &+\sum_{k=1}^{p}(E_{xII2}^{(k)}H_{yII2}^{*(k)} - E_{yII2}^{(k)}H_{yII2}^{*(k)})) \\ &\cdot \Delta x\,\Delta y \end{aligned} \tag{5.10}$$

where i, j, k identify the n, m and p nodes in regions I, II_1, II_2 respectively.

The dielectric power loss per unit length, for the full cross-section, is obtained from equation (5.5) as:

$$P_d \simeq 2\,\omega\varepsilon^{''}\varepsilon_o \sum_{k=1}^{p}(E_y^{(k)}E_y^{*(k)} + E_x^{(k)}E_x^{*(k)} + E_z^{(k)}E_z^{*(k)})\,\Delta x\,\Delta y \tag{5.11}$$

where the k index identifies p nodes in region II_2.

The conductor losses in the shield walls, for the full cross-section, are derived from equation (5.9) as:

$$\begin{aligned} P_w \;\simeq\; 2\,R_S(&\sum_{t=1}^{T}(H_x^{(t)}H_x^{*(t)} + H_z^{(t)}H_z^{*(t)})\Delta x \\ &+\sum_{s=1}^{S}(H_y^{(s)}H_y^{*(s)} + H_z^{(s)}H_z^{*(s)})\Delta y) \end{aligned} \tag{5.12}$$

where t identifies T nodes, on the top shield boundary ($0 \le x \le a_2$, $y = b_2$) spaced Δx and index s identifies S nodes, on the right hand side shield boundary ($0 \le y \le b_2$, $x = a_2$) with spacing Δy. Also in equations (5.10), (5.11) and (5.12) each component of $\mathbf{E}$ or $\mathbf{H}$, at a point, is the sum of a number of basis function values calculated using the MSW method at that point.

By substituting the field component values at each grid point into these equations, a close approximation of the power flow and losses can be obtained for the structure. Since equations (5.10), (5.11) and (5.12) are obtained from four times the quarter structure of Figure 5.3 duplication of any common points at the boundaries must be taken into account. Equation (5.3) can then be used to find the attenuation coefficient due to dielectric loss, shield wall loss or total loss.

5.4 Alternative Method - Attenuation Coefficient due to Dielectric Loss

Another way of calculating the attenuation due to dielectric loss α_d only is to calculate it directly using the MSW method. In this procedure the lossless propagation coefficient β_z is calculated first. The loss factor ε'', is then determined from the loss tangent, and included to give a complex permittivity of the dielectric. The program can then be run again using a range of complex propagation coefficients γ_z . These consist of the lossless β_z and a range of α_z values. A value of α_d is then determined by finding that value of α_z for which the determinant of the mode-matching equation matrix is closest to zero. This would normally be the start of an iterative process in which α_d and β_z are varied alternatively until the propagation coefficient converges to a value of sufficient accuracy. It was found however, that during the iterative procedure, the variation in β_z was insignificant and so only the initial lossless β_z was required.

The perturbation method using the grid is preferred to the above direct method as it can be used to find both shield wall loss and dielectric loss. Also it is much faster to compute. However, since fields from the lossless solution are used to estimate the dissipation, some additional error is involved. In section 5.5.2, dielectric loss results obtained by both methods are compared, to show that the additional error cost of the perturbation approximation is negligible.

Typical determinant value verses attenuation coefficient data, from the computer pro-

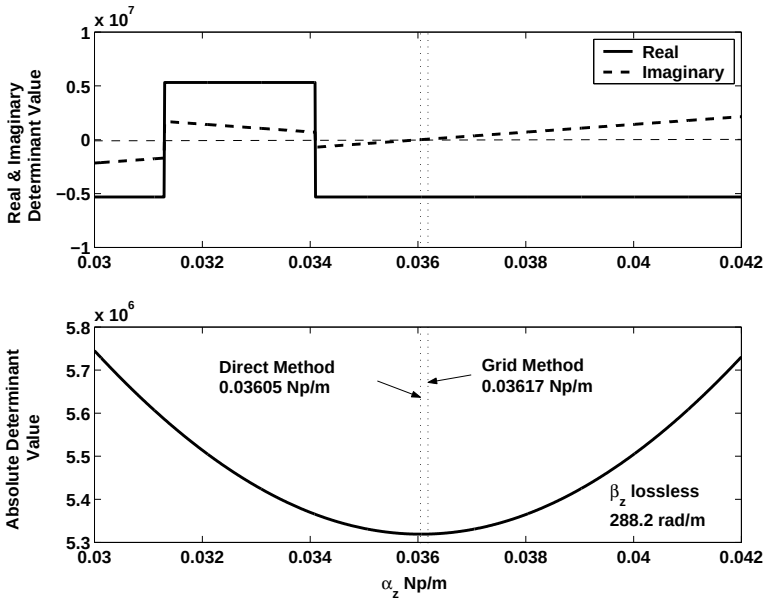

Figure 5.4: Determinant value verses the attenuation coefficient α_z. The best approximation to the direct method eigenvalue occurs at the minimum of the absolute value of the determinate. The mode is E_{11}^y from EO symmetry, $a_1 = b_1 =$ 6.025mm, the shield-to-dielectric dimension ratio $SDDR = a_2/a_1 = 2$, Frequency =3.4GHz, β_z lossless=288.2 rad/m.

gram used, is shown in Figure 5.4. The upper sub plot shows the real and imaginary values of the determinant and the lower the absolute value. The best approximation to the attenuation coefficient eigenvalue occurs at the minimum absolute value of the determinant, ie when the real and imaginary determinant values are closest to zero at the same time. The figure also shows a comparison between a direct method result and one using the grid method with a 201x201 grid size. The difference in the values is within 0.5%. Detailed results from this direct method are presented in section 5.5.2 to help validate the grid method. More detail concerning the programming of the direct method can be found in section 4.5.1.

5.5 Discussion of Calculated Results

5.5.1 Attenuation Coefficient Calculations

The resultant attenuation coefficients created by the dissipation within the dielectric and shield walls were calculated for the E_{11}^y mode and E_{21}^x/E_{12}^y coupled mode using the grid method described in section 5.3. The dielectric rod material is barium tetratitinate, for which the loss tangent is specified by the manufacturer (picoFarad$^{\text{TM}}$) as:

$$\tan\delta = \text{Frequency(GHz)}/3 \times 10^4 \tag{5.13}$$

This material was also used to obtain the experimental results presented later. A surface roughness factor of unity has been assumed for the metal shield.

The attenuation coefficient verses frequency (beginning near cutoff) with a shield-to-dielectric dimension ratio, $SDDR = a_2/a_1 = 2$, is shown in Figures 5.5 and 5.6 for the E_{11}^y mode and the E_{21}^x/E_{12}^y coupled mode respectively. The rise in α at the higher frequencies in the figures is due to the natural increase in the loss tangent with frequency.

Also the graphs of attenuation coefficient verses $SDDR$ with the frequency at 3.4GHz is shown in Figures 5.7 and 5.8 for the E_{11}^y mode and E_{21}^x/E_{12}^y coupled mode respectively. For the E_{11}^y mode shown in Figure 5.7, as shield size increases relative to the dielectric, α_w is gradually dominated by a relatively constant α_d. This indicates that when using the above dielectric with a relative permittivity of around 37, choosing an $SDDR > 2$, will minimise the effect of the shield conductor loss. However a similar structure with a dielectric that has a lower loss tangent would benefit, in better overall loss, if the shield was positioned further from the dielectric. Another observation from Figure 5.7 is that for α_w to equal α_d the shield has to be relatively close to the dielectric with an $SDDR$ of about 1.16.

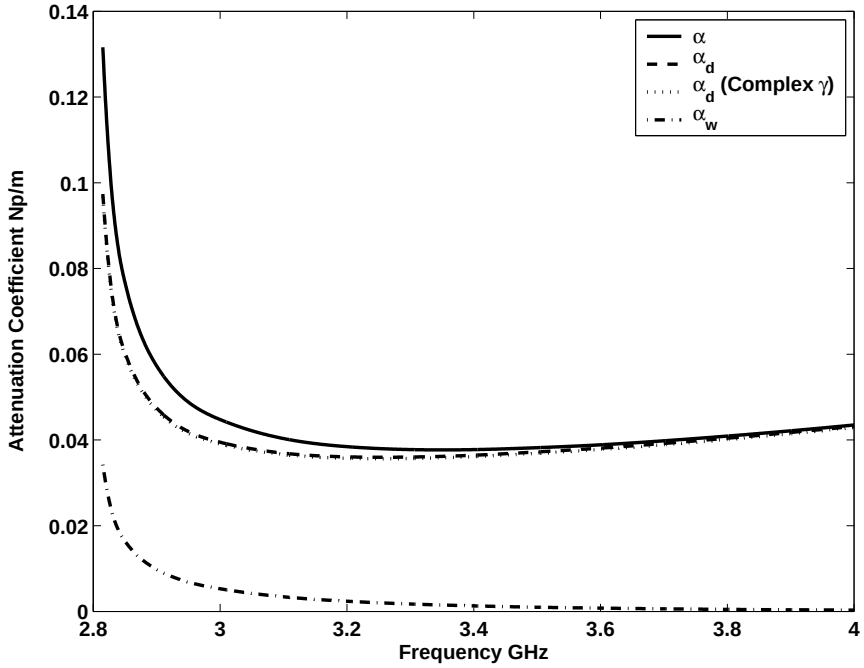

Figure 5.5: Attenuation coefficient versus frequency for the E_{11}^y mode. The shield-to-dielectric dimension ratio $SDDR = a_2/a_1 = 2$.

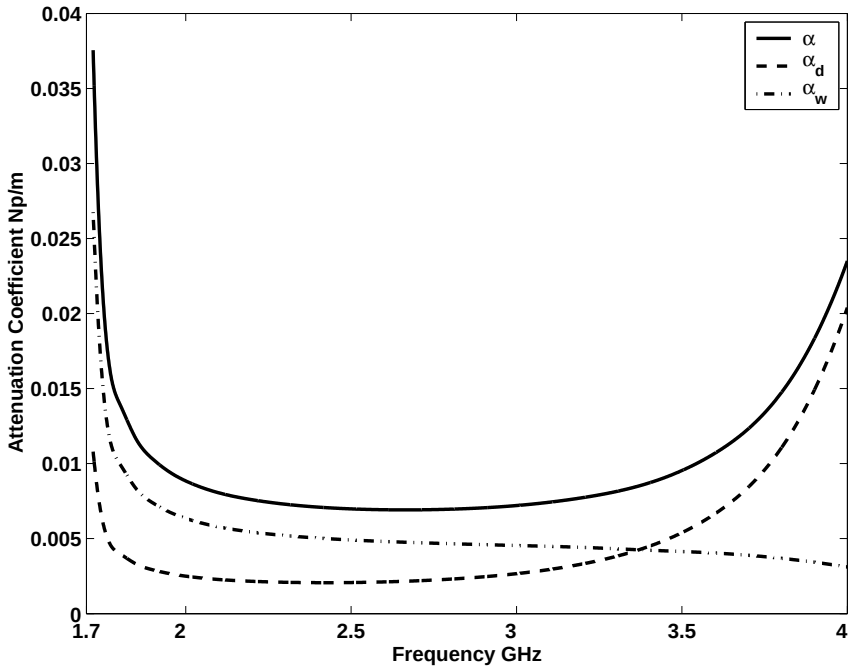

Figure 5.6: Attenuation coefficient versus frequency for the E_{21}^x/E_{12}^y coupled mode. The shield-to-dielectric dimension ratio $SDDR = a_2/a_1 = 2$.

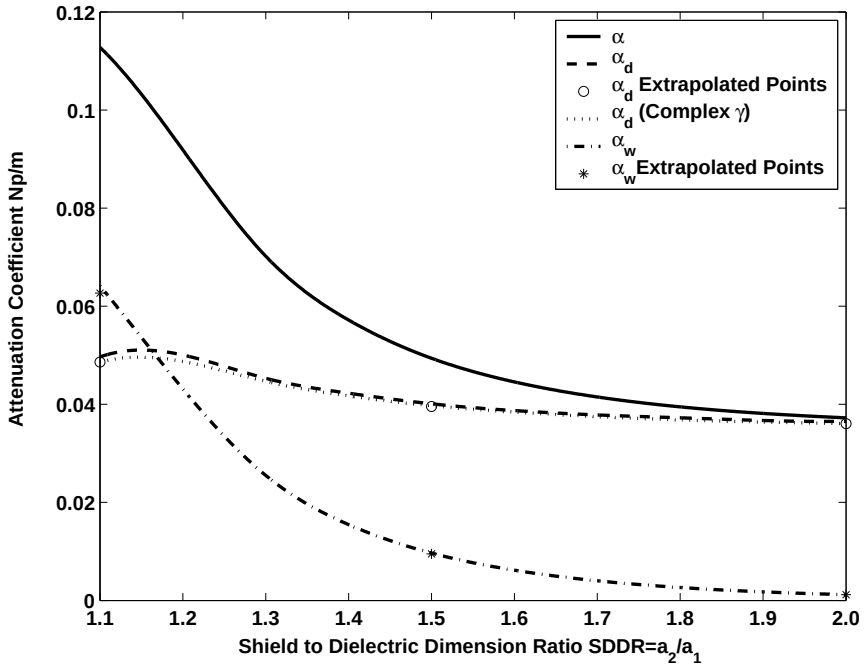

Figure 5.7: Attenuation coefficient versus dielectric to shield dimension ratio for the E_{11}^y mode. The frequency is 3.4GHz.

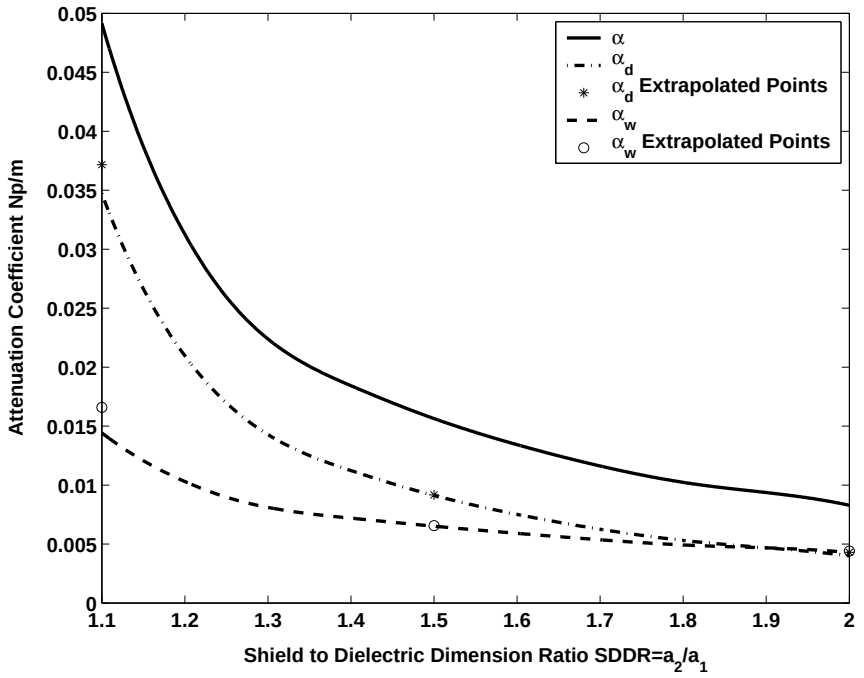

Figure 5.8: Attenuation coefficient versus dielectric to shield dimension ratio for the coupled E_{21}^x/E_{12}^y. The frequency is 3.4GHz.

It is interesting to note, from all the figures, that the attenuation coefficient is appreciably lower for the E_{21}^x/E_{12}^y coupled mode compared to the E_{11}^y mode owing to its lower dielectric loss while maintaining a relatively low shield wall conduction loss. This is due to the smaller intensity of the electric field in the dielectric compared to the air region for this mode, which is revealed when the field pattern is plotted as in Figure 5.10. In the figure the field intensity of the electric field has had to be increased artificially by 5 so that the dielectric field could be shown effectively at the same time as the larger intensity of the air region.

The size of grid used in these plots was 51x51 points for one quarter of the structure. The values marked with 'o' and '*' on the plots are generated from an extrapolation of the convergence of the attenuation coefficient with increase in grid size. The maximum grid used in this convergence process was 501x501 which took a number of hours to compute with a 1.6GHz P.C. The comparison of these values show that a grid size of 51x51 (only minutes to compute) gave results that are within 2% of those obtained with the 501x501 grid for $SDDR$s at 1.5 and 2. Hence the smaller grid size should give sufficient convergence to a solution for $SDDR$s down to about 1.3. Below this, larger grid sizes are required as the differences in results for $SDDR$ at 1.1 can approach 13% for some modes. This can be seen in Figure 5.8 for this $SDDR$ where the differences between the values for attenuation due to wall and dielectric loss, for the coupled E_{21}^x/E_{12}^y mode, are 6.5% and 12.9% respectively.

The grid size of 51x51 will be used in section 5.7 where the grid method accuracy was validated by using the results from it to calculate the Q of a rectangular shielded dielectric line (used as a resonator) and compared to measured Q values.

5.5.2 Comparison of the Grid Method and Direct Method to Calculate α_d

To estimate the the extra error due to the perturbation approximation which is inherent in the grid method α_d of the E_{11}^y mode was also calculated directly using the modified

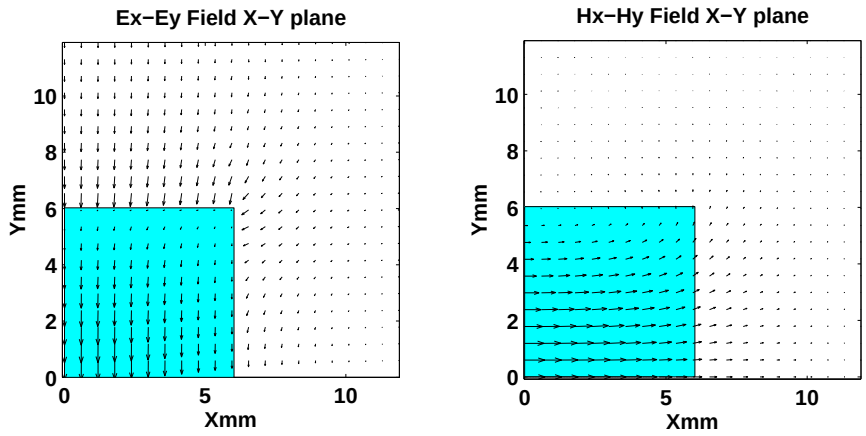

Figure 5.9: Electric and magnetic field patterns in the x-y plane for the E_{11}^{y} mode for quarter of the structure.

Solbach and Wolff (MSW) method as described in section 5.4. The results are shown in Figures 5.5 and 5.7, and agree closely with the grid method values. The maximum difference in α_d between the grid (51x51 points) and direct methods is 0.7% and 2.9% in Figures 5.5 and 5.7 respectively. However the extrapolated points from the grid method (501x501 points), of Figure 5.7, are within 0.025% of the direct method values at the same $SDDR$.

5.5.3 Calculated Values Compared to those Obtained Analytically

As $SDDR \Rightarrow 1$, the E_{11}^{y} mode becomes TE_{10} and the E_{21}^{x}/E_{12}^{y} coupled modes become the TM_{11} mode. The TE_{10} and TM_{11} like qualities of these modes, in a cross-section of the dielectric region, can be seen in figures 5.9 and 5.10 respectively. For the TE_{10} mode in rectangular waveguide the electric field vectors in the x-y plane are the result of the E_y component and have one half wave variation across the waveguide in the x direction only. The electric field in the dielectric rod is similar but does have some y variation. This y variation gradually disappears as the shield is brought closer to the rod. The electric field vectors in the x-y plane of the TM_{11} mode, in rectangular waveguide, is the result of the superposition of E_x and E_y components giving a radial pattern. The components each have one half wave variation across the waveguide.

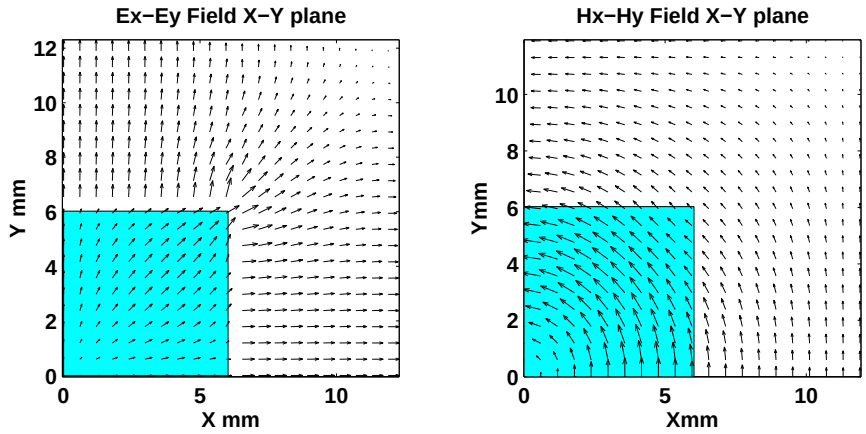

Figure 5.10: Electric and magnetic field patterns in the x-y plane for the coupled E^x_{21}/E^y_{12} modes for quarter of the structure.

differences at the dielectric rod edges. Again this gradually disappears as the shield is brought closer to the rod. For both modes the magnetic field vectors in the x-y plane are perpendicular to the electric field vectors.

A further check of the grid method was performed by calculating analytically, good approximations of α_w and α_d for a square cross-section waveguide homogeneously filled with dielectric. These were compared to those obtained from the grid method as the SDDR value is brought very close to 1. From Pozar (1998, p. 125) the attenuation due to wall loss for the TE_{10} mode in rectangular waveguide can be calculated analytically from:

$$\alpha^h_w = \frac{P^h_w}{2P^h_{10}} = \frac{2\pi^2 R_s[b + a/2 + (\beta_z^2 a^3)/2\pi^2]}{\omega\mu a^3 b\beta_z} \tag{5.14}$$

and (5.15)

$$\beta_z = \sqrt{\beta_0^2 - (m\pi/a)^2} \tag{5.16}$$

where $a = b = 2a_2 = 2b_2$ in this case, P^h_{10} and P^h_w are the time average power for the TE_{10} mode and the power dissipated in the waveguide walls respectively and superscript h stands for TE. The expressions for P^h_{10} and P^h_w are the same as equations 5.1 and 5.7.

Similarly using the method described by Pozar the attenuation due to dissipation in

the walls for the TM_{11} mode can be found from:

$$P_{11}^e = |A_{11}^e|^2 \, 1/16 \, R_e \, \frac{\beta_z \omega \varepsilon_0 \varepsilon_r a^4}{\pi^2} \tag{5.17}$$

$$P_w^e = |A_{11}^e|^2 \, R_s/4 \, \left(\frac{\omega \varepsilon_0 \varepsilon_r}{\pi}\right)^2 a^3 \tag{5.18}$$

and then:

$$\alpha_w^e = \frac{P_w^e}{2P_{11}^e} = 2R_s \frac{\omega \varepsilon_0 \varepsilon_r}{\beta_z a} \tag{5.19}$$

and (5.20)

$$\beta_z = \sqrt{\beta_0^2 - (\pi/a)^2 - (\pi/b)^2} \tag{5.21}$$

where superscript e stands for TM and A_{11}^e is an unknown coefficient.
From Pozar (1998, p. 111) the attenuation coefficient due to dielectric loss in a homogeneously filled rectangular waveguide for both TE and TM modes can be found from:

$$\alpha_d = \frac{\omega^2 \mu_0 \varepsilon_0 \varepsilon_r \tan \delta}{2\beta_z} \tag{5.22}$$

where β_z will be specific to the type of mode.

To obtain the best accuracy the grid method values, as mentioned before, were obtained from an extrapolation of the convergence of the attenuation coefficient with increase in grid size. The results of the extrapolation are shown in Figures 5.11 and 5.12 and are summarised in table 5.1. The analytically obtained values and those from the grid method show a difference of less than 2%. The dimensions of the waveguide used were the same as the dielectric rod used in experimental measurement, ie a 12.05mm square cross-section, $\varepsilon_r = 37.13$, a frequency of 3.4GHz and with $\tan \delta$ calculated for the dielectric at that frequency. The maximum grid size used was 501 x 501.

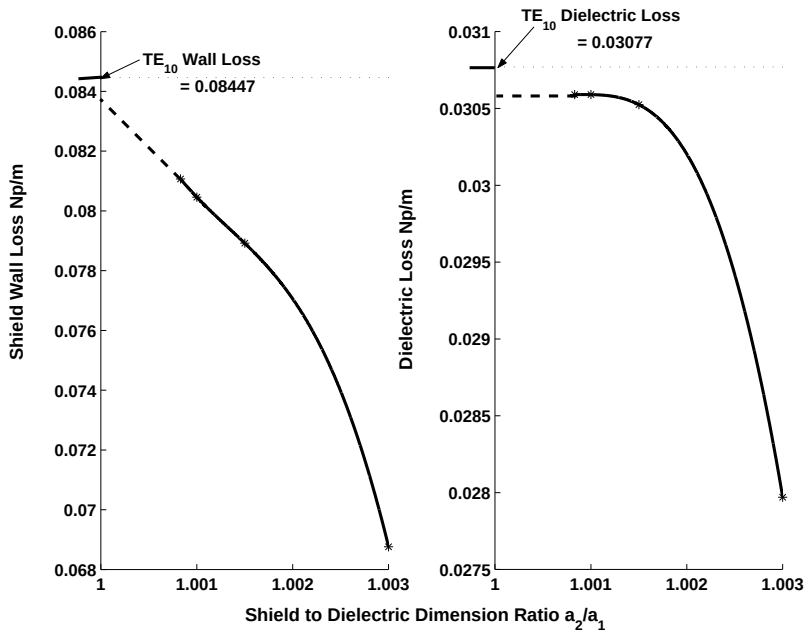

Figure 5.11: Extrapolation of the grid method, wall and dielectric loss values to $SDDR = 1$. Comparison is made with those calculated for the TE_{10} mode in dielectric filled rectangular waveguide using an analytical method.

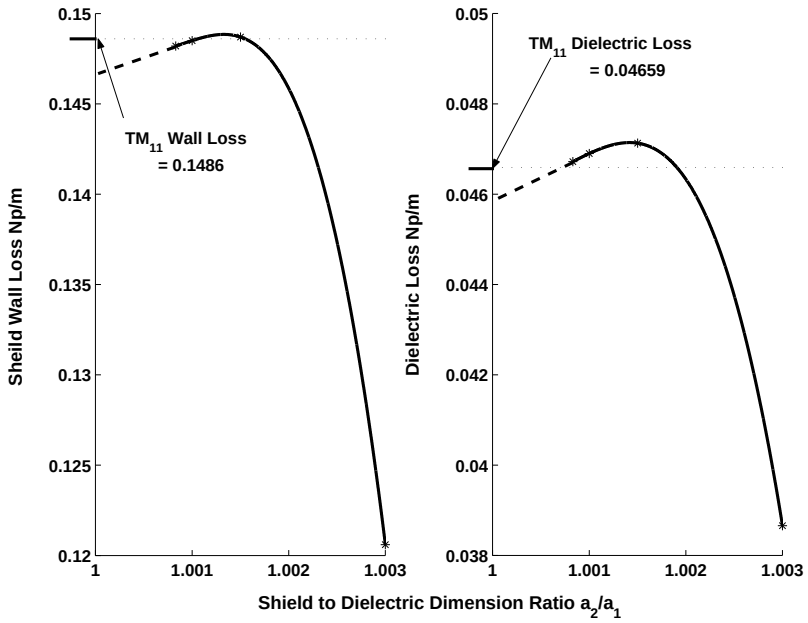

Figure 5.12: Extrapolation of the grid method, wall and dielectric loss values to $SDDR = 1$. Comparison is made with those calculated for the TM_{11} mode in dielectric filled rectangular waveguide using an analytical method.

Table 5.1: Comparison of extrapolated grid method attenuation coefficient results (Np/m) for the shielded rectangular dielectric waveguide, at SDDR=1, and those calculated for dielectric filled rectangular waveguide ($a_1 = b_2 = 6.025\text{mm}, \varepsilon_{r2} = 37.13$, Frequency = 3.4GHz).

	TE_{10}	E_{11}^y Grid Method	%
α_w	0.08447	0.0837	-0.9
α_d	0.03077	0.0306	-0.6
	TM_{11}	E_{21}^x/E_{12}^y Grid Method	%
α_w	0.1486	0.147	-1.1
α_d	0.04659	0.0458	-1.7

5.6 Measurement Technique

To verify the grid mode matching method for finding loss, two comparisons of calculated and measured unloaded Q were made using different types of shielded dielectric resonator.

The first set of measurements were made using the E_{11}^y mode and two sizes of square cross-section shield around the dielectric resonator. The resonators consisted of a square cross-section barium tetratitanate dielectric rod (12.05 x 12.05mm) placed in a square cross-section brass waveguide of the same length L (153.3mm). To facilitate accurate machining, the brass waveguides was made in two 'U' shaped cross-sectional halves and bolted together. Brass end plates were added to the ends of the waveguide, and in contact with ends of the rod, to form the resonators. Measurements of the reflection coefficient were made using a vector network analyzer that was lightly coupled to the resonators by a probe mounted at the mid-point, as in Figure 5.13. To provide consistent results the same dielectric rod was actually used in both resonators. The waveguide cross-sections were 23.8 x 23.8mm and 18 x 18mm, giving $SDDR$ values of 1.98 and 1.49 respectively.

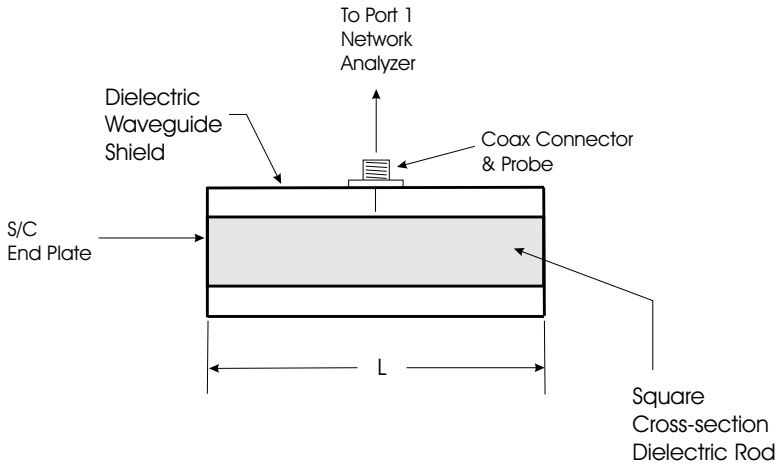

Figure 5.13: Set up of the dielectric resonator used for the measurement of unloaded Q.

The second set of measurements using the E_{11}^{y} and E_{11}^{x} modes were made with a similar resonator consisting of a square cross-section barium tetratitanate dielectric rod (12.05 x 12.05mm) and 85mm long but this time placed in a copper walled WR159 waveguide of the same length as the rod. Again brass end plates were added to the ends of the waveguide, and in contact with ends of the rod, to form the resonator. Measurements on this type of resonator were performed because the rectangular cross-section of the WR159 waveguide shielded allows the E_{11}^{y} and E_{11}^{x} modes to become non degenerate over part of the frequency range which was not the case in the first measurement arrangement. This variation in degeneracy can be seen by comparing the mode charts of the square cross-section resonators (Figures 5.14 and 5.15) with that of the WR159 shielded type (Figure 5.18).

The calculation of unloaded Q was carried out using a least squares fit to the measured reflection coefficient data. The method is the result of work carried out by Associate Professor Jim Ball at the Faculty of Engineering and Surveying, University of Southern Queensland (USQ), Queensland, Australia and is described in Appendix C.

The unloaded Q of a resonator can be calculated from:

$$Q = \frac{\omega_0 W}{P_{Cd} + P_{Cw} + P_e} \tag{5.23}$$

where ω_0 is the frequency at resonance, W is four times the energy stored in the three

regions of Figure4.2 over the resonator length, and P_{Cd}, P_{Cw} and P_e are the dielectric, wall and end plate losses respectively.

With reference to Balanis (1988, p. 390), the total energy stored in the resonator over the full cross-section can be calculated from:

$$W = \frac{\varepsilon_0}{2} 4 \int_0^L \int_0^{b_2} \int_0^{a_2} \varepsilon'(\mathbf{E} \cdot \mathbf{E}^*) dx\, dy\, dz \tag{5.24}$$

and the propagation coefficient will be:

$$\beta_z = \frac{N\pi}{L} \tag{5.25}$$

where N is the number of half wavelengths of the resonant mode under investigation. Furthermore the z variation of the components of $\mathbf{E}$ in this type of resonator will be of the form $\sin \beta_z z$ or $\cos \beta_z z$ and their amplitude will be twice that of unidirectional waveguide propagation. After integration with respect to z equation (5.24) be written as:

$$W = L\varepsilon_0 4 \int_0^{b_2} \int_0^{a_2} \varepsilon'(\mathbf{e} \cdot \mathbf{e}^*) dx\, dy \tag{5.26}$$

where $\mathbf{e}$ is a function of the transverse coordinates only. In Reimann sum form:

$$\begin{aligned} W \simeq\ & 4L\varepsilon_0 \Big(\sum_{i=1}^{I} (e_{xI}^{(i)} e_{xI}^{*(i)} + e_{yI}^{(i)} e_{yI}^{*(i)} + e_{zI}^{(i)} e_{zI}^{*(i)}) \\ & + \sum_{i=1}^{I} (e_{xII1}^{(i)} e_{xII1}^{*(i)} + e_{yII1}^{(i)} e_{yII1}^{*(i)} + e_{zII1}^{(i)} e_{zII1}^{*(i)}) \\ & + \varepsilon' \sum_{i=1}^{I} (e_{xII2}^{(i)} e_{xII2}^{*(i)} + e_{yII2}^{(i)} e_{yII2}^{*(i)} + e_{zII2}^{(i)} e_{zII2}^{*(i)})\Big) \\ & \cdot \Delta x\, \Delta y \end{aligned} \tag{5.27}$$

where i, j and k identify the n, m and p nodes in regions I, II_1, II_2 respectively. Alternatively, the energy stored in the cavity may be obtained from the power flow in the infinite waveguide (5.10):

$$W = \frac{2LP_0}{v_g} \tag{5.28}$$

where v_g is the group velocity, obtainable numerically.

Similarly, over the full cross-section, equation (5.11) for the dielectric loss P_d of dielectric waveguide per unit length will become:

$$P_{Cd} \simeq 4\omega\varepsilon^{''}\varepsilon_o L \sum_{i=1}^{I} (e_y^{(i)} e_y^{*(i)} + e_x^{(i)} e_x^{*(i)} + e_z^{(i)} e_z^{*(i)})\, \Delta x\, \Delta y \tag{5.29}$$

which is equivalent to:

$$P_{Cd} = 2LP_d \tag{5.30}$$

Wall Loss P_w from equation (5.12) for the full cross-section per unit length will become:

$$\begin{aligned} P_{Cw} \quad \simeq \quad & 4R_S L(\sum_{t=1}^{T} (h_x^{(t)} h_x^{*(t)} + h_z^{(t)} h_z^{*(t)})\Delta x \\ & + \sum_{s=1}^{S} (h_y^{(s)} h_y^{*(s)} + h_z^{(s)} h_z^{*(s)})\Delta y) \end{aligned} \tag{5.31}$$

which is equivalent to:

$$P_{Cw} = 2LP_w \tag{5.32}$$

The end plate loss, for both ends over the full cross-section of the resonator, can be calculated from:

$$P_e = 16R_s \int_0^{b_2} \int_0^{a_2} |\mathbf{h}_t|^2 dxdy \tag{5.33}$$

which becomes in Reimann sum form:

$$P_e \simeq 16R_s \sum_{i=1}^{I} (h_x^{(i)} h_x^{*(i)} + h_y^{(i)} h_y^{*(i)})\, \Delta x\, \Delta y \tag{5.34}$$

5.7 Comparison of Calculated and Measured Results

5.7.1 Square Cross-section Shielded Resonators

The reflection coefficient values for resonances of the E_{11}^y mode were measured over a frequency range from cut-off to 4.2GHz. When comparing the measured Q factor results

Table 5.2: Comparison of calculated and measured Q values for the 153.3mm long square cross-section dielectric rod resonator at N half wavelengths ($a_1 = b_1 =$ 6.025mm, $a_2 = b_2 = 11.9$mm & 9mm).

SDDR (a_2/a_1)	N	Measured Frequency (GHz)	Measured Unloaded Q	Calculated Unloaded Q	% Q Diff.
1.49	7	2.9731	3420	3373	-1.4
	8	2.9973	3793	3589	-5.8
	17	3.7589	5095	4924	-3.5
	20	4.1135	4702	4927	+4.6
1.98	7	2.8371	5092	5079	-0.3
	13	3.2907	5278	5743	+8.1
	17	3.7313	5241	5507	+4.8
	18	3.8508	5224	5412	+3.5

to calculated values, it is necessary to account for surface roughness. The average surface roughness due to the milling process was estimated as 3.2 micrometers. Given that the shield material is brass containing 38% zinc with a conductivity of 1.57×10^7 ohm.m, a surface roughness factor of about 1.7 is predicted from (Morgan, 1949). The method used in Morgan (1949) assumes that the surface profile shows a regular variation e.g. a sawtooth. The actual surface profile is likely to be more complicated than this. Therefore a surface roughness factor of 2 was used to calculate the Q factor values. A comparison of measured and calculated values is shown in Table 5.2. Percentage differences of the measured values with respect to the calculated values are shown in the right hand column. From this it can be seen that on average the measured Q factor values are too low by about 5%. The most probable reason for this is the flange contact resistance of the short circuit end plates (Somlo, 1979) which were bolted on, not soldered. The join between the brass waveguide halves (again bolted on not soldered) could also cause some loss due to the H_z components of the hybrid modes. These components will create perpendicular surface currents that will have to pass through the contact resistance of the join.

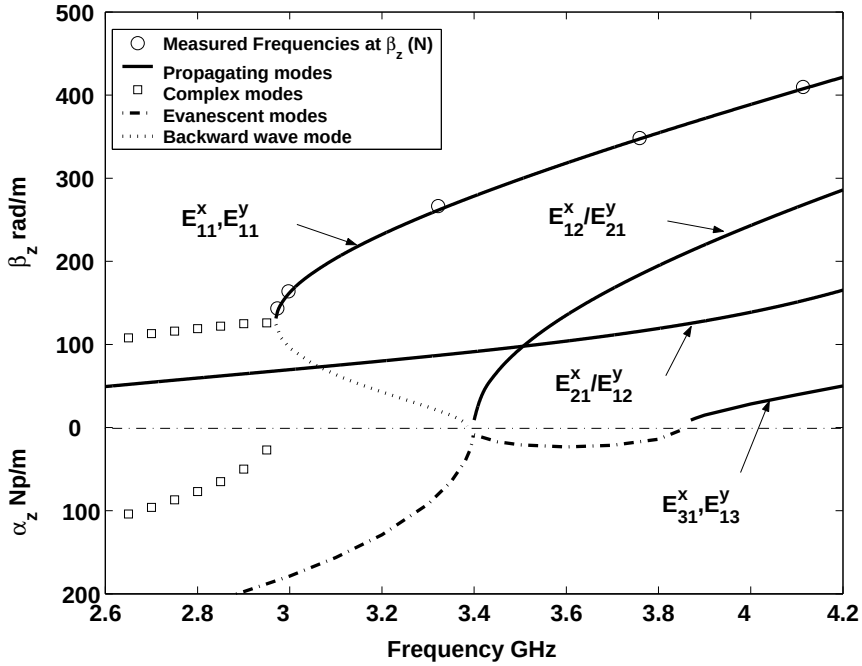

Figure 5.14: Calculated and measured propagation coefficient values for the first few modes to propagate, shield-to-dielectric dimension ratio $SDDR = 1.49$.

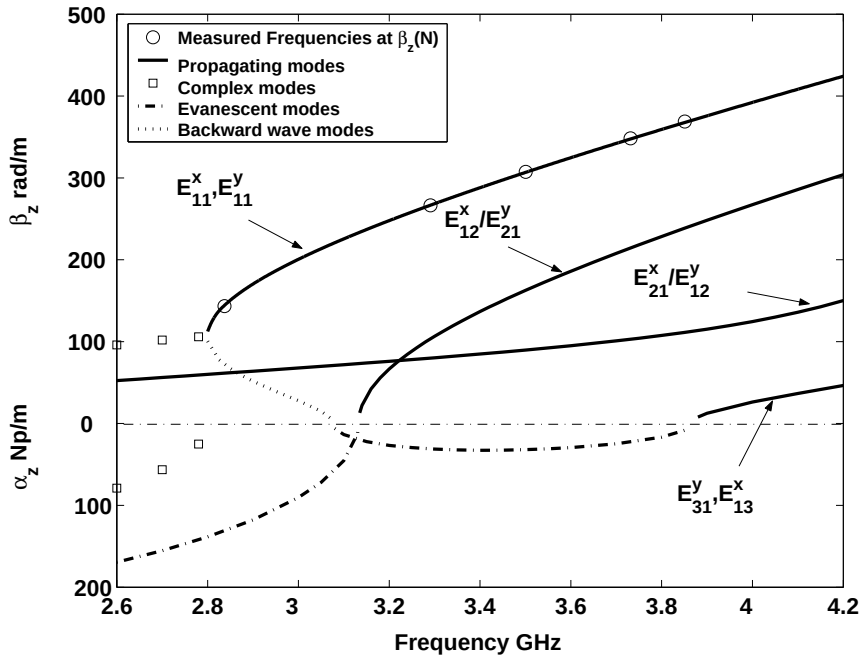

Figure 5.15: Calculated and measured propagation coefficient values for the first few modes to propagate, shield-to-dielectric dimension ratio $SDDR = 1.98$.

Not all possible resonances were able to be measured. It was found that some resonances did not couple well to the probe and so were too noisy. Other resonances were found to be affected by significant coupling to the degenerate mode E_{11}^x which made accurate unloaded Q calculations impossible at these frequencies.

Mode charts for the first few modes to propagate are shown in Figures 5.14 and 5.15 for SDDRs of 1.49 and 1.98 respectively. The 'o' points show the propagation coefficients from (5.25) plotted against the measured frequencies of the resonances, so that comparison with calculation can be made. The differences between measured and calculated frequencies at the same N propagation values are less than 1% for both resonators.

5.7.2 WR159 Waveguide Shielded Resonator

The reflection coefficient values for resonances of the E_{11}^y and E_{11}^x modes were measured over a frequency range from 2.4 to 4GHz. In this resonator the inside walls of the waveguides and end plates were highly polished and so the surface roughness could be considered to be very low. The shield wall material is copper (conductivity 5.813×10^7 ohm.m) and the end plates are brass containing 38% zinc (conductivity of 1.57×10^7 ohm.m). A comparison of measured and calculated values is shown in Table 5.3. Percentage differences of the measured values with respect to the calculated values are shown in the right hand column. This result is also shown graphically in Figure 5.16.

The figure shows good correlation between the measured points and corresponding calculated values illustrated by the least squares 2nd order polynomial fit to the measured points.

A break up of the calculated Q due to dielectric loss Q_d, end plate loss Q_e and shield wall loss Q_w can be seen in Figure 5.17.

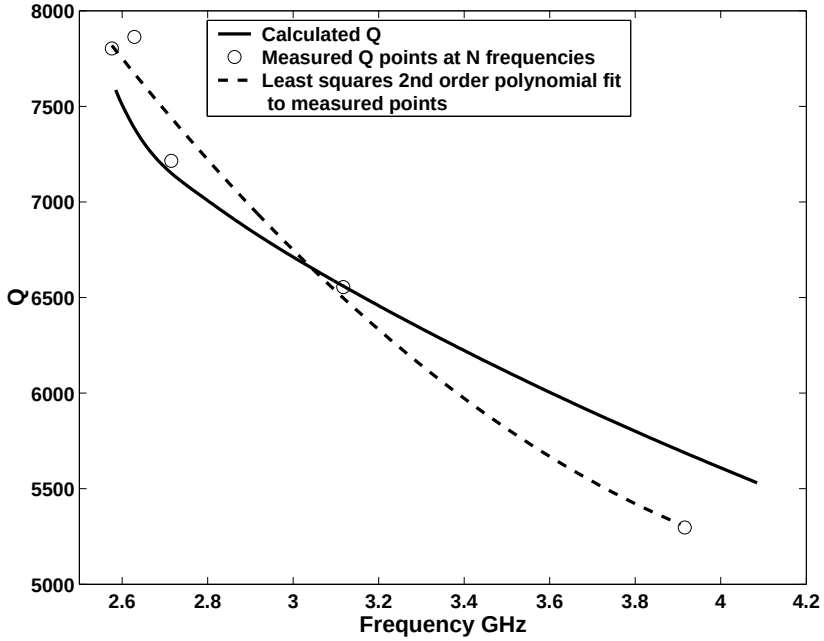

Figure 5.16: Calculated and measured Q factor of the E_{11}^y mode for the 85mm long, WR159 shielded, square cross-section dielectric rod resonator. Dimensions: $a_1 = b_1 = 6.025$mm, $a_2 = 20.1$mm, $b_2 = 10.045$mm.

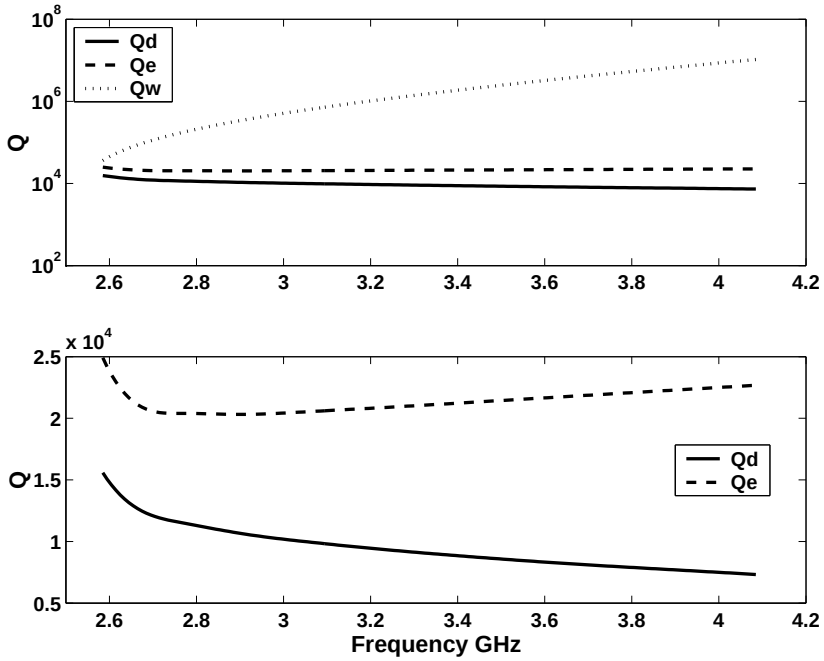

Figure 5.17: Break up of the calculated Q factor components of the E_{11}^y mode for 85mm long, WR159 shielded, square cross-section dielectric rod resonator. The upper graph shows all the Q components due to dielectric loss Q_d, end plate loss Q_e and shield wall loss Q_w. The lower magnified graph shows Q_d and Q_e only. Dimensions: $a_1 = b_1 = 6.025$mm, $a_2 = 20.1$mm, $b_2 = 10.045$mm.

Table 5.3: Comparison of calculated and measured Q values for the 85mm long, WR159 shielded, square cross-section dielectric rod resonator at N half wavelengths. Exact dimensions $a_1 = b_1 = 6.025$mm, $a_2 = 20.1$mm, $b_2 = 10.045$mm.

Mode Type	N	Measured Frequency (GHz)	Measured Unloaded Q	Calculated Unloaded Q	% Q Diff.
E_{11}^y	2	2.5785	7803	7640	-2.1
	3	2.6286	7863	7387	-6.4
	4	2.7150	7215	7160	-0.8
	6	3.1172	6555	6560	+0.1
	10	3.9159	5297	5688	+6.9
E_{11}^x	5	2.9620	6164	6217	+0.9
	6	3.0959	6435	6191	-3.9

The upper graph shows that, for the WR159 shielded, square cross-section dielectric rod resonator, the large Q_w will have little effect on the overall Q as it is swamped by the much lower Q_d and Q_e, ie the shield wall loss in this structure is much lower than the other losses. Similarly the lower graph, which excludes Q_w, shows that Q_d is the more dominant factor compared to Q_e. Therefore the gradual decrease in total Q, shown in Figure 5.16 for calculated and measured results, is due mostly to Q_d whose behaviour is caused by the natural increase in dielectric loss with increase in frequency. Furthermore the shape of the calculated Q curve in Figure 5.16 follows that of Q_d, and to a lesser extent Q_e, and hence a least squares polynomial fit to the measured points was considered appropriate.

The flange contact resistance of the end plates with the waveguide ends and the surface roughness of the inside wall and end plate surfaces do not appear to play a significant role in the result. This is thought to be due to the far superior machining of the commercial waveguide and the polished finish of the surfaces respectively.

Again with this structure not all possible resonances were able to be measured and it was found that some resonances did not couple well to the probe and so were too noisy or not found. Measurements and recognition of some desired resonances was also made

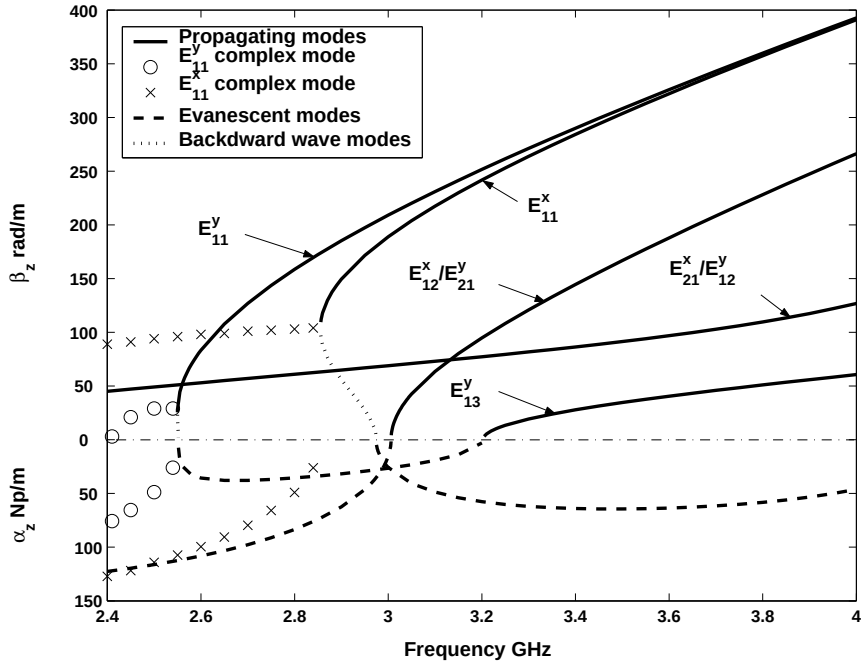

Figure 5.18: Calculated propagation coefficient values for the first few modes to propagate of a WR159 shielded, square cross-section dielectric rod waveguide. Dimensions: $a_1 = b_1 = 6.025$mm, $a_2 = 20.1$mm, $b_2 = 10.045$mm.

difficult by the close proximity of other resonances caused by the near degeneracy of the E_{11}^y and E_{11}^x modes and the congestion of other propagating modes at the higher frequency end of the measured band. A mode chart for the band of interest is shown in Figure 5.18 and reveals the reasonably large proliferation of propagating modes.

5.8 Computer Program to Calculate the Attenuation due to Losses and the Q Factor of the Test Resonator

The programing steps to find the attenuation due to dielectric and shield wall losses and the Q factor of test resonator of section 5.6 are shown in the flow chart of Figure 5.19. Before the program is run the propagation coefficient for the mode of interest in the structure and also the unknown coefficients of the basis functions have to be found. This procedure has already been described in section 4.5. The details of the flow chart of Figure 5.19 are as follows:

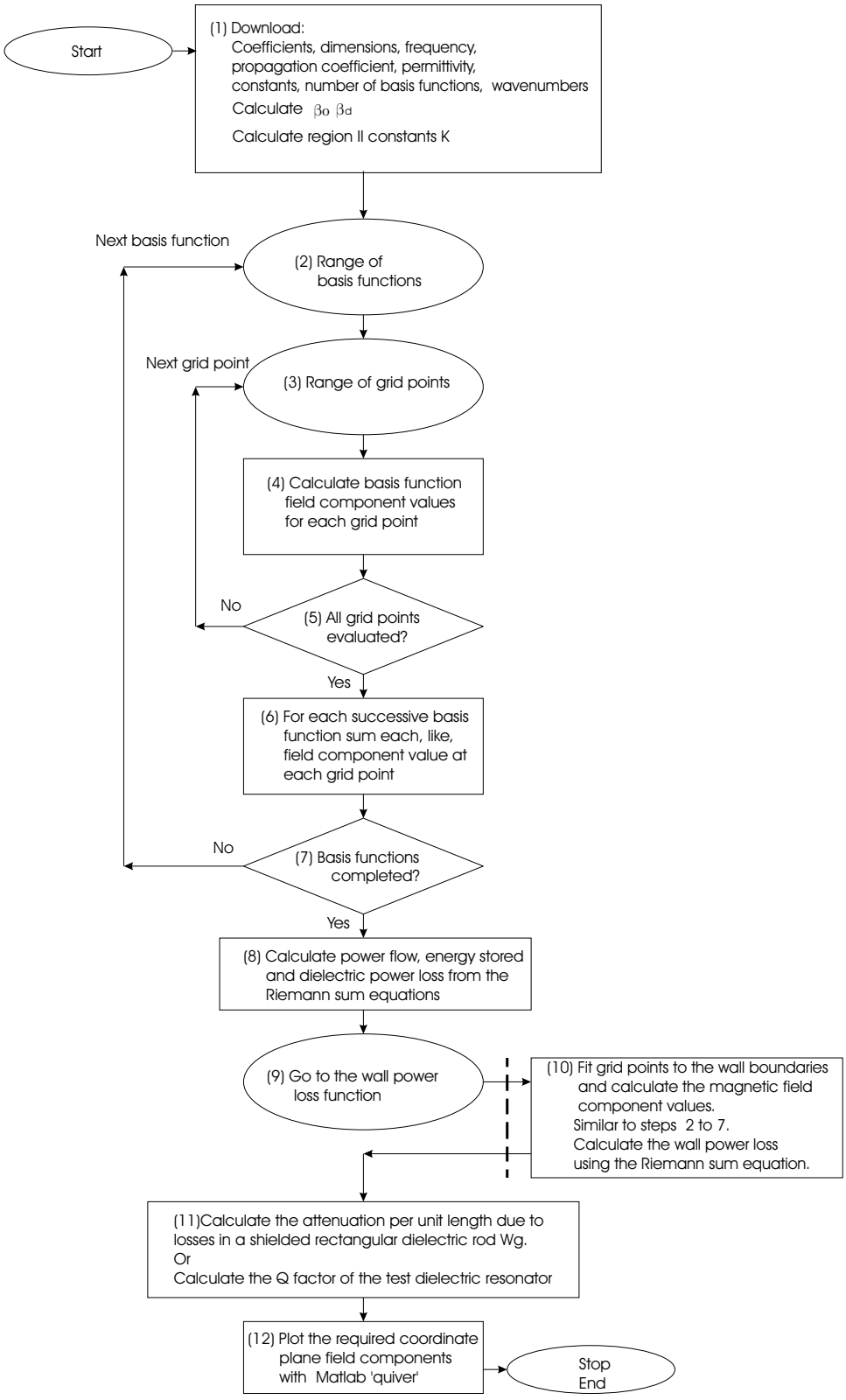

Figure 5.19: Flow chart of the program to find the attenuation due to power losses of the shielded rectangular dielectric rod waveguide and the Q factor of the test resonator.

1 to 7. These steps of the flow chart have the same function as the programing steps described in section 4.5.2 for the field plotting program of a propagating mode. The only difference is that the grid is offset by a half space to facilitate the Riemann sum elemental areas. Compare Figures 4.9 and 5.3 which show the grid setup in both cases.

8. Using the Riemann sum equations calculate the power flow (equation (5.10)) and dielectric loss (equation (5.11)) of the shielded rectangular dielectric rod waveguide and/or the energy stored (equation (5.27)), dielectric loss (equation (5.30)) and end plate loss (equation (5.33)) of the test resonator.

9. Go to the wall power loss function.

10. This sub-routine performs the same function as in steps 1 to 7 of the main program but the grid points are arranged to only fall on the wall contour boundary. The Riemann sum equations calculate the shield wall loss (equation (5.12)) of the shielded rectangular dielectric rod waveguide and/or the shield wall loss (equation (5.32)) of the test resonator. Return to the main program.

11. Calculate the attenuation coefficient due to dielectric and shield wall loss using equation (5.3) and/or the Q factor of the test resonator from equation (5.23).

12. Plot the electric and magnetic field pattern of the quarter cross-section. This is an optional step but is recommended because it allows a check as to whether the correct mode has been used in calculation. Also if a mistake has made in entering a dimension or variable etc, this will show up as a very poor field match at the mode matching boundary.

A copy of the computer programs described in this section can be seen on the companion CD-ROM for this thesis and operating details are given in Appendix D.

5.9 Conclusion

In this chapter a numerical method for finding the attenuation coefficient of a shielded rectangular dielectric rod waveguide has been presented. The method is based on well known formulae for power and loss in association with the field calculations of the modified Solbach and Wolff mode matching method described in Wells & Ball (2005*b*). The effect on the attenuation coefficient of frequency, and the proximity of the shield to the dielectric rod, has also been shown for both the E_{11}^y mode and the dominant E_{21}^x/E_{12}^y coupled modes. These mode matching results are original for this type of structure.

The method is confirmed by close comparison with a direct method for calculating the attenuation coefficient due to the dielectric and also with analytically calculated values for a rectangular waveguide completely filled with dielectric. The method is also validated by good comparison of the measured and calculated Q values of the shielded dielectric rod waveguide when used as a resonator. The difference between calculated and measured Q values is on average less than 4%; the worst result differing by 8.5%.

This method of finding the losses of the hybrid modes will have application in the design of rectangular shielded dielectric rod waveguide and fundamental mode dielectric-loaded cavity resonators.

Chapter 6

Conclusion

6.1 Project Overview

The main proposition of this thesis is that the mode matching method has significant advantages for the analysis of the electromagnetic fields of structures used in current dielectric loaded multimode cavity filters. The broad aim of the project was then to use mode matching to perform electromagnetic field analysis on the rectangular shielded dielectric rod waveguide.

As set out in the Introduction of the thesis the main objective was to completely characterise this structure and this has been achieved. The work has included an investigation of the proximity effect of the shield to the dielectric on the propagation coefficient and field patterns and of the distribution of losses within this structure. This has to provided a foundation for a complete analysis of the shielded rectangular cross-section dielectric resonators (as has been achieved for cylindrical resonators (Zaki & Atia, 1983)). This could then be seen as a precursor to later research on a cubic dielectric loaded multimode cavity resonator and the present design problems as discussed with filter manufacturer Filtronic (see chapter 1, Introduction, p. 3).

The numerical results have been confirmed by experimental measurements on short circuited lengths of this waveguide.

Section 6.2 to 6.4 summarise the major findings of the thesis and their significance to the wider body of knowledge in the field. The chapter concludes with summaries of original work and suggested areas for future work.

6.2 The Resonant Frequency and Gap Capacitance of a Coaxial Resonator

In Chapter 3 a simplified mode matching method of finding the TEM mode resonant frequencies of a coaxial resonator, and calculation of the gap capacitance was presented. The procedure, initially started to obtain expertise in mode matching eigenvalue problems, was found to have enough original content to be the subject of a paper published in *IEE Proceedings on Microwave Antennas and Propagation* (Wells & Ball, 2004). In the course of this preliminary work some general characteristics that can be encountered with mode matching were revealed.

6.2.1 Characteristics of the Mode Matching Solution

The accuracy of the resonant frequency calculations for the coaxial resonator are limited principally by three factors:

- the size of the steps between frequencies over the range tested (section 3.3);
- the number of modes used in each region (which determines the degree of convergence to the solution - section 3.6.1); and
- the number of modes that can be used before numerical problems occur which in turn limits the possibility of good convergence. This is due to matrix element values exceeding the dynamic range of the computer (section 3.6.1). At the same

time the problem is further complicated by the requirement to keep the ratio of modes in each region close to that of the region heights so as to satisfy the relative convergence criteria. This is difficult in the coaxial resonator structure as the ratio of heights is generally large.

Despite these limitations the resonant frequency values calculated for the coaxial resonator (without a tuning screw) were shown to be within 1% of measured values (section 3.5).

The accuracy of the unknown coefficients and field plotting is limited similarly by the same numerical problems as the resonant frequency calculations. However in this case the solution to a set of linear equations is required, not just eigenvalues found from the zeros of the determinant of the homogeneous equation matrix. The availability of a solution is now limited by the onset of rank deficiency of the matrix (section 3.6.2), which occurs before problems with computer dynamic range, as the gap size becomes smaller. Therefore this aspect of the method is limited to the field plotting of TEM modes in coaxial resonators with larger gap sizes. In the example structure of section 3.6.2 the region height ratio (gap width to structure length) had to be greater than 1/8.

These limitations of the mode matching method for the coaxial resonator would seem to be generic for MM, and appear not to have been emphasised in literature.

Traditionally coaxial filters have been designed using filter theory based on TEM mode transmission line structures. The mode matching procedure (Wells & Ball, 2004) presented in Chapter 3 allows a more accurate determination of the resonant frequency than the traditional procedure as it takes into account the effective gap capacitance of the whole structure and not just the simple parallel plate gap model. Furthermore the method described has been tailored to only find resonant frequencies of the desired TEM modes, and so the computer program is more efficient as it is not encumbered with unwanted code. However, because this method is designed to reproduce TEM resonances, the cutoff frequencies of coaxial TE and TM modes in the structure of

interest should always be calculated, as some of these modes may exist (Pozar, 1998, p. 143), but not show up in the solution. The method also allows an accurate method of calculating the gap capacitance.

6.3 Propagation in a Shielded Rectangular Dielectric Rod Waveguide

There has always been difficulty obtaining accurate propagation coefficients for the various modes in rectangular dielectric rod waveguide (Sudbo, 1992). In Chapter 4 a mode matching method (Wells & Ball, 2005*b*) was developed to calculate the propagation coefficients and field patterns of the modes in this type of structure with a surrounding rectangular shield. The unshielded result can still be realised by moving the shield a sufficient distance from the rod where it has negligible effect.

The analysis performed reveals the original result that when the dielectric is shielded there exists dominant E^x_{21}/E^y_{12} coupled modes, a fundamental E^x_{11} mode, and all the higher order modes associated with OO and EO symmetry. These higher order modes had not previously been identified (section 4.2).

The chapter is an expansion of a paper accepted for publication in *IEEE Transactions on Microwave Theory and Techniques* (Wells & Ball, 2005*b*).

The accuracy of the propagation coefficient calculations in the shielded rectangular dielectric rod are limited by a number of factors, some of which are similar to that of the coaxial resonator problem. These are:

- the size of the steps between propagation coefficient values over the range tested (section 4.5.1);
- The number and the ratio of basis functions used in each region, and the proximity of the shield to the dielectric determines the rate of convergence to the solution.

In particular:

1. The number of basis functions is limited to a maximum value, beyond which numerical problems occur. This is due to matrix element values exceeding the dynamic range of the computer, creating operations that are considered mathematically undefined by the software (Matlab etc) so that no solution is possible. However the number of basis functions required for sufficient convergence was always well below this limit (section 4.10.2).
2. The configuration of the modified Solbach and Wolf method, for the shielded dielectric rod waveguide, requires that an equal number of modes must be used in each region. This was found to give very good convergence and therefore automatically satisfies the relative convergence criteria (section 4.10.2).
3. As the shield in the structure is moved closer to the dielectric rod more basis functions are required to maintain the same degree of convergence. However for the accuracy required the number of basis functions necessary was always well below the maximum limit described in point 1 above (sections 4.6.2 and 4.10.2).

And in addition:

- caution has to be observed when searching for the wavenumbers $\beta_{y_n}^{(II_2)}$ and $\beta_{y_n}^{(II_1)}$ to ensure that none in the selected range are overlooked. Missed values generally occurred when, in an effort to speed up the root finding process, too large a step size was used between the wavenumber estimates. Missed wavenumbers can cause poor convergence and inaccuracy in propagation coefficient calculations and in extreme cases no solution will be found (section 4.10.1).

With these limitations taken into account, a comparison of calculated and measured propagation coefficients of the more dominant E_{11}^x, E_{11}^y modes and the E_{21}^x/E_{12}^y coupled mode were found to be within 2% over a wide frequency range (section 4.9, p. 88). More typically though, away from the steep slope of the mode diagram curves near

propagation cut off (section 4.6.5), the difference between measured and calculated values is less than 0.5% (section 4.10.2, p. 92).

The accuracy of the unknown coefficients and field plotting (see section 4.10.3) is limited by the same numerical problems as the propagation coefficient calculations. As was the case of the coaxial resonator problem, the availability of a solution is now determined as well by the rank deficiency of the equation matrix (section 4.10.3). In this case however the matrix condition is superior to the coaxial resonator problem because, as previously stated, the relative convergence criteria is conveniently satisfied. This means that sufficient modes can be used to give quite accurate field component values before any numerical problems occur (section 4.10.2). This is borne out by the good results obtained in Chapter 5 for the attenuation of the shielded rectangular dielectric rod waveguide (section 5.7).

The method developed allows the effect of shield proximity to be assessed, and so has application to the design of cavity filters incorporating rectangular parallelepiped or cubic dielectric resonators. It is easily extended to include calculation of both dielectric losses, and conductor losses in the shield wall, which may be used as a guide to resonator design. As noted in section 4.10 there are some limitations to the method but knowledge of these will allow sufficiently accurate results for most purposes to be achieved. This work could extended to the calculation of the resonant frequencies of fundamental mode dielectric-loaded cavity resonators (considered further in section 6.6 below).

6.4 Attenuation of a Shielded Rectangular Dielectric Rod Waveguide

In Chapter 5 the calculation of the attenuation coefficient of the commonly-used E_{11}^{y} mode, and other fundamental modes, in a shielded rectangular dielectric rod waveguide was presented. The influence on the attenuation coefficient of the proximity of the shield to the rod was also evaluated. This result is not reported in literature, and has therefore

been submitted for publication (Wells & Ball, 2005*a*).

The accuracy of the numerical grid method of finding the attenuation of a shielded rectangular dielectric rod waveguide described in Chapter 5 is dependent on the size of the grid used. It was found that for shield-to-dielectric dimension ratios above 1.3 a grid size of 51x51 gave results that were within 2% of those for a 501x501 grid. The smaller grid size took only minutes to compute on a 1.6GHz PC using Matlab code. Below this dimension ratio, larger grid sizes were required and an inherent exponential rise in processing time occurred (section 5.5.1).

Verification of the attenuation coefficient results was achieved by comparing calculated and measured Q at the resonant frequencies of a number of shielded rectangular dielectric rod resonators. The difference between calculated and measured Q values is on average less than 4%; the worst result differing by 8.5%.

The loss in rectangular dielectric waveguides is mostly due to that in the dielectric. However, if the waveguide is surrounded by a rectangular metallic shield, then the total loss of the waveguide will also include loss due to induced currents in the inner surface of the shield walls. From the method of Chapter 4 (Wells & Ball, 2005*b*) the values of the modal field components for a shielded rectangular dielectric rod can be calculated. In Chapter 5 using the numerical grid method (Wells & Ball, 2005*a*) the fields of the commonly used E_{11}^y mode and the E_{21}^x/E_{12}^y coupled modes were employed to find the respective wall and dielectric losses of the waveguides and hence their attenuation (section 5.5.1). The effect of the proximity of the shield on the attenuation of these modes was also evaluated and is summarised below:

- For the E_{11}^y mode in the structure described it was found that, as the shield size increases relative to the dielectric, the attenuation due to wall loss is gradually dominated by a relatively constant attenuation due to the loss of the dielectric. This indicates that when using the dielectric described, choosing a shield-to-dielectric dimension ratio SDDR greater than 2, will minimise the effect of the shield conductor loss. Another observation was that for the attenuation due to

wall loss to equal that of the dielectric the shield had to be relatively close to the dielectric with an SDDR of about 1.16 (section 5.5.1).

- It was found that the attenuation coefficient was appreciably lower for the dominant E_{21}^x/E_{12}^y coupled mode compared to the E_{11}^y mode owing to its lower dielectric loss while maintaining a relatively low shield wall conduction loss. This was due to the smaller intensity of the electric field in the dielectric compared to the air region for this mode (section 5.5.1).

These results will have application in the design of rectangular shielded dielectric rod waveguide and fundamental mode dielectric-loaded cavity resonators.

6.5 Summary of Original Work

The areas of this project where original work has been performed are summarised below.

1. A simplified mode matching method of finding the resonant frequency of a coaxial resonator, and calculation of the gap capacitance. This preliminary work in the project revealed a number of general limitations of the mode matching method that appear not to have been emphasised in literature.

2. Development of a mode matching method to calculate the propagation coefficients and field patterns of the modes in a shielded rectangular dielectric rod waveguide. Propagating, complex, evanescent and backward wave modes were included and the work showed the presence of a dominant mode, and other fundamental modes, not previously identified. The effect of the shield proximity on the propagation characteristics and mode spectrum was investigated. The limitations on the accuracy of the mode matching method developed for this type of structure were also revealed.

3. Development of a numerical method and computer program, using the fields ascertained in (2), to calculate the attenuation coefficient of the commonly used

E_{11}^{y} mode and the E_{21}^{x}/E_{12}^{y}coupled modes in a shielded rectangular dielectric rod waveguide. The effect on the attenuation coefficient of the proximity of the shield to the rod was also evaluated for both these modes. Limitations on accuracy were also discussed.

6.6 Recommendations for Future Work

It was always the intention that the present project would provide the foundations for a study of the rectangular dielectric rod in a rectangular waveguide cavity and once this was completed the work could be extended to the cubic dielectric resonator in a rectangular cavity.

6.6.1 The Rectangular Dielectric Rod in a Rectangular Waveguide Cavity

This work is surmised to follow closely the method described by Zaki & Atia (1983) where a cylindrical dielectric rod in a cylindrical waveguide cavity was modeled. The propagation characteristics of an infinite cylindrical waveguide containing a dielectric rod were first established. This could be calculated analytically. Then a cylindrical cavity was modeled as a length of this guiding structure, terminated in short lengths of empty waveguide. This formed a dielectric rod loaded cavity. Mode matching was applied at the boundaries between these regions to solve the eigenvalue problem of the determination of the resonant frequencies of the possible modes.

The differences in this process for a mode matching method to model the rectangular dielectric rod in a rectangular waveguide cavity would be:

1. Propagation coefficients for an infinite waveguide would have to be calculated numerically for a range of frequencies covering the suspected frequency range of resonant modes in a rectangular dielectric loaded cavity. These propagation coef-

ficients and the type and number of possible resonant modes could be ascertained by using the mode matching method of Chapter 4 on a particular structure to produce a mode chart (for example see Figure 4.14) over the frequency area of interest.

2. As in Chapter 4, due to symmetry, only a quarter of the cross-section would need to be used in calculation. Also if the dielectric rod is placed in the centre of the rectangular cavity symmetry would allow that only half the length of the structure would be necessary in the computation.

3. Standard rectangular waveguide equations would be used as basis functions in the empty rectangular waveguide ends of the structure.

4. In the rectangular shielded dielectric rod waveguide part of the structure, the basis functions used in Chapter 4 would be used, but there would be individual groups of these. One for each rectangular shielded dielectric rod waveguide mode determined from the mode chart. The number of basis functions in each mode group would have to be large enough to allow a sufficiently accurate determination of each mode.

5. The rectangular shielded dielectric rod waveguide modes obtained from the mode chart would have to include backward waves, complex modes and evanescent modes as well as the propagating modes. A sufficient number of these ('built up' from the basis functions) would be required to give an accurate determination of the resonant modes in the structure.

6. In the one quarter cross-section mode matching method used in Chapter 4 the position of electric and magnetic wall boundaries (section 4.4 pp. 56,57) determines the basis functions and type of modes found in the solution. Therefore in the resonator described here only the symmetry that produces an expected resonant mode would be required in computation, ie only the modes produced from a particular symmetry will be required to 'build up' the resonant mode fields in the cavity.

6.6.2 The Cubic Dielectric Resonator in a Rectangular Cavity

This would follow on from the previous topic and could encompass the multimode aspects of this type of structure as described by Hunter (2001, p. 298) and the empirical approach of Walker & Hunter (2002).

6.6.3 Benefits of the Recommended Work

The benefits to be expected if these solutions were carried out would be:

- A greater understanding of the effect of the proximity of rectangular cavity walls to a parallelepiped type dielectric resonator.
- An accurate dissection of the loss due to the cavity walls and the dielectric and their effect on the Q factor.
- Accurate calculation of the resonant frequency of dominant and higher order modes and hence their distance from the desired resonant mode. This can be important where high stop band attenuation is required.

References

Alessandri, F., Bartolucci, G. & Sorrentino, R. (1988), 'Admittance matrix formulation of waveguide discontinuity problems: Computer- aided design of branch guide directional couplers', *IEEE Transactions on Microwave Theory and Techniques* **36**(2), 394–403.

Arndt, F., Bayer, R., Reiter, J. M., Sieverding, T. & Wolf, T. (1997), 'Automated design of waveguide components using hybrid mode Matchning/Numerical EM building blocks in optimisation orientated CAD frame-works – state of the art and recent advances', *IEEE Transactions on Microwave Theory and Techniques* **45**(5), 747–759.

Atia, A. E. & Williams, A. E. (1972), 'Narrow -bandpass waveguide filters', *IEEE Transactions on Microwave Theory and Techniques* **20**, 258–265.

Balanis, C. A. (1988), *Advanced Engineering Electromagnetics*, Wiley, New York.

Chambers, L. (1953), 'Propagation in waveguides filled longitudinally with two or more dielectrics', *Journal of Applied Physics* **4**, 39–45.

Chen, S. W. (1990), Analysis and Modeling of Dielectric Loaded Resonators, Filters and Periodic Structures, PhD thesis, University of Maryland, College Park. UMI Dissertation Services 300 N.Zeeb Road, Ann Arbor, Michigan, USA.

Chen, S.-W. & Zaki, K. A. (1991), 'Dielectric ring resonators loaded in waveguide and on a substrate', *IEEE Transactions on Microwave Theory and Techniques* **39**(12), 2069–2076.

Chu, T. S. & Itoh, T. (1986), 'Generalized scattering matrix for analysis of cascaded and offset microstrip step discontinuities', *IEEE Transactions on Microwave Theory and Techniques* **34**(2), 280–284.

Clarricotes, P. J. B. & Slinn, K. R. (1967), 'Numerical solution of waveguide discontinuity problems', *Proceedures IEE* **114**(7), 878–886.

Collin, R. E. (1991), *Field Theory of Guided Waves*, 2 edn, IEEE Press.

Collin, R. E. & Ksienski, D. A. (1987), 'Boundary element method for dielectric resonators and waveguides', *Radio Science* **22**(7), 1155 – 1167.

Conte & DeBoor (1980), *Elementary Numerical Analysis*, 2nd edn, McGraw Hill, New York.

Craven, G. F. & Mok, C. K. (1971), 'The design of evanescent mode waveguide filters for a prescribed insertion loss characteristic', *IEEE Transactions on Microwave Theory and Techniques* **19**, 295–308.

Eleftheriades, G. V., Omar, A. S., Kathi, L. P. B. & Rebeiz, G. M. (1994), 'Some important properties of waveguide junction generalised scattering matrices in the context of the mode matching technique', *IEEE Transactions on Microwave Theory and Techniques* **42**(10), 1896–1903.

Engel-Jr., A. G. & Kathi, L. P. B. (1991), 'Low loss monolithic transmission lines for submillimeter and terahertz frequency applications', *IEEE Transactions on Microwave Theory and Techniques* **39**(11), 1847–1854.

Fiedziuszko, S. J. (1982), 'Dual-mode dielectric resonator loaded cavity filters', *IEEE Transactions on Microwave Theory and Techniques* **30**(9), 1311–1316.

Gesche, R. & Lochel, N. (1988), 'Scattering by a lossy dielectric cylinder in a rectangular waveguide', *IEEE Transactions on Microwave Theory and Techniques* **36**(1), 137–144.

Goell, J. E. (1969), 'A circular-harmonic computer analysis of rectangular dielectric waveguides', *The Bell System Technical Journal* **48**(9), 2133–2160.

Harrington, R. F. (2001), *Time Harmonic Electromagnetic Fields*, IEEE Press Classic Reissue.

Hunter, I. (2001), *Theory and Design of Microwave Filters*, Electromagnetic Wave Series 48, The Institution of Electrical Engineers, London.

IRE Standards on Antennas and Waveguides: Definition of Terms, (1953), *Proceedings of IRE* **41**, 1721–1728.

Itoh, T. (1989), *Numerical Techniques for Microwave and Millimeter- Wave Passive Structures*, John Wiley.

James, G. L. (1987), 'Admittance of irises in coaxial and circular waveguides for TE11 mode excitation', *IEEE Transactions on Microwave Theory and Techniques* **35**(4), 430–434.

Kajfez, D. (1994), 'Linear fractional curve fitting for measurement of high q factors', *IEEE Transactions on Microwave Theory and Techniques* **42**(7), 1149–1153.

Kajfez, D. & Guillon, P. (1986), *Dielectric Resonators*, Artech House.

Kasa, I. (1976), 'A circle fitting procedure and its error analysis', *IEEE Transactions of Instrumentation and Measurement* pp. 8–14.

Knox, R. M. & Toulios, P. P. (1970), Integrated circuit for millimeter through optical frequency range, *in* J. Fox, ed., 'Proc. MRI Symposium on Submillimeter Wave', Polytechnic Press, Brooklyn, pp. 497–516.

Kobayashi, Y., Fukuoka, N. & Yoshida, S. (1981), 'Resonant modes for a shielded dielectric rod resonator', *Electronics and Communications in Japan - translation 1983 Scripta Publishing Co.* **64-B**(11), 46–51.

Kwok, R. S. & Liang, J.-F. (1999), 'Characterisation of high-q resonators for microwave-filter applications', *IEEE Transactions on Microwave Theory and Techniques* **47**(1), 111–114.

Leong, K. & Mazierska, J. (2002), 'Precise measurements of the q factor of dielectric resonators in the transmission mode - accounting for noise, crosstalk, delay of uncalibrated lines, coupling loss and coupling reactance', *IEEE Transactions on Microwave Theory and Techniques* **50**(9), 2115–2127.

Leroy, M. (1983), 'On the convergence of numerical results in modal analysis', *IEEE Transactions on Antennas and Propagation* **31**(4), 655–659.

Liang, X.-P. & Zaki, K. A. (1993), 'Modeling of cylindrical dielectric resonators in rectanglar waveguides and cavities', *IEEE Transactions on Microwave Theory and Techniques* **41**(12), 2174–2181.

Lioubtchenko, D., Tretyakov, S. & Dudorov, S. (2003), *Millimeter-Wave Waveguides*, Kluwer Academic Publishers, Boston.

Luebbers, R. J. & Munk, B. A. (1973), 'Analysis of thick rectangular waveguide windows with finite conductivity', *IEEE Transactions on Microwave Theory and Techniques* **21**(7), 461–468.

Marcatili, E. A. J. (1969), 'Dielectric rectangular waveguide and directional coupler for integrated optics', *The Bell System Technical Journal* **48**(9), 2071–2102.

Marcuvitz, N. (1951), *Waveguide Handbook*, McGraw-Hill. Reprint 1993 Short Run Press, Exeter.

Marozowski, M. & Mazur, J. (1990), 'Predicting complex waves in lossless guides', *Conference Proceedings: 20th European Microwave Conference* pp. 487–492.

Matthaei, G. L., Young, L. & Jones, E. M. T. (1984), *Microwave Filters, Impedance Matching Networks and Coupling Structure*, McGraw-Hill, New York.

Mittra, R. (1963), 'Relative convergence of the solution of a doubly infinite set of equations', *Journal of Research of the National Bureau of Standards- D. Radio Propagation* **67D**(2), 245–254.

Mittra, R., Hou, Y.-L. & Jamnejad, V. (1980), 'Analysis of open dielectric waveguides using mode-matching technique and variational methods', *IEEE Transactions on Microwave Theory and Techniques* **28**(1), 36–43.

Mittra, R. & Lee, S. W. (1971), *Analytical Techniques in the Theory of Guided Waves*, Macmillan, New York.

Morgan, S. P. (1949), 'Effect of suface roughness on eddy current losses at microwave frequencies', *Journal of Applied Physics (American)* **20**(4), 352–362.

Oliner, A. A., Peng, S.-T., Hsu, T.-I. & Sanchez, A. (1981), 'Guidance and leakage properties of a class of open dielectric waveguides: Part2- new physical effects', *IEEE Transactions on Microwave Theory and Techniques* **29**(9), 855–869.

Omar, A. S. & Schunemann, K. (1985), 'Transmission matrix representation of finline discontinuities', *IEEE Transactions on Microwave Theory and Techniques* **33**(9), 765–770.

Omar, A. S. & Schunemann, K. F. (1987), 'Complex and backward-wave modes in inhomogeneously and anisotropically filled waveguides', *IEEE Transactions on Microwave Theory and Techniques* **35**(3), 268–275.

Patzelt, H. & Arndt, F. (1982), 'Double-plane steps in rectangular waveguides and their application for transformers, irises and filters', *IEEE Transactions on Microwave Theory and Techniques* **30**(5), 771–776.

Penny, J. & Lindfield, G. (1995), *Numerical Methods Using Matlab*, Ellis Horwood, Sydney.

Pozar, D. M. (1998), *Microwave Engineering*, 2 edn, John Wiley and Sons.

Rahman, B. M. A. & Davies, J. B. (1984), 'Finite element analysis of optical and microwave waveguide problems', *IEEE Transactions on Microwave Theory and Techniques* **32**, 20–28.

Reiter, J. M. & Arndt, F. (1992), 'A boundary contour mode matching method for the rigorous analysis of cascaded arbitrarily shaped h-plane discontinuities in rectangular waveguide', *IEEE Microwave and Guide Wave Letters* **2**(10), 403–405.

Risley, E. W. (1969), 'Discontinuity capacitance of a coaxial line terminated in a circular waveguide', *IEEE Transactions on Microwave Theory and Techniques* **17**(2), 86–92.

Rizzi, P. A. (1998), *Microwave Engineering - Passive Circuits*, Prentice Hall.

Rong, Y. & Zaki, K. A. (1999), 'Full wave analysis of coupling between cylindrical combline resonators', *IEEE Transactions on Microwave Theory and Techniques* **47**(9), 1721–1729.

Sabbagh, M. E., Zaki, K. A., Yao, H.-W. & Yu, M. (2001), 'Full wave analysis of coupling between combline resonators and its application to combline filters with canonical configurations', *IEEE Transactions on Microwave Theory and Techniques* **49**(12), 2384–2393.

Safavi-Naini, R. & Macphie, R. H. (1981), 'On solving waveguide junction scattering problems by the conservation of complex power technique', *IEEE Transactions on Microwave Theory and Techniques* **29**(4), 337–343.

Safavi-Naini, R. & Macphie, R. H. (1982), 'Scattering at rectangular to rectangular waveguide junctions', *IEEE Transactions on Microwave Theory and Techniques* **30**(11), 2060–2063.

Sander, K. F. (1987), *Microwave Components and Systems*, Addison-Wesley.

Schweig, E. & Bridges, W. B. (1984), 'Computer analysis of dielectric waveguides: A finite difference method', *IEEE Transactions on Microwave Theory and Techniques* **32**(5), 531–541.

Shih, Y. C. & Gray, K. G. (1983), 'Convergence of numerical solutions of step type waveguide discontinuity problems by modal analysis', *IEEE MTT-S International Symposium Digest (Boston)* pp. 233–235.

Sieverding, T. & Arndt, F. (1992), 'Field theoretic CAD of open or aperture matched t-junction coupled rectangular waveguide structures', *IEEE Transactions on Microwave Theory and Techniques* **40**(2), 353–362.

Solbach, K. & Wolff, I. (1978), 'The electromagnetic fields and the phase constants of dielectric image lines', *IEEE Transactions on Microwave Theory and Techniques* **26**(4), 266–274.

Somlo, P. I. (1979), 'The effect of flange loss on the reflection coefficient of reduced height', *IEEE Transactions on Microwave Theory and Techniques* **27**(9), 795–797.

Strube, J. & Arndt, F. (1985), 'Rigorous hybrid-mode analysis of the transition from rectangular waveguide to shielded dielectric image line', *IEEE Transactions on Microwave Theory and Techniques* **33**(5), 391–401.

Sudbo, A. S. (1992), 'Why are accurate computations of mode fields in rectangular dielectric waveguides difficult?', *Journal of Lightwave Technology* **10**(4), 419–419.

Valor, L. & Zapata, J. (1995), 'Efficient finite element analysis of waveguides with lossy inhomogeneous anisotropic materials characterized by arbitrary permittivity and permeability tensors', *IEEE Transactions on Microwave Theory and Techniques* **43**(10), 2452–2459.

Veidt, B. (1998), 'Selecting 3-d electromagnetic software', *Microwave Journal* pp. 126–137.

Wade, J. D. & Macphie, R. H. (1986), 'Scattering at circular to rectangular waveguide junctions', *IEEE Transactions on Microwave Theory and Techniques* **34**(11), 1085–1091.

Walker, V. & Hunter, I. C. (2002), 'Design of triple mode TE01d resonator transmission filters', *IEEE Microwave and Wireless Components Letters* **12**(6), 215–217.

Wang, C., Zaki, K. A. & Atia, A. E. (1997), 'Dual mode conductor-loaded cavity filters', *IEEE Transactions on Microwave Theory and Techniques* **45**(8), 1240–1246.

Wang, C., Zaki, K. A., Atia, A. E. & Dolan, T. G. (1998), 'Dielectric combline resonators and filters', *IEEE Transactions on Microwave Theory and Techniques* **46**(12), 2501–2506.

Wells, C. G. & Ball, J. A. R. (2004), 'Gap capacitance of a coaxial resonator using simplified mode matching', *IEE Proceedings on Microwave Antennas and Propagation* **151**(5), 399 – 403.

Wells, C. G. & Ball, J. A. R. (2005*a*), 'Attenuation of a shielded rectangular dielectric rod waveguide', *submitted for publication in IEEE Transactions on Microwave Theory and Techniques* .

Wells, C. G. & Ball, J. A. R. (2005*b*), 'Mode matching analysis of a shielded rectangular dielectric rod waveguide', *IEEE Transactions on Microwave Theory and Techniques* **53**(10), 3169–3177.

Wexler, A. (1967), 'Solution of waveguide discontinuities by modal analysis', *IEEE Transactions on Microwave Theory and Techniques* **15**(9), 508–517.

Wu, K.-L., Yu, M. & Sivadas, A. (2002), 'A novel modal analysis of a circular to rectangular waveguide t-junction and its application to the design of circular waveguide dual-mode filters', *IEEE Transactions on Microwave Theory and Techniques* **50**(2), 465–473.

Yao, H.-W. (1995), EM Simulation of Resonant and Transmission Structures - Applications to Filters and Multiplexers, PhD thesis, University of Maryland.

Yao, H.-W., Zaki, K. A., Atia, A. E. & Hershtig, R. (1995), 'Full wave modeling of conducting posts in rectangular wavguides and its applications to slot coupled combine filters', *IEEE Transactions on Microwave Theory and Techniques* **43**(12), 2824–2829.

Zaki, K. A. & Atia, A. E. (1983), 'Modes in dielectric-loaded wavguides and resonators', *IEEE Transactions on Microwave Theory and Techniques* **31**(12), 1039–1045.

Zaki, K. A. & Chen, C. (1986), 'New results in dielectric loaded resonators', *IEEE Transactions on Microwave Theory and Techniques* **34**(7), 815–824.

Zaki, K. A., Chen, S. W. & Chen, C. (1988), 'Modeling discontinuities in dielectric loaded waveguides', *IEEE Transactions on Microwave Theory and Techniques* **36**(12), 1804–1810.

Appendix A

Coaxial Resonator Mode Matching Equations

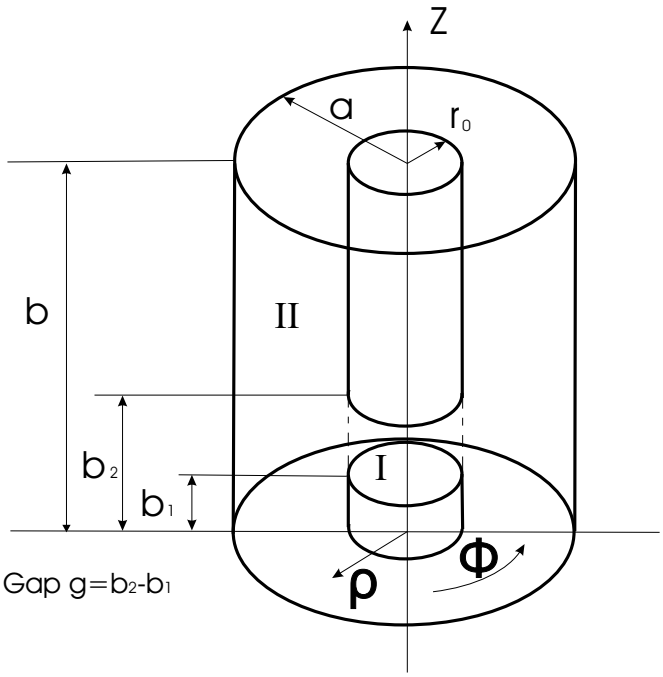

Figure A.1: Single coaxial resonator coordinate system and designations applicable to the equations presented in this appendix

A.1 The differential equations for Radial TM Modes

These equations are from Balanis (1988, p. 503)

$$
\begin{aligned}
H_\phi &= -\tfrac{1}{\mu}\tfrac{\partial A_z}{\partial \rho} \\
H_\rho &= \tfrac{1}{\mu\rho}\tfrac{\partial A_z}{\partial \phi} \\
E_\rho &= -j\tfrac{1}{\omega\mu\varepsilon}\tfrac{\partial^2 A_z}{\partial\rho\partial z} \\
E_\phi &= -j\tfrac{1}{\omega\mu\varepsilon}\tfrac{1}{\rho}\tfrac{\partial^2 A_z}{\partial\phi\partial z} \\
E_z &= -j\tfrac{1}{\omega\mu\varepsilon}\left(\tfrac{\partial^2}{z^2}+\beta^2\right)A_z
\end{aligned}
$$

A.2 Basis Functions for Region I

$$A_{z_I} = A_k^{TM} J_0\left(\beta_{\rho_I}\rho\right)\cos\left(\beta_{z_I}(z-b_1)\right) \tag{A.1}$$

$$E_{z_I} = -j\frac{A_k^{TM}}{\omega\mu_0\varepsilon_0\varepsilon_r}\beta_{\rho_I}^2 J_0(\beta_{\rho_I}\rho)\cos(\beta_{z_I}(z-b_1)) \tag{A.2}$$

$$E_{\rho_I} = j\frac{A_k^{TM}}{\omega\mu_0\varepsilon_0\varepsilon_r}\beta_{\rho_I} J_0{}'(\beta_{\rho_I}\rho)\sin(\beta_{z_I}(z-b_1)) \tag{A.3}$$

$$H_{\phi_I} = -\frac{A_k^{TM}}{\mu_0}\beta_{\rho_I} J_0{}'(\beta_{\rho_I}\rho)\cos(\beta_{z_I}(z-b_1)) \tag{A.4}$$

where: $\beta_z = (\frac{k\pi}{b_2-b_1})$; $\beta_\rho^2 = \beta_0^2 - \beta_z^2$; $\beta_0^2 = \omega^2\mu_0\varepsilon_0\varepsilon_r$

As there is no circumferential variation considered the other field components are zero.

A.3 Basis Functions for Region II

$$A_{z_{II}} = B_n^{TM}(Y_0(\beta_{\rho_{II}}a)J_0(\beta_{\rho_{II}}\rho) - J_0(\beta_{\rho_{II}}a)Y_0(\beta_{\rho_{II}}\rho))\cos(\beta_{z_{II}}) \quad \text{(A.5)}$$

$$E_{z_{II}} = -j\frac{B_n^{TM}}{\omega\mu_0\varepsilon_0\varepsilon_r}\beta_{\rho_{II}}^2(Y_0(\beta_{\rho_{II}}a)J_0(\beta_{\rho_{II}}\rho) - J_0(\beta_{\rho_{II}}a)Y_0(\beta_{\rho_{II}}\rho)) \cdot\cos(\beta_{z_{II}}) \quad \text{(A.6)}$$

$$E_{\rho_{II}} = j\frac{B_n^{TM}}{\omega\mu_0\varepsilon_0\varepsilon_r}\beta_{\rho_{II}}(Y_0(\beta_{\rho_{II}}a)J_0{}'(\beta_{\rho_{II}}\rho) - J_0(\beta_{\rho_{II}}a)Y_0{}'(\beta_{\rho_{II}}\rho)) \cdot\sin(\beta_{z_{II}}) \quad \text{(A.7)}$$

$$H_{\phi_{II}} = -\frac{B_n^{TM}}{\mu_0}\beta_{\rho_{II}}(Y_0(\beta_{\rho_{II}}a)J_0{}'(\beta_{\rho_{II}}\rho) - J_0(\beta_{\rho_{II}}a)Y_0{}'(\beta_{\rho_{II}}\rho)) \cdot\cos(\beta_{z_{II}}) \quad \text{(A.8)}$$

where: $\beta_{z_{II}} = (\frac{n\pi}{b})$; $\beta_{\rho_{II}}^2 = \beta_0^2 - \beta_{z_{II}}^2$; $\beta_0^2 = \omega^2\mu_0\varepsilon_0\varepsilon_r$
and the prime ' $\prime$ ' represents the differential of the particular Bessel function.

As there is no circumferential variation considered the other field components are zero.

A.4 Summary of Integrals

A.4.1 Cross-product of the Basis Functions and Testing Functions of the Same Region

A summary of the integrals derived from orthogonality relation equation (3.10) (ie the integrals are for a field equation and testing function from the same region):

$$I_{SS} = \int_{b_1}^{b_2} \sin\frac{m\pi z}{B}\sin\frac{n\pi z}{B}\,dz = \frac{B}{2} \quad \text{for } m = n$$
$$= 0 \quad \text{for } m \neq n \quad \text{(A.9)}$$

$$I_{CC} = \int_{b_1}^{b_2} \cos\frac{m\pi z}{B}\cos\frac{n\pi z}{B}\,dz \quad = \quad \frac{B}{2} \qquad \text{for } m = n$$
$$= \quad 0 \qquad \text{for } m \neq n \tag{A.10}$$

Where:

$B = b_2 - b_1$ for a region I equation and a region I testing function or

$B = b$ for a region II equation and a region II testing function.

A.4.2 Cross-product of the Basis Functions and Testing Functions of the Different Regions

A summary of the integrals derived from the coupling integral equations (3.12) and (3.14)(ie the integrals are for a field equation and testing function from different regions) :

$$I_{SS} = \int_{b_1}^{b_2} \sin\frac{m\pi z}{b}\sin\frac{n\pi z}{b_2 - b_1}\,dz \tag{A.11}$$
$$= \frac{m\pi}{b_2 - b_1}\left((-1^{m+1})\sin\frac{n\pi b_2}{b} + \sin\frac{n\pi b_1}{b}\right) \cdot \Big/ \left(\left(\frac{m\pi}{b_2 - b_1}\right)^2 - \left(\frac{n\pi}{b}\right)^2\right) \tag{A.12}$$

$$I_{CC} = \int_{b_1}^{b_2} \cos\frac{m\pi z}{b}\cos\frac{n\pi z}{b_2 - b_1}\,dz \tag{A.13}$$
$$= \frac{n\pi}{b}\left(\sin\frac{n\pi b_1}{b} - (-1^m)\sin\frac{n\pi b_2}{b}\right) \cdot \Big/ \left(\left(\frac{m\pi}{b_2 - b_1}\right)^2 - \left(\frac{n\pi}{b}\right)^2\right) \tag{A.14}$$

.

Appendix B

Shielded Dielectric Rod Waveguide Mode Matching Equations

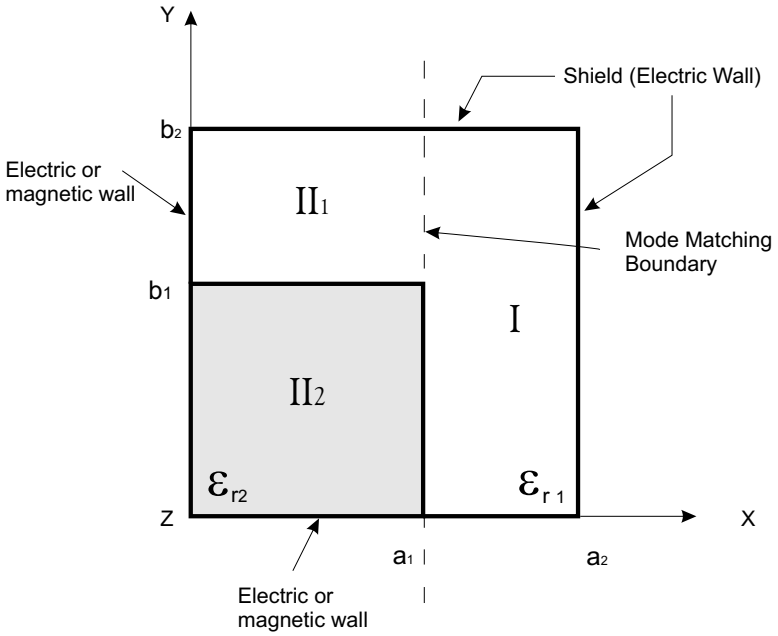

Figure B.1: One quarter of the rectangular dielectric line with shield, showing mode-matching regions and designations applicable to the equations presented in this appendix.

B.1 Basis Function Equations

B.1.1 Magnetic vector potential and longitudinal component basis function equations for TM^y

From Balanis (1988, p.397) longitudinal component basis function equations for TM^y can be derived from:

$$E_z = -j\frac{1}{\omega\mu\varepsilon}\frac{\partial^2 A_y}{\partial y \partial z}$$
$$H_z = \frac{1}{\mu}\frac{\partial A_y}{\partial x}$$

EO symmetry

$$\begin{aligned} A_{y_{me}}^{(I)EO} &= A_{me}^{(I)} \sin(\beta_{x_{me}}^{(I)}(a_2 - x)) \sin(\beta_{y_{me}}^{(I)} y) e^{-\gamma z} \\ A_{y_{ne}}^{(II_1)EO} &= B_{ne}^{(II_1)} \sin(\beta_{x_{ne}}^{(II_1)} x) \cos(\beta_{y_{ne}}^{(II_1)}(b_2 - y)) e^{-\gamma z} \\ A_{y_{ne}}^{(II_2)EO} &= B_{ne}^{(II_2)} \sin(\beta_{x_{ne}}^{(II_2)} x) \sin(\beta_{y_{ne}}^{(II_2)} y) e^{-\gamma z} \end{aligned} \tag{B.1}$$

$$\begin{aligned} E_{z_{me}}^{(I)EO} &= j\frac{A_{me}^{(I)}\beta_{y_{me}}^{(I)}\gamma}{\omega\mu_o\epsilon_o} \sin(\beta_{x_{me}}^{(I)}(a_2 - x)) \cos(\beta_{y_{me}}^{(I)} y) e^{-\gamma z} \\ E_{z_{ne}}^{(II_1)EO} &= j\frac{B_{ne}^{(II_1)}\beta_{y_{ne}}^{(II_1)}\gamma}{\omega\mu_o\epsilon_o} \sin(\beta_{x_{ne}}^{(II_1)} x) \sin(\beta_{y_{ne}}^{(II_1)}(b_2 - y)) e^{-\gamma z} \\ E_{z_{ne}}^{(II_2)EO} &= j\frac{B_{ne}^{(II_2)}\beta_{y_{ne}}^{(II_2)}\gamma}{\omega\mu_o\epsilon_o\epsilon_{r2}} \sin(\beta_{x_{ne}}^{(II_2)} x) \cos(\beta_{y_{ne}}^{(II_2)} y) e^{-\gamma z} \end{aligned} \tag{B.2}$$

$$\begin{aligned} H_{z_{me}}^{(I)EO} &= -\frac{A_{me}^{(I)}\beta_{x_{me}}^{(I)}}{\mu_o} \cos(\beta_{x_{me}}^{(I)}(a_2 - x)) \sin(\beta_{y_{me}}^{(I)} y) e^{-\gamma z} \\ H_{z_{ne}}^{(II_1)EO} &= \frac{B_{ne}^{(II_1)}\beta_{x_{ne}}^{(II_1)}}{\mu_o} \cos(\beta_{x_{ne}}^{(II_1)} x) \cos(\beta_{y_{ne}}^{(II_1)}(b_2 - y)) e^{-\gamma z} \\ H_{z_{ne}}^{(II_2)EO} &= \frac{B_{ne}^{(II_2)}\beta_{x_{ne}}^{(II_2)}}{\mu_o} \cos(\beta_{x_{ne}}^{(II_2)} x) \sin(\beta_{y_{ne}}^{(II_2)} y) e^{-\gamma z} \end{aligned} \tag{B.3}$$

OO symmetry

$$\begin{aligned} A_{y_{me}}^{(I)OO} &= A_{me}^{(I)} \sin(\beta_{x_{me}}^{(I)}(a_2 - x)) \sin(\beta_{y_{me}}^{(I)} y) e^{-\gamma z} \\ A_{y_{ne}}^{(II_1)OO} &= B_{ne}^{(II_1)} \cos(\beta_{x_{ne}}^{(II_1)} x) \cos(\beta_{y_{ne}}^{(II_1)}(b_2 - y)) e^{-\gamma z} \\ A_{y_{ne}}^{(II_2)OO} &= B_{ne}^{(II_2)} \cos(\beta_{x_{ne}}^{(II_2)} x) \sin(\beta_{y_{ne}}^{(II_2)} y) e^{-\gamma z} \end{aligned} \tag{B.4}$$

$$\begin{aligned} E_{z_{me}}^{(I)OO} &= j\frac{A_{me}^{(I)}\beta_{y_{me}}^{(I)}\gamma}{\omega\mu_o\epsilon_o} \sin(\beta_{x_{me}}^{(I)}(a_2 - x)) \cos(\beta_{y_{me}}^{(I)} y) e^{-\gamma z} \\ E_{z_{ne}}^{(II_1)OO} &= j\frac{B_{ne}^{(II_1)}\beta_{y_{ne}}^{(II_1)}\gamma}{\omega\mu_o\epsilon_o} \cos(\beta_{x_{ne}}^{(II_1)} x) \sin(\beta_{y_{ne}}^{(II_1)}(b_2 - y)) e^{-\gamma z} \\ E_{z_{ne}}^{(II_2)OO} &= j\frac{B_{ne}^{(II_2)}\beta_{y_{ne}}^{(II_2)}\gamma}{\omega\mu_o\epsilon_o\epsilon_{r2}} \cos(\beta_{x_{ne}}^{(II_2)} x) \cos(\beta_{y_{ne}}^{(II_2)} y) e^{-\gamma z} \end{aligned} \tag{B.5}$$

$$\begin{aligned} H_{z_{me}}^{(I)OO} &= -\tfrac{A_{me}^{(I)}\beta_{x_{me}}^{(I)}}{\mu_o}\cos(\beta_{x_{me}}^{(I)}(a_2-x))\sin(\beta_{y_{me}}^{(I)}y)e^{-\gamma z} \\ H_{z_{ne}}^{(II_1)OO} &= -\tfrac{B_{ne}^{(II_1)}\beta_{x_{ne}}^{(II_1)}}{\mu_o}\sin(\beta_{x_{ne}}^{(II_1)}x)\cos(\beta_{y_{ne}}^{(II_1)}(b_2-y))e^{-\gamma z} \\ H_{z_{ne}}^{(II_2)OO} &= -\tfrac{B_{ne}^{(II_2)}\beta_{x_{ne}}^{(II_2)}}{\mu_o}\sin(\beta_{x_{ne}}^{(II_2)}x)\sin(\beta_{y_{ne}}^{(II_2)}y)e^{-\gamma z} \end{aligned} \tag{B.6}$$

OE symmetry

$$\begin{aligned} A_{y_{me}}^{(I)OE} &= A_{me}^{(I)}\sin(\beta_{x_{me}}^{(I)}(a_2-x))\cos(\beta_{y_{me}}^{(I)}y)e^{-\gamma z} \\ A_{y_{ne}}^{(II_1)OE} &= B_{ne}^{(II_1)}\cos(\beta_{x_{ne}}^{(II_1)}x)\cos(\beta_{y_{ne}}^{(II_1)}(b_2-y))e^{-\gamma z} \\ A_{y_{ne}}^{(II_2)OE} &= B_{ne}^{(II_2)}\cos(\beta_{x_{ne}}^{(II_2)}x)\cos(\beta_{y_{ne}}^{(II_2)}y)e^{-\gamma z} \end{aligned} \tag{B.7}$$

$$\begin{aligned} E_{z_{me}}^{(I)OE} &= -j\tfrac{A_{me}^{(I)}\beta_{y_{me}}^{(I)}\gamma}{\omega\mu_o\epsilon_o}\sin(\beta_{x_{me}}^{(I)}(a_2-x))\sin(\beta_{y_{me}}^{(I)}y)e^{-\gamma z} \\ E_{z_{ne}}^{(II_1)OE} &= j\tfrac{B_{ne}^{(II_1)}\beta_{y_{ne}}^{(II_1)}\gamma}{\omega\mu_o\epsilon_o}\cos(\beta_{x_{ne}}^{(II_1)}x)\sin(\beta_{y_{ne}}^{(II_1)}(b_2-y))e^{-\gamma z} \\ E_{z_{ne}}^{(II_2)OE} &= -j\tfrac{B_{ne}^{(II_2)}\beta_{y_{ne}}^{(II_2)}\gamma}{\omega\mu_o\epsilon_o\epsilon_{r2}}\cos(\beta_{x_{ne}}^{(II_2)}x)\sin(\beta_{y_{ne}}^{(II_2)}y)e^{-\gamma z} \end{aligned} \tag{B.8}$$

$$\begin{aligned} H_{z_{me}}^{(I)OE} &= -\tfrac{A_{me}^{(I)}\beta_{x_{me}}^{(I)}}{\mu_o}\cos(\beta_{x_{me}}^{(I)}(a_2-x))\cos(\beta_{y_{me}}^{(I)}y)e^{-\gamma z} \\ H_{z_{ne}}^{(II_1)OE} &= -\tfrac{B_{ne}^{(II_1)}\beta_{x_{ne}}^{(II_1)}}{\mu_o}\sin(\beta_{x_{ne}}^{(II_1)}x)\cos(\beta_{y_{ne}}^{(II_1)}(b_2-y))e^{-\gamma z} \\ H_{z_{ne}}^{(II_2)OE} &= -\tfrac{B_{ne}^{(II_2)}\beta_{x_{ne}}^{(II_2)}}{\mu_o}\sin(\beta_{x_{ne}}^{(II_2)}x)\cos(\beta_{y_{ne}}^{(II_2)}y)e^{-\gamma z} \end{aligned} \tag{B.9}$$

EE symmetry

$$\begin{aligned} A_{y_{me}}^{(I)EE} &= A_{me}^{(I)}\sin(\beta_{x_{me}}^{(I)}(a_2-x))\cos(\beta_{y_{me}}^{(I)}y)e^{-\gamma z} \\ A_{y_{ne}}^{(II_1)EE} &= B_{ne}^{(II_1)}\sin(\beta_{x_{ne}}^{(II_1)}x)\cos(\beta_{y_{ne}}^{(II_1)}(b_2-y))e^{-\gamma z} \\ A_{y_{ne}}^{(II_2)EE} &= B_{ne}^{(II_2)}\sin(\beta_{x_{ne}}^{(II_2)}x)\cos(\beta_{y_{ne}}^{(II_2)}y)e^{-\gamma z} \end{aligned} \tag{B.10}$$

$$\begin{aligned} E_{z_{me}}^{(I)EE} &= -j\tfrac{A_{me}^{(I)}\beta_{y_{me}}^{(I)}\gamma}{\omega\mu_o\epsilon_o}\sin(\beta_{x_{me}}^{(I)}(a_2-x))\sin(\beta_{y_{me}}^{(I)}y)e^{-\gamma z} \\ E_{z_{ne}}^{(II_1)EE} &= j\tfrac{B_{ne}^{(II_1)}\beta_{y_{ne}}^{(II_1)}\gamma}{\omega\mu_o\epsilon_o}\sin(\beta_{x_{ne}}^{(II_1)}x)\sin(\beta_{y_{ne}}^{(II_1)}(b_2-y))e^{-\gamma z} \\ E_{z_{ne}}^{(II_2)EE} &= -j\tfrac{B_{ne}^{(II_2)}\beta_{y_{ne}}^{(II_2)}\gamma}{\omega\mu_o\epsilon_o\epsilon_{r2}}\sin(\beta_{x_{ne}}^{(II_2)}x)\sin(\beta_{y_{ne}}^{(II_2)}y)e^{-\gamma z} \end{aligned} \tag{B.11}$$

$$\begin{aligned} H_{z_{me}}^{(I)EE} &= -\tfrac{A_{me}^{(I)}\beta_{x_{me}}^{(I)}}{\mu_o}\cos(\beta_{x_{me}}^{(I)}(a_2-x))\cos(\beta_{y_{me}}^{(I)}y)e^{-\gamma z} \\ H_{z_{ne}}^{(II_1)EE} &= \tfrac{B_{ne}^{(II_1)}\beta_{x_{ne}}^{(II_1)}}{\mu_o}\cos(\beta_{x_{ne}}^{(II_1)}x)\cos(\beta_{y_{ne}}^{(II_1)}(b_2-y))e^{-\gamma z} \\ H_{z_{ne}}^{(II_2)EE} &= \tfrac{B_{ne}^{(II_2)}\beta_{x_{ne}}^{(II_2)}}{\mu_o}\cos(\beta_{x_{ne}}^{(II_2)}x)\cos(\beta_{y_{ne}}^{(II_2)}y)e^{-\gamma z} \end{aligned} \tag{B.12}$$

The rest of the TM^y basis function components can be derived from the equations described by Balanis (1988, p.397):

$$
\begin{aligned}
E_x &= -j\tfrac{1}{\omega\mu\varepsilon}\tfrac{\partial^2 A_y}{\partial x \partial y} \\
E_y &= -j\tfrac{1}{\omega\mu\varepsilon}\left(\tfrac{\partial^2}{y^2} + \beta^2\right) A_y \\
H_x &= -\tfrac{1}{\mu}\tfrac{\partial A_y}{\partial z} \\
H_y &= 0
\end{aligned}
$$

B.1.2 Electric vector potential and longitudinal component basis function equations for TE^y

From Balanis (1988, p.395) longitudinal component basis function equations for TE^y can be derived from:

$$E_z = \frac{1}{\varepsilon}\frac{\partial F_y}{\partial x}$$
$$H_z = -j\frac{1}{\omega\mu\varepsilon}\frac{\partial^2 F_y}{\partial y \partial z}$$

EO symmetry

$$\begin{aligned} F_{y_{mh}}^{(I)EO} &= A_{mh}^{(I)}\cos(\beta_{x_{mh}}^{(I)}(a_2-x))\cos(\beta_{y_{mh}}^{(I)}y)e^{-\gamma z} \\ F_{y_{nh}}^{(II_1)EO} &= B_{nh}\cos(\beta_{x_{nh}}^{(II_1)}x)\sin(\beta_{y_{nh}}^{(II_1)}(b_2-y))e^{-\gamma z} \\ F_{y_{nh}}^{(II_2)EO} &= B_{nh}^{(II_2)}\cos(\beta_{x_{nh}}^{(II_2)}x)\cos(\beta_{y_{nh}}^{(II_2)}y)e^{-\gamma z} \end{aligned} \tag{B.13}$$

$$\begin{aligned} E_{z_{mh}}^{(I)EO} &= -\frac{A_{mh}^{(I)}\beta_{x_{mh}}^{(I)}}{\epsilon_o}\sin(\beta_{x_{mh}}^{(I)}(a_2-x))\cos(\beta_{y_{mh}}^{(I)}y)e^{-\gamma z} \\ E_{z_{nh}}^{(II_1)EO} &= \frac{B_{nh}\beta_{x_{nh}}^{(II_1)}}{\epsilon_o}\sin(\beta_{x_{nh}}^{(II_1)}x)\sin(\beta_{y_{nh}}^{(II_1)}(b_2-y))e^{-\gamma z} \\ E_{z_{nh}}^{(II_2)EO} &= \frac{B_{nh}^{(II_2)}\beta_{x_{nh}}^{(II_2)}}{\epsilon_o\epsilon_{r2}}\sin(\beta_{x_{nh}}^{(II_2)}x)\cos(\beta_{y_{nh}}^{(II_2)}y)e^{-\gamma z} \end{aligned} \tag{B.14}$$

$$\begin{aligned} H_{z_{mh}}^{(I)EO} &= -j\frac{A_{mh}^{(I)}\beta_{y_{mh}}^{(I)}\gamma}{\omega\mu_o\epsilon_o}\cos(\beta_{x_{mh}}^{(I)}(a_2-x))\sin(\beta_{y_{mh}}^{(I)}y)e^{-\gamma z} \\ H_{z_{nh}}^{(II_1)EO} &= -j\frac{B_{nh}\beta_{y_{nh}}^{(II_1)}\gamma}{\omega\mu_o\epsilon_o}\cos(\beta_{x_{nh}}^{(II_1)}x)\cos(\beta_{y_{nh}}^{(II_1)}(b_2-y))e^{-\gamma z} \\ H_{z_{nh}}^{(II_2)EO} &= -j\frac{B_{nh}^{(II_2)}\beta_{y_{nh}}^{(II_2)}\gamma}{\mu_o\epsilon_o\epsilon_{r2}}\cos(\beta_{x_{nh}}^{(II_2)}x)\sin(\beta_{y_{nh}}^{(II_2)}y)e^{-\gamma z} \end{aligned} \tag{B.15}$$

OO symmetry

$$\begin{aligned} F_{y_{mh}}^{(I)OO} &= A_{mh}^{(I)}\cos(\beta_{x_{mh}}^{(I)}(a_2-x))\cos(\beta_{y_{mh}}^{(I)}y)e^{-\gamma z} \\ F_{y_{nh}}^{(II_1)OO} &= B_{nh}\sin(\beta_{x_{nh}}^{(II_1)}x)\sin(\beta_{y_{nh}}^{(II_1)}(b_2-y))e^{-\gamma z} \\ F_{y_{nh}}^{(II_2)OO} &= B_{nh}^{(II_2)}\sin(\beta_{x_{nh}}^{(II_2)}x)\cos(\beta_{y_{nh}}^{(II_2)}y)e^{-\gamma z} \end{aligned} \tag{B.16}$$

$$
\begin{aligned}
E_{z_{mh}}^{(I)OO} &= -\frac{A_{mh}^{(I)}\beta_{x_{mh}}^{(I)}}{\epsilon_o}\sin(\beta_{x_{mh}}^{(I)}(a_2-x))\cos(\beta_{y_{mh}}^{(I)}y)e^{-\gamma z} \\
E_{z_{nh}}^{(II_1)OO} &= -\frac{B_{nh}\beta_{x_{nh}}^{(II_1)}}{\epsilon_o}\cos(\beta_{x_{nh}}^{(II_1)}x)\sin(\beta_{y_{nh}}^{(II_1)}(b_2-y))e^{-\gamma z} \\
E_{z_{nh}}^{(II_2)OO} &= -\frac{B_{nh}^{(II_2)}\beta_{x_{nh}}^{(II_2)}}{\epsilon_o\epsilon_{r2}}\cos(\beta_{x_{nh}}^{(II_2)}x)\cos(\beta_{y_{nh}}^{(II_2)}y)e^{-\gamma z}
\end{aligned} \tag{B.17}
$$

$$
\begin{aligned}
H_{z_{mh}}^{(I)OO} &= -j\frac{A_{mh}^{(I)}\beta_{y_{mh}}^{(I)}\gamma}{\omega\mu_o\epsilon_o}\cos(\beta_{x_{mh}}^{(I)}(a_2-x))\sin(\beta_{y_{mh}}^{(I)}y)e^{-\gamma z} \\
H_{z_{nh}}^{(II_1)OO} &= -j\frac{B_{nh}\beta_{y_{nh}}^{(II_1)}\gamma}{\omega\mu_o\epsilon_o}\sin(\beta_{x_{nh}}^{(II_1)}x)\cos(\beta_{y_{nh}}^{(II_1)}(b_2-y))e^{-\gamma z} \\
H_{z_{nh}}^{(II_2)OO} &= -j\frac{B_{nh}^{(II_2)}\beta_{y_{nh}}^{(II_2)}\gamma}{\mu_o\epsilon_o\epsilon_{r2}}\sin(\beta_{x_{nh}}^{(II_2)}x)\sin(\beta_{y_{nh}}^{(II_2)}y)e^{-\gamma z}
\end{aligned} \tag{B.18}
$$

OE symmetry

$$
\begin{aligned}
F_{y_{mh}}^{(I)OE} &= A_{mh}^{(I)}\cos(\beta_{x_{mh}}^{(I)}(a_2-x))\sin(\beta_{y_{mh}}^{(I)}y)e^{-\gamma z} \\
F_{y_{nh}}^{(II_1)OE} &= B_{nh}\sin(\beta_{x_{nh}}^{(II_1)}x)\sin(\beta_{y_{nh}}^{(II_1)}(b_2-y))e^{-\gamma z} \\
F_{y_{nh}}^{(II_2)OE} &= B_{nh}^{(II_2)}\sin(\beta_{x_{nh}}^{(II_2)}x)\sin(\beta_{y_{nh}}^{(II_2)}y)e^{-\gamma z}
\end{aligned} \tag{B.19}
$$

$$
\begin{aligned}
E_{z_{mh}}^{(I)OE} &= -\frac{A_{mh}^{(I)}\beta_{x_{mh}}^{(I)}}{\epsilon_o}\sin(\beta_{x_{mh}}^{(I)}(a_2-x))\sin(\beta_{y_{mh}}^{(I)}y)e^{-\gamma z} \\
E_{z_{nh}}^{(II_1)OE} &= -\frac{B_{nh}\beta_{x_{nh}}^{(II_1)}}{\epsilon_o}\cos(\beta_{x_{nh}}^{(II_1)}x)\sin(\beta_{y_{nh}}^{(II_1)}(b_2-y))e^{-\gamma z} \\
E_{z_{nh}}^{(II_2)OE} &= -\frac{B_{nh}^{(II_2)}\beta_{x_{nh}}^{(II_2)}}{\epsilon_o\epsilon_{r2}}\cos(\beta_{x_{nh}}^{(II_2)}x)\sin(\beta_{y_{nh}}^{(II_2)}y)e^{-\gamma z}
\end{aligned} \tag{B.20}
$$

$$
\begin{aligned}
H_{z_{mh}}^{(I)OE} &= j\frac{A_{mh}^{(I)}\beta_{y_{mh}}^{(I)}\gamma}{\omega\mu_o\epsilon_o}\cos(\beta_{x_{mh}}^{(I)}(a_2-x))\cos(\beta_{y_{mh}}^{(I)}y)e^{-\gamma z} \\
H_{z_{nh}}^{(II_1)OE} &= -j\frac{B_{nh}\beta_{y_{nh}}^{(II_1)}\gamma}{\omega\mu_o\epsilon_o}\sin(\beta_{x_{nh}}^{(II_1)}x)\cos(\beta_{y_{nh}}^{(II_1)}(b_2-y))e^{-\gamma z} \\
H_{z_{nh}}^{(II_2)OE} &= j\frac{B_{nh}^{(II_2)}\beta_{y_{nh}}^{(II_2)}\gamma}{\mu_o\epsilon_o\epsilon_{r2}}\sin(\beta_{x_{nh}}^{(II_2)}x)\cos(\beta_{y_{nh}}^{(II_2)}y)e^{-\gamma z}
\end{aligned} \tag{B.21}
$$

EE symmetry

$$\begin{aligned} F_{y_{mh}}^{(I)EE} &= A_{mh}^{(I)} \cos(\beta_{x_{mh}}^{(I)}(a_2 - x)) \sin(\beta_{y_{mh}}^{(I)} y) e^{-\gamma z} \\ F_{y_{nh}}^{(II_1)EE} &= B_{nh} \cos(\beta_{x_{nh}}^{(II_1)} x) \sin(\beta_{y_{nh}}^{(II_1)}(b_2 - y)) e^{-\gamma z} \\ F_{y_{nh}}^{(II_2)EE} &= B_{nh}^{(II_2)} \cos(\beta_{x_{nh}}^{(II_2)} x) \sin(\beta_{y_{nh}}^{(II_2)} y) e^{-\gamma z} \end{aligned} \tag{B.22}$$

$$\begin{aligned} E_{z_{mh}}^{(I)EE} &= -\frac{A_{mh}^{(I)} \beta_{x_{mh}}^{(I)}}{\epsilon_o} \sin(\beta_{x_{mh}}^{(I)}(a_2 - x)) \sin(\beta_{y_{mh}}^{(I)} y) e^{-\gamma z} \\ E_{z_{nh}}^{(II_1)EE} &= \frac{B_{nh} \beta_{x_{nh}}^{(II_1)}}{\epsilon_o} \sin(\beta_{x_{nh}}^{(II_1)} x) \sin(\beta_{y_{nh}}^{(II_1)}(b_2 - y)) e^{-\gamma z} \\ E_{z_{nh}}^{(II_2)EE} &= \frac{B_{nh}^{(II_2)} \beta_{x_{nh}}^{(II_2)}}{\epsilon_o \epsilon_{r2}} \sin(\beta_{x_{nh}}^{(II_2)} x) \sin(\beta_{y_{nh}}^{(II_2)} y) e^{-\gamma z} \end{aligned} \tag{B.23}$$

$$\begin{aligned} H_{z_{mh}}^{(I)EE} &= j\frac{A_{mh}^{(I)} \beta_{y_{mh}}^{(I)} \gamma}{\omega \mu_o \epsilon_o} \cos(\beta_{x_{mh}}^{(I)}(a_2 - x)) \cos(\beta_{y_{mh}}^{(I)} y) e^{-\gamma z} \\ H_{z_{nh}}^{(II_1)EE} &= -j\frac{B_{nh} \beta_{y_{nh}}^{(II_1)} \gamma}{\omega \mu_o \epsilon_o} \cos(\beta_{x_{nh}}^{(II_1)} x) \cos(\beta_{y_{nh}}^{(II_1)}(b_2 - y)) e^{-\gamma z} \\ H_{z_{nh}}^{(II_2)EE} &= j\frac{B_{nh}^{(II_2)} \beta_{y_{nh}}^{(II_2)} \gamma}{\mu_o \epsilon_o \epsilon_{r2}} \cos(\beta_{x_{nh}}^{(II_2)} x) \cos(\beta_{y_{nh}}^{(II_2)} y) e^{-\gamma z} \end{aligned} \tag{B.24}$$

The rest of the TE^y basis function components can be derived from the equations described by Balanis (1988, p.395):

$$\begin{aligned} E_x &= \tfrac{1}{\varepsilon} \tfrac{\partial F_y}{\partial z} \\ E_y &= 0 \\ H_x &= -j \tfrac{1}{\omega \mu \varepsilon} \tfrac{\partial^2 F_y}{\partial x \partial y} \\ H_y &= -j \tfrac{1}{\omega \mu \varepsilon} \left(\tfrac{\partial^2}{y^2} + \beta^2 \right) F_y \end{aligned}$$

B.2 The Continuity Equations at the II_1/II_2 Boundary

A summary of the equations derived from the continuity of the longitudinal fields at the boundary $y = b_1,\ 0 \le x \le a_1$, for all symmetries:

EO and OO symmetry

$$K_{ne} = \frac{B_{ne}^{(II_1)}}{B_{ne}^{(II_2)}} = \frac{\beta_{y_{ne}}^{(II_2)} \cos(\beta_{y_{ne}}^{(II_2)} b_1)}{\beta_{y_{ne}}^{(II_1)} \epsilon_{r2} \sin(\beta_{y_{ne}}^{(II_1)} (b_2 - b_1))} \tag{B.25}$$

$$\frac{1}{\beta_{y_{ne}}^{(II_1)}} \cot(\beta_{y_{ne}}^{(II_1)} (b_2 - b_1)) = \frac{\epsilon_{r2}}{\beta_{y_{ne}}^{(II_2)}} \tan(\beta_{y_{ne}}^{(II_2)} b_1) \tag{B.26}$$

$$K_{nh} = \frac{B_{nh}^{(II_1)}}{B_{nh}^{(II_2)}} = \frac{\cos(\beta_{y_{nh}}^{(II_2)} b_1)}{\epsilon_{r2} \sin(\beta_{y_{nh}}^{(II_1)} (b_2 - b_1))} \tag{B.27}$$

$$\beta_{y_{nh}}^{(II_1)} \cot(\beta_{y_{nh}}^{(II_1)} (b_2 - b_1)) = \beta_{y_{nh}}^{(II_2)} \tan(\beta_{y_{nh}}^{(II_2)} b_1) \tag{B.28}$$

OE and EE symmetry

$$K_{ne} = \frac{B_{ne}^{(II_1)}}{B_{ne}^{(II_2)}} = \frac{\beta_{y_{ne}}^{(II_2)} \sin(\beta_{y_{ne}}^{(II_2)} b_1)}{\beta_{y_{ne}}^{(II_1)} \epsilon_{r2} \sin(\beta_{y_{ne}}^{(II_1)} (b_2 - b_1))} \tag{B.29}$$

$$\frac{1}{\beta_{y_{ne}}^{(II_1)}} \cot(\beta_{y_{ne}}^{(II_1)} (b_2 - b_1)) = -\frac{\epsilon_{r2}}{\beta_{y_{ne}}^{(II_2)}} \cot(\beta_{y_{ne}}^{(II_2)} b_1) \tag{B.30}$$

$$K_{nh} = \frac{B_{nh}^{(II_1)}}{B_{nh}^{(II_2)}} = \frac{\sin(\beta_{y_{nh}}^{(II_2)} b_1)}{\epsilon_{r2} \sin(\beta_{y_{nh}}^{(II_1)} (b_2 - b_1))} \tag{B.31}$$

$$\beta_{y_{nh}}^{(II_1)} \cot(\beta_{y_{nh}}^{(II_1)} (b_2 - b_1)) = -\beta_{y_{nh}}^{(II_2)} \cot(\beta_{y_{nh}}^{(II_2)} b_1) \tag{B.32}$$

where subscripts h and e are TM^y and TE^y respectively.

B.3 Summary of Integrals for Region I

A summary of the integrals, derived for all symmetries in region I, from the orthogonality equations (4.27) and (4.28):

$$\begin{aligned} I_{S_I S_I} = \int_0^{b_2} \sin\frac{m\pi y}{2b_2}\sin\frac{q\pi y}{2b_2}\,dy &= \frac{b_2}{2} \qquad \text{for } m = q,\ m \text{ and } q \geq 1 \\ &= 0 \qquad \text{for } m \text{ or } q = 0 \\ &= 0 \qquad \text{for } m \neq q \end{aligned} \tag{B.33}$$

$$\begin{aligned} I_{C_I C_I} = \int_0^{b_2} \cos\frac{m\pi y}{2b_2}\cos\frac{q\pi y}{2b_2}\,dy &= \frac{b_2}{2} \qquad \text{for } m = q,\ m \text{ and } q \geq 1 \\ &= b_2 \qquad \text{for } m \text{ or } q = 0 \\ &= 0 \qquad \text{for } m \neq q \end{aligned} \tag{B.34}$$

B.4 Summary of the Integrals for Regions II_1 and II_2

A summary of the integrals derived for regions II_1 and II_2 with TM^y or TE^y from the coupling integral equations (4.30) and (4.33):

EO and OO symmetry, region II_1

$$I_{C_{II_1} C_I} = \int_{b_1}^{b_2} \cos(\beta_{y_n}^{(II_1)}(b_2 - y))\cos\frac{q\pi y}{2b_2}\,dy \tag{B.35}$$

$$I_{S_{II_1} S_I} = \int_{b_1}^{b_2} \sin(\beta_{y_n}^{(II_1)}(b_2 - y))\sin\frac{q\pi y}{2b_2}\,dy \tag{B.36}$$

OE and EE symmetry, region II_1

$$I_{C_{II_1} S_I} = \int_{b_1}^{b_2} \cos(\beta_{y_n}^{(II_1)}(b_2 - y))\sin\frac{q\pi y}{2b_2}\,dy \tag{B.37}$$

$$I_{S_{II_1} C_I} = \int_{b_1}^{b_2} \sin(\beta_{y_n}^{(II_1)}(b_2 - y))\cos\frac{q\pi y}{2b_2}\,dy \tag{B.38}$$

all symmetries, region II_2

$$I_{C_{II_2}C_I} = \int_0^{b_1} \cos(\beta_{y_n}^{(II_2)} y) \cos\frac{q\pi y}{2b_2}\, dy \tag{B.39}$$

$$I_{S_{II_2}S_I} = \int_0^{b_1} \sin(\beta_{y_n}^{(II_2)} y) \sin\frac{q\pi y}{2b_2}\, dy \tag{B.40}$$

It was found that the algebraic solutions to the above integrals are large and best calculated using a symbolic solver package such as Maple$^{\text{TM}}$. The solution expressions can then be cut and pasted directly into a computer program.

Appendix C

Calculation of Unloaded Q Factor from the Measured Reflection Coefficient of a Resonator

In this appendix the method used for determining unloaded Q factor from the measured reflection coefficient S_{11} of the resonant structures of section 5.6 will be described. The method is the result of work carried out by Associate Professor Jim Ball at the Faculty of Engineering and Surveying, University of Southern Queensland (USQ), Queensland, Australia.

To obtain consistent unloaded high Q calculated results from lightly coupled S_{11} response data requires a numerical technique involving the least squares of the data points. This is because of the limitations of the vector network analyser (HP 8720C used in testing) which typically cause the measured data to be noisy and allow only a small number of points to be used in the narrow bandwidths required. Typical magnitude and phase data are shown in Figure C.1 for the WR159 waveguide shielded dielectric rod at the $N = 2$ half wave length, E_{11}^{y} mode, resonance described in Chapter 5. This example will be used through the rest of this section. The method procedure

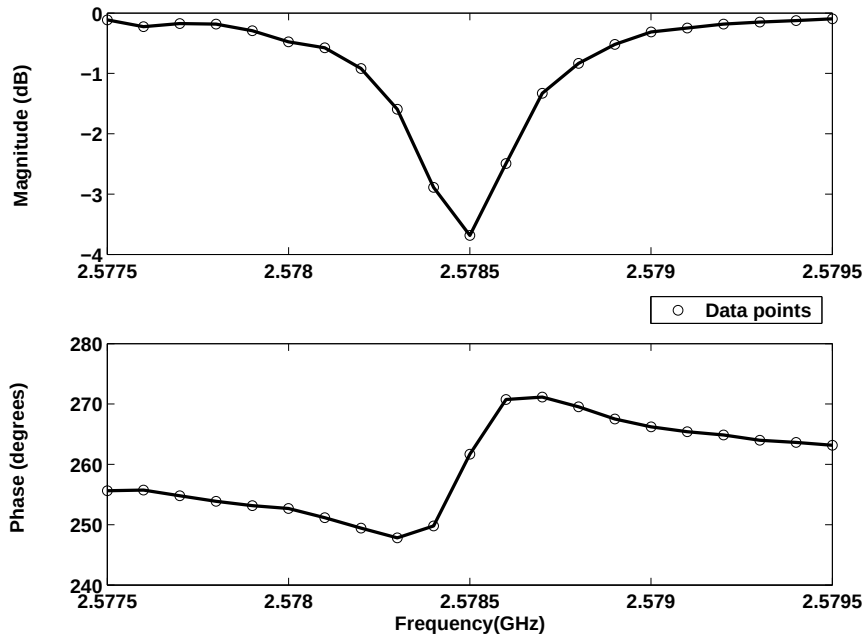

Figure C.1: Typical lightly coupled reflection coefficient response data ($N = 2$) from the WR159 shielded dielectric resonator of Chapter 5.

is as follows:

1. When plotted on a Smith chart the S_{11} data of an ideal resonator near resonance should form a perfect circle touching the outer circumference of the chart. A requirement of the method is that an accurate measure of the magnitude of the minimum reflection coefficient $|\rho_{min}|$ is required. This can be achieved firstly by calculating a least squares fitted circle to the data points (Kasa, 1976). The minimum reflection coefficient $|\rho_{min}|$ is than found as that value of reflection coefficient on the circle closest to the centre of the Smith Chart. A least squares fit circle of typical data is shown in Figure C.2 and in close up in Figure C.3.

2. In some cases it is desirable to reduce some of the off resonance part of the data ie above about 3db in the top magnitude graph of Figure (C.1). This part of the data can decrease accuracy due to the effects of noise and periodic ripples due to mismatches in the measurement setup (Leong & Mazierska, 2002).

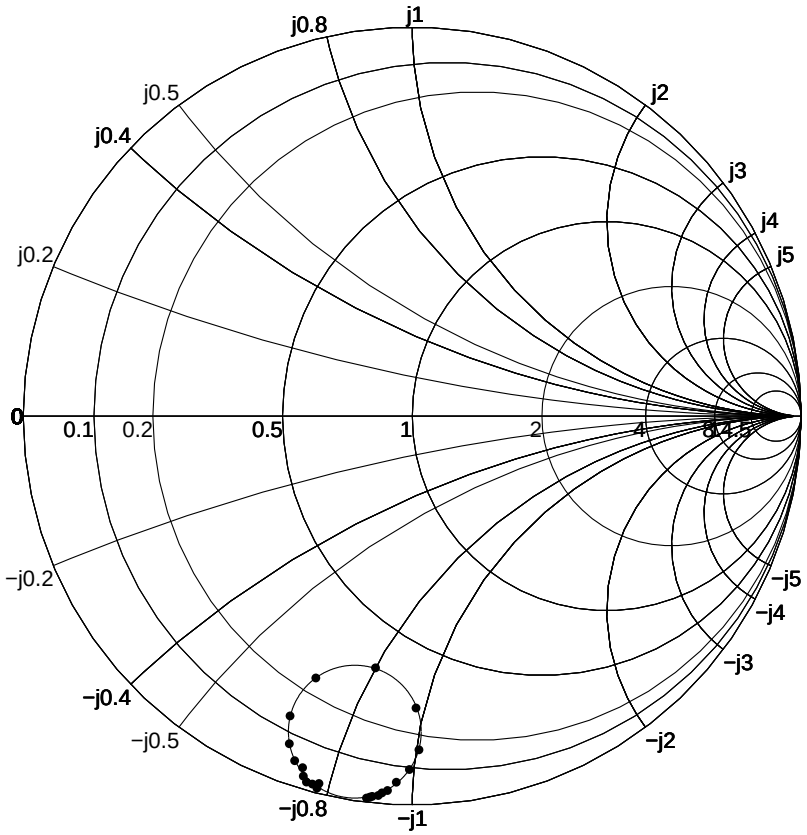

Figure C.2: A least squares fit circle to the $N = 2$, E^y11, mode reflection coefficient response data from the WR159 shielded dielectric resonator of Chapter 5.

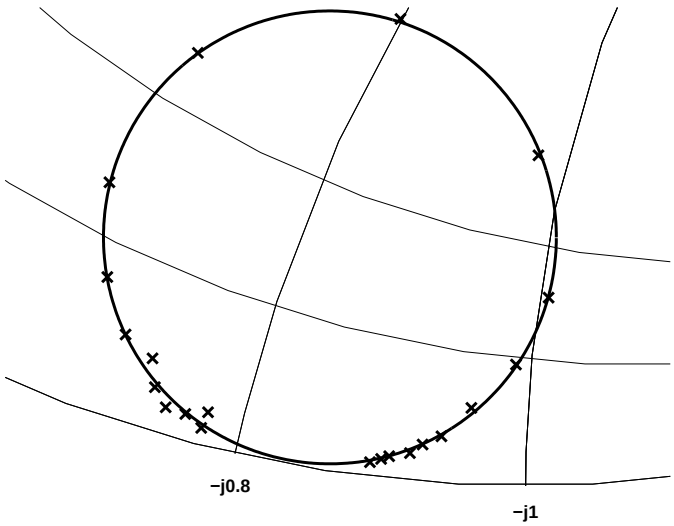

Figure C.3: Close up of a least squares fit circle to the $N = 2$, E^y_{11} mode, reflection coefficient response data from the WR159 shielded dielectric resonator of Chapter 5.

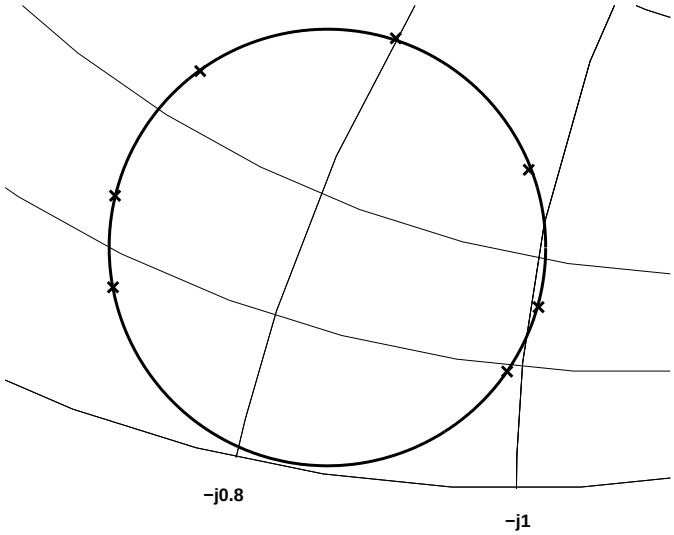

Figure C.4: Close up of a least squares fit circle to the $N = 2$, E_{11}^y mode, reflection coefficient response data from the WR159 shielded dielectric resonator of Chapter 5. Off resonance points removed

3. From Kwok & Liang (1999) the resonant structure can be modeled as a series resonant circuit with source impedance Z_o terminated by the series resistance R and the following expression can be written:

$$Q\left(\frac{\omega}{\omega_0} - \frac{\omega_0}{\omega}\right) = \pm\frac{2}{1 \pm |\rho_{min}|}\sqrt{\frac{|\rho|^2 - |\rho_{min}|^2}{1 - |\rho|^2}} = y \tag{C.1}$$

where at resonance

$$|\rho_{min}|^2 = \left(\frac{R - Z_0}{R + Z_0}\right)^2 \tag{C.2}$$

The first $\pm$ to the right of the equal sign in equation (C.1) is positive when $\omega > \omega_0$ and negative when $\omega < \omega_0$. The second $\pm$ is positive if the resonator is undercoupled and negative if overcoupled.

Equation (C.1) places the reflection coefficient data in a form that expresses it as a linear relationship between ω and y in the cartesian plane. Further simplifying the LHS of the equation gives:

$$Q\frac{(\omega + \omega_0)(\omega - \omega_0)}{\omega\omega_0} = y$$

and since $\omega \simeq \omega_0$ near resonance the equation finally becomes:

$$y = (\frac{2Q}{\omega_0})\omega - 2Q = (\frac{2Q}{f_0})f - 2Q \tag{C.3}$$

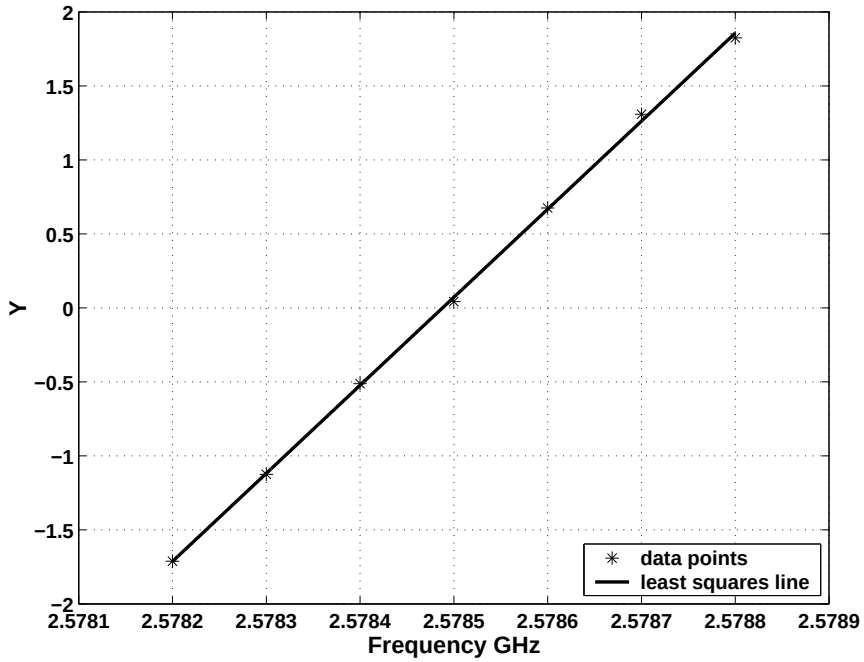

Figure C.5: Least squares fit line to the, N=2, E_{11}^{y} mode, reflection coefficient response data from the WR159 shielded dielectric resonator of Chapter 5. Off resonance points removed.

4. Equation (C.3) is in the form $y = a_1 x + a_0$

   This allows a_1 and a_0 to be determined from a least squared error straight line procedure obtainable from most mathematical texts. The WR159 shielded example, with reduced off resonance data points, is shown in Figure C.5. With reference to equation (C.3) the Q and the resonant frequency of a resonance can then be found from:

$$Q = -a_0/2 \tag{C.4}$$

$$\omega_0 = -a_1/a_1 \tag{C.5}$$

For more precise calculations of unloaded Q (Kajfez, 1994) (Leong & Mazierska, 2002), the effect of coupling loss is taken into account. With no coupling loss the response circle should touch the outer circumference of the smith chart. Any gap at this point shows the degree of coupling loss. In the measurements performed in Chapter 5 this gap

was always very small when using a lightly coupled probe (see Figures C.2 and C.3). The more precise methods complicate the computation of Q and were not considered necessary in the current work considering the magnitude in the uncertainty of estimated losses such as surface roughness (Morgan, 1949) and flange losses (Somlo, 1979).

One advantage of this method over the linear fractional method developed by Kajfez (1994) is that the resonant frequency is calculated explicitly at the first attempt.

Appendix D

Guide to Thesis Companion Disk

The following is a guide to the companion CD-ROM with this thesis. It contains a copy of the dissertation and a basic cross-section of the main computer programs for the coaxial resonator of Chapter 3, the rectangular shielded dielectric rod of Chapter 4 and for the rectangular shielded dielectric rod attenuation in Chapter 5. The programs are written using Matlab version 6.1 and may not be compatible with earlier versions.

To run a program it is recommended that the entire directory containing the files be copied to the users hard drive. This will ensure that all the necessary input files are available for the program, and that the program can save results to disk if required.

NOTE: When files are copied from CD-ROM to hard disk, each file is marked 'read-only' by default. It is strongly recommended that all files be changed to 'read-write' before attempting to run any of the programs from the companion CD-ROM.

The programs on the CD-ROM are edited versions of a small number of those used in the project and are meant as an explanatory guide to program descriptions in the relative chapters. For example only the programs for propagating and evanescent modes, using EO symmetry, are shown for the shielded rectangular dielectric rod waveguide. However the basic layout of the program is the same for all symmetries and could be modified

by changing the basis functions and wavenumber equations, as shown in Appendix B, for the symmetry required.

To aid in initial understanding of the use of the programs, example inputs marked in square brackets, are provided.

Chapter 3 Software

Coaxial Resonator

Program Name: CoaxResonator.m

Associated Functions: CoaxResCoeff.m, CoaxResFieldDisp.m, circleplotIP.m, lineMatlabCombIP.m, oxmodesIP.m

Location: \CoaxResonator\CoaxResonator.m

Platform: Matlab V6.1

Description: Finds the TEM resonant frequencies of a coaxial resonator, the unknown coefficients of the basis functions and plots some of the fields in the x-z and x-y planes.

Chapter 4 & 5 Software

Rectangular Shielded Dielectric Rod Waveguide

Program Name: EOBzIPVer.m

Associated Functions: By2QIP.m, EO_OOIntegralsIP.m, EOCoeffIP.m, EODieLossIP.m, EOEqIP.m, EOLossesIP.m, EOWallLossIP.m, oddsprogIP.m, WavNumXIP.m, EOBzCmplxIP.m, EOEqCmplxIP.m, xylinesRecDQSIP.m, YTEooeoEq.m, YTMooeoEq.m, RowInsert.m

Location: \RectShDielRodRes\EOBzIPVer.m

Platform: Matlab V6.1

Description: Finds the propagation coefficients of propagating, evanescent and complex modes, with EO symmetry, of the shielded rectangular dielectric rod waveguide. Also found for propagating modes are the unknown coefficients of the basis functions, the attenuation for a selected mode in the waveguide and plots of the vector fields in the x-y plane.